Co-ordination of cytoskeletal structure and dynamics with extracellular topography

Gorey, Alex

Awarding institution:
King's College London

Co-ordination of cytoskeletal structure and dynamics with extracellular topography.

Mark-Alexander GOREY

Randall Centre for Cell & Molecular Biophysics

School of Basic and Medical Biosciences

Faculty of Life Science and Medicine

PhD Supervisors: Dr Susan Cox, Professor Maddy Parsons

A thesis submitted for the degree of Doctor of Philosophy

to King's College London December 2022

Declaration

I, Mark-Alexander Gorey, confirm that the work presented in this thesis is my own. Where information has been derived from other sources, I confirm that this has been indicated in the thesis.

Acknowledgements

The work done in this PhD would not have been possible without the help of both my supervisors over the past 4 years. I would first like to thank my supervisor Susan Cox for allowing me to complete my PhD in her lab. Susan is not only the best supervisor someone could ask for but has allowed me to work to the best of my abilities while offering me her time, energy and support when needed. Going beyond the science, she truly went above with matters outside of research, to make sure I was doing well and staying as healthy as possible. For this and so many other things I am thankful to have had her as my supervisor and am proud to have been a member of her group. Thank you, Susan! You have been the best boss someone could ask for. To Maddy Parsons, I would like to thank her for her infectious motivation, passion, and advice over the years. Maddy brought so much to this thesis, and I have truly loved being even a small part of her team. This wouldn't have been possible without you so a massive thank you Maddy! It is truly rare to have such amazing supervisors and I will miss my time with both of you.

I had the best of luck getting to work with members from both their labs. I want to thank both Tom and Ishan, my fellow guys from the Cox group, who went through this with me, for all the laughs, advice and support they brought. You guys really made it the amazing experience it was. To Dylan, your work with the LLSM and everything outside, cannot be thanked enough! You were a dream come true hun and I'll forever be grateful. To Annelise, I'm going to miss running into you for a chat, gossip and laugh. I owe you both so much for all the laughs, help and time we spent together. To Richard and Lisa, thank you both for your wisdom and help with everything it made the world of difference in this project! From the Parsons group I really want to thank Willow, Grace, Claudia, Yonnis, Karin, Campbell, Brooke, Jake, Tom, Salwa, Irina, Alice, Mabel, Aneesa and Sofia for putting up with my constant interrupting of their serious work to go grab coffee. You have been a major part of this experience and I will miss you all so much. Sending my love to you all and I'll be back soon to pull you out of the lab again!

To my family I want to thank them for putting up with me and for supporting me over what seems like an endless journey. Mama and Dad, I love you both so much and I can't wait for us to celebrate together the end of this period in my life. It would never

have been possible without you both and everything you've done for me throughout my entire life. I love you so much. To Mariana, Ella and Michael thank you for keeping me in check all these years and can't wait to celebrate with you soon.

To my other family, I want to thank two queens that have been there for me through thick and thin, Ms Stefan and Ms Joe! You two have given me laughs, support and believed in me no matter the situation and I love you gurls like the crazy fools we all are. Margaritas are waiting at mine so hurry up!

To Anthony and Pete, I want to thank for having my back and always pushing me to keep going. Your support, love, and willingness to open a bottle of Rose no matter the time of day may be the only reason I made it through this in one sane piece. I'm anxiously waiting with a chill bottle for us to celebrate together!

To Aldo, I am so glad to have met you and am so excited for the future. You really believed in my abilities and have pushed me to where I am today. I'm so excited for this next chapter which would not have been possible without your support. Bacio!

Finally, to Jakob, I want to thank you for everything you have done for me which I cannot put into words adequately and for putting up with me during this time. I can't thank you enough for your endless positivity, support and humour that was my light during a very trying time. Sorry it took so long and can't wait to celebrate together now it is coming to an end!

Abstract

The local environment of cells is known to regulate their shape and motility. The vast majority of research to date has focused on analysis of motile behaviour of cells on two-dimensional surfaces. However, cells migrating within three-dimensional extracellular matrices (ECM) represent a more physiologically relevant environment, showing substantially different morphological and cell behaviour. Moreover, tissues in the human body are not uniform in stiffness or structure, presenting additional environmental variability for cells to navigate. *In vivo*, it is unlikely that cells experience fully two- or three-dimensional environments, but rather several structures of different dimensionalities that all influence the behaviour of the cell, and all interact with each other.

Here we investigate the role the local environment plays in regulating the structure and dynamics of single cells imbedded in three-dimensional collagen matrices of increasing stiffness. Increasing ECM stiffness is achieved through non-enzymatic glycation with D-ribose, across three concentrations at 0-, 50- and 200-mM. This represents a powerful technique for studying the short- and long-term dynamics and cell-ECM interactions imposed on one another in a consistent and reproducible way. Our investigations focus on the dynamics of single cells, the speed and location of actin treadmilling with respect to migration behaviour and matrix topography quantification in accordance with that of the ECM stiffness.

Using methods in atomic force microscopy, for ECM characterization, and live super resolution imaging enables us to analyse these three-dimensional structures without changing cell behaviour due to phototoxic effects, while still being able to capture dynamic cell events at high and low temporal resolution within relatively thick specimens in high resolution. Live super-resolution imaging revealed that initial seeding of single Hela cells to be affected directly in a stiffness dependant manner by the local environment. Studies showed matrices of lower stiffness having higher protrusion number and turnover in single cells, with smaller protrusion volume, causing a reduced invasion of the extracellular environment. Conversely in matrices of increasing stiffnesses single cells demonstrated greater protrusion development and life span, with higher numbers of stress fibres and greater reach on its surrounding environment. High temporal resolution imaging data, acquired at 24-

hours, enabled the analyse in greater depth of the correlation between protrusion, actin and collagen dynamics respectively to local environments of increasing stiffnesses.

These studies demonstrate a novel and reproducible approach, paving the way for future studies to understanding mechano-regulated mechanisms of single cells in three-dimensional environments at a molecular scale. Shedding light on how the ECM organisation and stiffness plays a role in changing local cytoskeletal dynamics and the effects of cytoskeletal components on effectively navigating its local environment, provides new insight into cell behaviour in healthy and diseased tissue environments.

Table of Contents

Table of Figures

List of Tables

Abbreviations

Abbreviation	Meaning
2D	Two-Dimensional
3D	Three-Dimensional
AFM	Atomic Force Microscopy
AFT	Alignment by Fourier Transform
AGE	Advanced Glycation End Products
Arp2/3	Actin Related Protein 2/3
BM	Basement Membrane
CAF	Cancer Associated Fibroblast
CB	Cell Body
CLSM	Confocal Laser Scanning Microscopy
CNA35-EGFP	Collagen Binding Protein labelled with fluorescent EGFP
CSC	Cancer Stem Cell
CTC	Circulating Tumour Cell
ECM	Extracellular Matrix
EGFP	Enhanced Green Fluorescent Protein
F-Actin	Filamentous Actin
FAK	Focal Adhesion Kinase
FBS	Fetal Bovine Serum
Fiji	ImageJ
G-Actin	Globular Actin
GAG	Glycosaminoglycans

HA	Hyaluronic Acids
HEK	Human Embryonic Kidney Cells
IM	Interstitial Matrix
iSIM	Instant Structured Illumination Microscope
kDa	Kilo Dalton
L	Litre
LLSM	Lattice Light Sheet Microscope
LOX	Lysyl Oxidase
M	Molar
mg	Milligrams
min	Minutes
MIP	Maximum Intensity Projection
mL	Milliliter
mm	Millimeter
mM	Milimolar
MMP	Matrix Metallo-Proteinases
NA	Numerical Aperture
nm	Nanometer
Pa	Pascals
Prot	Protrusion
Rho GTPase	Ras Homology Guanosine Triphosphatase
Rhoa	Ras Homology Family Member A
ROCK	Rho-Associated Protein Kinase

ROI	Region of Interest
ROS	Reactive Oxygen Species
RPM	Revolution per Minute
SHG	Second-Harmonic Generation
SRC	Proto-oncogene tyrosine-protein kinase Src
TMI	Tumour Microenvironment
VASP	Vasodilator-stimulated phosphoprotein
µg	Micrograms
µL	Microliter
µM	Micromolar
µm	Micrometer

1 Introduction

1.1 Components and function of extracellular matrix

The extracellular matrix (ECM) consists of the non-cellular components secreted by cells that provide the structural, biomechanical, and biochemical cues to all multicellular organisms. Through varying, unique, and tightly controlled composition, the ECM in tissues offers different levels of rigidity, the ability of a solid to change its shape, and elasticity, the ability of a deformed material body to return to its original shape and size, best designed for their specific function and optimal productivity. The ECM is highly dynamic during tissue homeostasis, with constant cycles of deposition, degradation, and remodelling by resident cells. The ECM offers versatility in the properties of the local tissue, such as elastic, tensile, and compressive strength (S. H. Kim, Turnbull, and Guimond 2011). This enables the flexibility to provide tissue-specific support and a dynamic interplay between cells and the surrounding ECM to control tissue function (Kai, Laklai, and Weaver 2016). Deregulation of ECM dynamics, mechanics and composition can lead to a number of different pathologies including cancer (Bonnans, Chou, and Werb 2014).

Varieties of ECM structures have a diversity of roles from forming the basement membrane (BM) to the interstitial matrix (IM) that are intimately interconnected. The BM, also known as basal lamina, delineates borders between distinct cell types having different functions, controlling cell organization and being heavily implicated in the differentiation and development of healthy tissue. Located under the BM, the IM forms the porous 3D lattice between cells of a common type with a common function regulating cell adhesion, development, differentiation, growth, and survival. These various components are produced by different types of cells, the BM by epithelial cells and IM by fibroblasts (Pompili et al. 2021). Fibroblasts are a heterogenous cell type well-known for their central role in the production, homeostasis, and regeneration of the ECM. Fibroblasts secrete all components of the ECM dynamically responding to a broad array of paracrine (from nearby cells) and autocrine (self- secreting) signals, such as cytokines and growth factors (Kendall and Feghali-Bostwick 2014; J. M. Zhang and An 2007)

The components of the ECM are divided into two broad classes, based on their macromolecular types: fibrous proteins and proteoglycans. The fibrous molecular composition is mainly comprised of collagens, elastin, and fibronectin with collagens being the most abundant proteins, making up 30% of the total protein mass in multicellular animals and the main structural component of the ECM (Frantz, Stewart, and Weaver 2010). A graphical representation of the ECM is provided below in **Figure 1.1.**

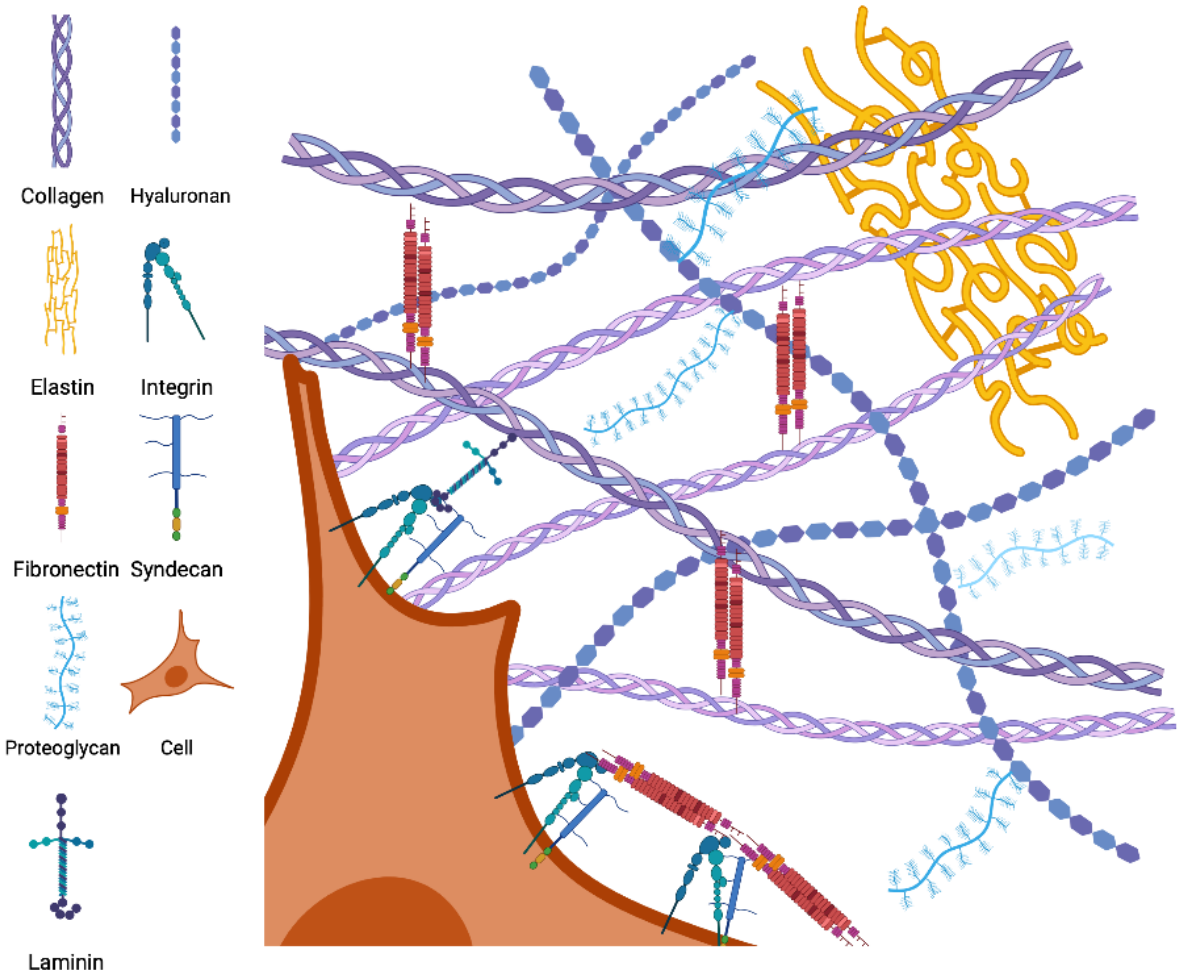

Figure 1.1 - Composition and organization of the ECM
Simple schematic representing the composition of the ECM and cell interface. Fibrillar structures such as collagen, elastin and fibronectin coupled with proteoglycans and hyaluronan are the major components in regulating the chemical and structural properties of the ECM. Laminin shown is mainly found in the BM. These properties are sensed and interpreted by the cell through transmembrane binding sites, some being integrin and syndecan, known as mechanotransduction affecting intracellular components. Created with BioRender.com.

Being the main structural element of the ECM, collagen composition provides tensile strength and supports for cell adhesion and migration (Rozario and DeSimone 2010). The different degrees of fibrillar rigidity and structure in the ECM is provided by the controlled relative expression of varying collagen subtypes secreted by fibroblasts in the ECM. A graphical representation of the structural features of collagen ranging from procollagen, tropocollagen molecules, collagen fibrils to collagen fibres is provided below in **Figure 1.2**. 28 different types of collagens have been described to date, all of them sharing the structure of polypeptide triple-stranded α chains (Ricard-Blum and Ruggiero 2005). Intracellular modifications of the collagen polypeptide chain, via hydroxylation of proline and lysine and the addition of sugars, form the triple-helical right-handed coiled procollagen molecule. Collagen glycation causes inter-molecular crosslinking between the triple-helical regions of the adjacent collagen molecules. Further variations seen in collagen subtypes arise from the different compositions of homotrimers and heterotrimers self-arranging into microfibrils (Brodsky and Persikov 2005). Once mobilised to the extracellular space, terminal domains are removed forming tropocollagen crosslinked fibrils that self-assemble through deamination of residues into stable collagen fibres. The globular terminal domains at each end are vital in the proper assembly of collagen monomers and consequently larger collagen aggregates, with mutations in collagen genes resulting in the abnormal assembly of fibrils and fibres (Culbert et al. 1995).

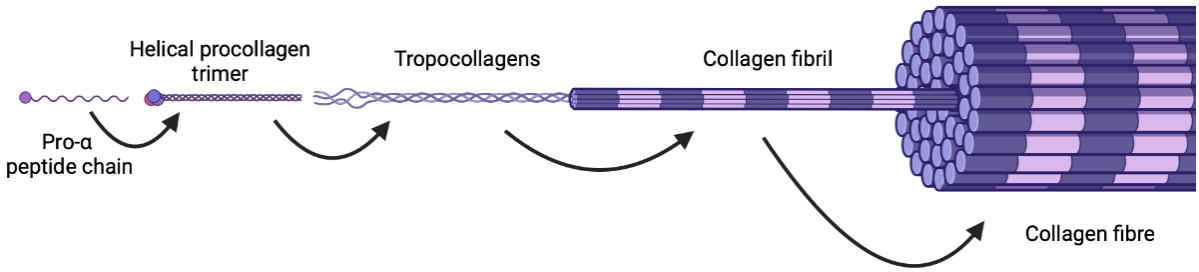

Figure 1.2 – Structural features of collagen assembly
Simple schematic representing the biogenesis of fibrillar collagen. α-chain subunits are synthesized intracellularly and assemble into helical collagen trimers before being secreted into the extracellular space resulting in the formation of mature tropocollagen. LOX catalyse tropocollagen chains crosslinking them to form collagen fibrils and further organized and assembled into collagen fibres. Created with BioRender.com.

The different subtypes of collagens offer different structural advantages to tissue, such as collagen IV being the major network constituent of BM, collagen VII anchoring the BM and collagen II making up 50% of all cartilage protein (Rosso et al. 2004). Most IM collagen subtypes highly associate with type I collagen. Collagen type I is a heterotrimer encoded by two genes, Col1a1 and Col1a2, and is the most abundant of the collagens in mammals, undergoing dynamic remodelling, critical in normal development and present in a large range of tissues such as skin, bone, and tendons (Naomi, Ridzuan, and Bahari 2021). ECM stiffness can be altered by varying the density of macromolecules, such as collagens, or through increasing crosslinks via lysyl oxidase (LOX) enzymatic function (Lucero and Kagan 2006) or non-enzymatic glycation (Mason and Reinhart-King 2013), and by degradation of the ECM by matrix metallo-proteinases (MMPs, Deryugina and Quigley 2006). Collagen type I is widely used *in vitro* cell culturing as a 3D biomaterial, providing a more physiological scaffold for the study of the cell-ECM relationship. Collagen fibres are critical for cell-ECM interaction, providing physical support and chemical properties required for integrin-mediated cell signalling (Lu et al. 2011).

Fibronectin is a multi-domain fibrous glycoprotein intimately involved in the organization of the interstitial ECM and in mediating cell attachment and function.

Available in two forms, fibronectin can be found as soluble plasma fibronectin, a major component of blood synthesized by hepatocytes, or insoluble fibrillar fibronectin, assembled in the ECM after fibroblast synthesis (Pankov and Yamada 2002). Fibronectin is encoded through a single gene and secreted as a dimer, composed of nearly identical covalently linked sub-units, into the ECM containing binding sites for other fibronectin dimers, collagen, and transmembrane cell receptors (Pankov and Yamada 2002). Splicing of mRNA precursors of fibronectin enables the production of over 20 variants with different cell-adhesive, ligand-binding, and solubility properties. This provides a mechanism for precisely altering ECM composition, functional flexibility, and integrin cell-ECM contact (Parisi et al. 2020).

Being highly mechano-sensitive, the full-length of fibronectin can be subject to stretching through traction forces imposed by the cells or other ECM proteins, further exposing cell or ECM binding sites that affect cell behaviour (Smith et al. 2007). Cell-surface binding is essential in the assembly of fibronectin dimers into fibrils and is implicated in collagen type I assembly and vice versa.

In addition to collagen and fibronectin, other components such as elastin play a critical role in the structural, biochemical, and biomechanical properties of the ECM. Elastin provides the elastic recoil to tissue after repeated stretching, and its precursor, tropoelastin monomers, assembles into fibres and crosslink heavily with one another through their lysine residues via the LOX enzymes (Reichheld et al. 2019). Elastin associates with collagen in a tightly regulated manner, limiting the extremity to which it can stretch, and providing integrity to tissues undergoing repetitive deformation (Swee, Parks, and Pierce 1995).

Laminins are trimeric glycoproteins composed of α, β, and γ chains that induce signalling pathways affecting cytoskeletal organization via integrin binding (Berrier and Yamada 2007; Domogatskaya, Rodin, and Tryggvason 2012). Mainly found in the BM, laminins have great structural diversity, up to 16 isoforms offering both common and specific functions. Common important functions include interacting with

receptors anchored in the BM to adjacent cells regulating signalling pathways and cellular functions. BM can contain one to several members of the laminin family, heavily impacting the unique physiological functions of different BM in the body (Aumailley 2013). Inducing specific functionalities, such as adhesion, migration, and differentiation, laminins are vitally important in phenotypic maintenance and found to play a role in the invasiveness of cancer cells (Schéele et al. 2007).

Proteoglycans are part of the second class of macromolecular types found in the ECM, and provide a variety of functions such as buffering, hydration, binding, and force-resistance. Proteoglycans are membrane- and ECM-bound proteins secreted by cells that act as ‘space fillers’ in all ECM, providing lubricating and hydration functions (Järveläinen et al. 2009). Proteoglycans allow the covalent bonding of glycosaminoglycans, long chains of negatively charged disaccharides, to trap hormones, cytokines, growth factors, cations, and water within tissues (Nikitovic et al. 2018). Proteoglycans are classified into two groups, short leucine-rich proteoglycans, using collagen-binding proteins to induce the structure and formation of the ECM, and hyalectans, serving as molecular bridges between the cell surface and ECM (Iozzo and Karamanos 2010; Iozzo and Schaefer 2015).

Hyaluronic acids interact with proteoglycans to help fill large volumes of tissue. Hyaluronic acids are linear negatively charged polysaccharides, ubiquitously present in the ECM and allow further fine-tuning of the biophysical properties of tissues through control of compressive and lubricating aspects of the matrix (Abatangelo et al. 2020; Camenisch et al. 2000).

Thus, the composition and dynamic biophysical properties of the ECM influence biochemical signals and cell phenotypes, and dysregulation of these can play a key role in cancer progression (Egeblad, Rasch, and Weaver 2010).

1.2 Cell-ECM interactions and mechanotransduction

The ability of cells to rapidly sense and react to new or changing structures in the surrounding ECM is vital for adaptation, migration, and survival. The process through which cells actively sense, integrate and converts mechanical stimuli into intracellular signals is known as mechanotransduction (Dobner, Amadi, and Lee 2012). In order to detect ECM rigidity and topography, cells mechanically probe their microenvironment via cytoskeletal structures, such as filopodia and lamellipodia to sense the mechanical feedback and resistance of their environment through varying degrees of adhesion. Integrin-based focal adhesions provide the main cell-ECM contact site and control intracellular signalling cascades leading to cytoskeletal organisation and traction (Dupont 2016).

Interactions between the cell cytoskeletal structures and the ECM are mediated by transmembrane proteins known as integrins. Integrins are bidirectional signalling receptors which function as non-covalent heterodimers composed of 18 α and 8 β subunits, able to generate 24 different integrins that give them the versatility required for binding to varieties of ECM ligands, such as fibronectin, collagen, and laminins (Mana, Valdembri, and Serini 2020). Trafficking of integrins regulates their cell-surface availability thorugh endocytosis and recycling to the plasma membrane via both clathrin dependent and independent routes (Ezratty et al. 2009). This enables the mediation of integrin availability, localisation and plays a role in adhesion and cell migration (Paul, Jacquemet, and Caswell 2015).

The inactive forms of integrins (closed) show low affinity for ECM ligands. Integrins do not have intrinsic enzymatic activity but rely on interactions with cytoplasmic proteins to promote downstream signalling (Harburger and Calderwood 2009; S. H. Lo 2006). Intracellular signals causing conformational changes to integrin extracellular domains, termed inside-out signalling, enable the opening and activation of integrins (Calderwood 2004). Cytosolic integrin adaptor proteins, such as talin, bind to β-subunits tails to separate integrin subunits opening their conformation, and to actin along with other cytoskeletal and signalling pathways, regulating their activity (Critchley and Gingras 2008). This open conformation of

integrins provides a high affinity to ECM ligands and in recruiting more effectors. Kindlin, cooperating with and functioning similarly to talin, promotes integrin clustering, protrusion extension and focal adhesion maturation (Kechagia, Ivaska, and Roca-Cusachs 2019). A graphical representation of integrin mechanosignalling is provided below in **Figure 1.3**.

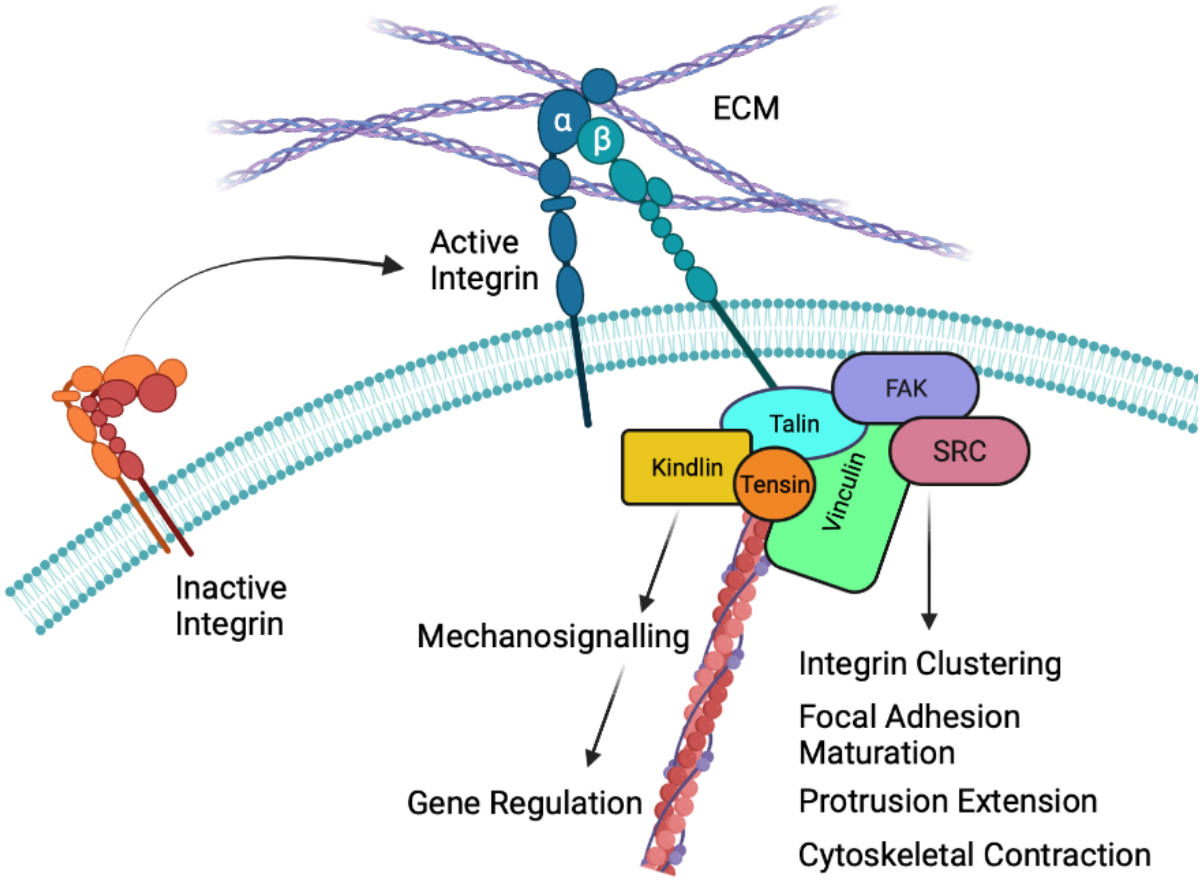

Figure 1.3 - Summary of cell- ECM integrin mechanosignaling
Simple schematic representing cell-ECM integrin signalling. Inactive integrin lacking ECM ligand in closed conformation shown on the left with lack of downstream signal transmission. Active integrin shown binding ECM ligand with bound Talin (Blue) to β subunit (Teal). Kindlin (Yellow), Vinculin (Green) and Tensin (Orange) allow mechanosignal transmission through actin cytoskeleton to affect gene regulation within the nucleus. FAK (Purple) is also bound to Talin, which acts as a binding site for Src kinase (Mauve) from which downstream mechanosignalling affects various intracellular components. FAK also drives integrin clustering, focal adhesion maturation and cellular contractility. Created with BioRender.com.

Extracellular signal ligand affinity can also induce integrin activation, transmitting signals from the ECM into the cell, termed outside-in signalling (Hynes 2002; Miranti and Brugge 2002). Promoted by binding of the ECM and force generation, this slows the diffusion of integrin dimers, triggering several of the steps involved in integrin activation, essentially by pulling integrins open. Pulling tensile forces on bound integrins leads to feedback mechanisms further affecting integrin conformation and ligand-binding-kinetics. The deformation itself of the cell membrane around bound integrins gives rise to higher probability of binding to ligands. Reciprocally, actin can pull on integrins, further contributing to force generation (Paszek et al. 2009).

Integrin activation is key in inducing and regulating tissue development, formation, angiogenesis, matrix remodelling and cell migration and proliferation (Calderwood 2004). Integrins are the key receptor family in focal adhesions. Proteins, such as FAK and vinculin, mediate the initial connection of growing adhesomes to integrins and F-actin. As it increases in size, more proteins are recruited, such as zyxin and myosin II, influencing the contractility and tension transduction of focal adhesions to the cell, allowing integrin adhesion mechano-transduction (Gardel et al. 2010; Geiger, Spatz, and Bershadsky 2009; Small et al. 1998). As nascent adhesions mature into focal adhesions, the upregulation of integrin clustering and stress fibres induces cell spreading and cytoskeletal contraction (Geiger, Spatz, and Bershadsky 2009; Martino et al. 2018).

Integrin clusters bound to ECM ligands, crosslink with each other and with actin when experiencing mechanical resistance. Integrin clustering induces an accumulation of adaptor proteins, modulating the enzymatic activity of kinases, phosphatases and small GTPases helping transmit mechanical information of the surrounding ECM (Bachmann et al. 2019; Raab-Westphal, Marshall, and Goodman 2017). These clustering complexes contribute to the additional recruitment of cytoskeletal signalling proteins, such as Paxillin, Vinculin, ARP2/3, and F-actin, and triggers the activation of the FAK, SRC, AKT and ERK pathways in gene regulation

(Elfenbein and Simons 2013; Liu, Calderwood, and Ginsberg 2000; Paul, Jacquemet, and Caswell 2015)

Focal adhesions are an integrin-mediated cell–ECM adhesion structure that anchors the ends of actin filaments (stress fibres) and mediates strong attachments to substrates. It also functions as an integrin-signalling platform. Focal adhesions are key components in the cell-ECM in sensing the mechanical components, mediating actin-myosin contractility in response to ECM adhesion. With hundreds of different proteins, focal adhesions offer diversity of function from anchoring cells to being dynamically assembled and disassembled providing traction and mobility to migrating cells (Geiger, Spatz, and Bershadsky 2009).

FAK is recruited to integrin-ligand complexes, known as nascent adhesions, facilitating further recruitment of focal adhesion maturation components. With maturation, focal adhesions increase in size through increased integrin clustering to the termini of stress fibres. This upregulation induces increased recruitment of other proteins, such as vinculin, paxillin and zyxin causing conformational changes to the cytoskeleton through contraction and spreading via Rho GTPases (Warner, Wilson, and Caswell 2019). This causes a positive feedback loop further activating FAK and upregulation of focal adhesions, therefore making it a vital factor in mediating dynamic turnover of focal adhesions and cytoskeletal organisation of its dynamics (Mierke et al. 2017).

The cytoskeleton is composed of an interconnected network of filaments and regulatory proteins designed to rapidly support, connect, and alter cellular functions to best survive and manipulate the ECM (Fletcher and Mullins 2010). This network, comprised of filamentous actin, microtubules, and intermediary filaments, is all vital in the mechanotransduction sensing, architectural organisation of the cell and imposition of contractile forces of the cell (Rizzelli et al. 2020).

F-actin filaments are polar filamentous single-stranded helices composed of actin monomers, also known as globular actin (G-actin), that polymerise in an ATP-dependant fashion (Etienne-Manneville 2004). The polar assembly and disassembly of F-actin, through the polymerisation and depolymerisation of G-actin, enables a controlled cellular process known as actin treadmilling. Actin polymerisation and depolymerisation occurs through actin-binding proteins such as profilin and cofilin respectively, enabling highly controlled and rapid turnover of F-actin structures (Kardos et al. 2009). Through F-actin regulators, under the influence of Rho GTPases, cytoskeletal structures impose deformations on the cell membrane through F-actin polymerisation to facilitate the migration or invasion of cells. Rho GTPases belong to the Ras superfamily and modulate the actin cytoskeleton, migration and more, with important Rho GTPases including RhoA, Rac1 and Cdc42. Generally speaking, the function of Rho GTPases is mediated by binding of GTP to Rho GTPases. GTP-bound Rho GTPases subsequently bind to targets and activate them by inducing conformational change or altering localisation (Svensmark and Brakebusch 2019).

F-actin assembles into more complex bundled arrays in the format of stress fibres (anti-parallel F-actin fibres) or filopodia (parallel F-actin bundles), providing structural support for adhesion and migration (Doyle and Yamada 2016). Proteins such as Arp2/3 enable actin nucleation resulting in assembly of branched actin networks at 70°, supporting membrane protrusion through assembly of larger-scale actin meshwork at the leading edge. ENA/VASP proteins support formin-mediated elongation promoting the unbranched upregulation of F-actin at filament heads by inhibiting capping proteins and binding to profilin units that are themselves bound to G-actin (Breitsprecher et al. 2011). Central, dorsal, and transverse actin stress fibres anchor to focal adhesions at either both ends, one end or none respectively (Small et al. 1998b; Tojkander, Gateva, and Lappalainen 2012).

A simplified graphical representation of actin-based protrusion and integrin signalling in filopodia, lamellipodia and integrin clustering tractional force is shown in **Figure 1.4**. Filopodia, defined as parallel F-actin bundles assembled in thin protrusions

extending from the plasma membrane, enable cells to explore and directionally invade their surroundings (Jacquemet, Hamidi, and Ivaska 2015; Kerber and Cheney 2011). Thin sheet-like protrusions from the leading edge of the cell, known as lamellipodia, contain a mesh of F-actin networks under the control of formins and ARP2/3 (Svensmark and Brakebusch 2019). Contractile forces are generated by the interactions of F-actin structures and non-muscle myosin II. This process, known as actomyosin contractility, controls cell shape, migration, and acts as a mechanosensory component of the ECM.

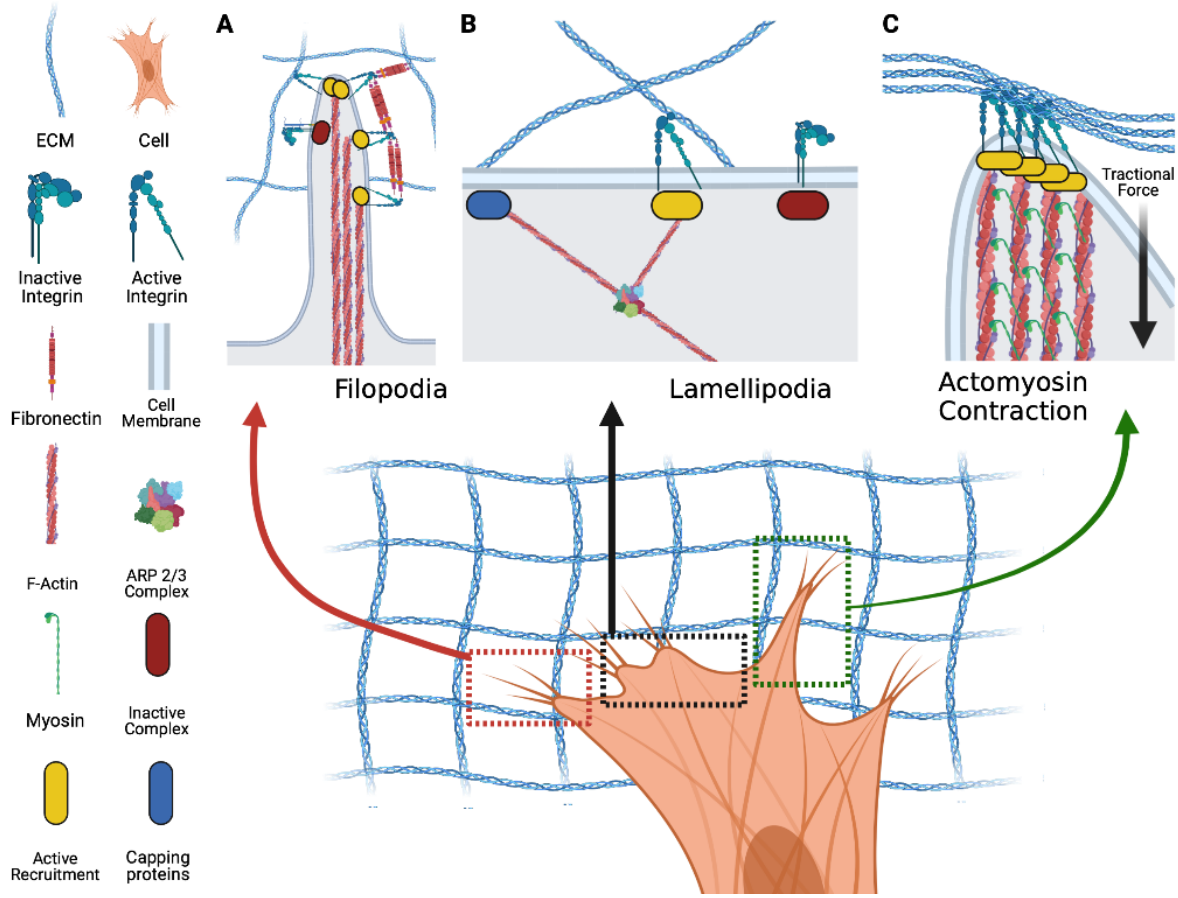

Figure 1.4 – Actin protrusions of the cytoskeleton when exploring and applying tractional force on the ECM
Simple schematic of actin-based protrusions used in 3D single cell ECM mechanotransduction. Filopodia (**A**) show inactive integrins lacking ECM ligands and downstream signalling transmission. Active integrins coupled with the ECM induce active recruitment proteins linked to fine F-actin bundles able to transmit signals downstream inducing conformational changes to the cytoskeleton. ARP2/3 mediated branched filamentous actin networks form lamellipodia (**B**) connecting to the active integrin complex. Actomyosin contractions (**C**) induce tractional forces on the surrounding ECM through active integrin clusters. Created with BioRender.com.

During this process, the role of RhoA, RhoC and downstream target Rho- associated kinases (ROCK1/2) are essential with RhoA activating ROCK which subsequently phosphorylates the regulatory light chain of myosin II, disrupting the influence of the phosphatase MYPT1. Phosphorylated myosin II promotes actin filament contraction and subsequent force generation, with actomyosin organised into a contractile network of stress fibres and peripheral bundles (Pandya, Orgaz, and Sanz-Moreno 2017). FAK and FAK-SRC signalling complexes in focal adhesions, and its active kinase domain, have been shown to regulate focal adhesion. The ability to transmit and generate contractile forces through ROCK kinase and MLCK is necessary to facilitate FAK-dependent cell invasion. These findings indicate that the focal adhesion protein FAK plays a central role as a mechano-coupling and mechano-regulating protein. This shows an intricate link between focal adhesions and their role in actomyosin contractility promoting 3D motility (Mierke et al. 2017).

Ultimately internal actin networks are used as mechanosensors of ECM stiffness due to their response to external stiffnesses and induction of contractile force generation through stress fibres, due to mechanoreciprocity (Colombelli et al. 2009). The reciprocity between cells and the ECM are controlled through these contractile forces resulting in bi-directional alterations to cell shape and ECM remodelling. These are essential processes in the homeostasis, mechanotransduction, migration and invasion of collective and single-cell migration (Röper 2013; Shellard and Mayor 2019)

1.3 ECM remodelling and biomechanics in cancer

In general, cancer refers to diseases characterized by the abnormal growth and uncontrolled division of cells as a result of cellular mutations, without causing cell death. This uncontrolled proliferation and abnormal behaviour of mutated cells can cause significant architectural shifts to the ECM through remodelling, triggering accelerated deregulations to the relationship between the cell and surrounding microenvironment, resulting in a more severe malignancy and metastatic progression (Cox and Erler 2011). There are several factors that can cause cancer cell mutations, including but not limited to ageing, genetic predispositions, and lifestyle choices. Throughout the body, tumour cells compete actively and advantageously with healthy cells for resources. Over time, the mechanisms for ensuring proper cell division and repairing of mutations diminish as we age. As a result of exposure to exogenous and endogenous stresses, it is also more likely for mutations to occur, reducing DNA damage response, and, in some cases, genetic mutations through inheritance can serve as a clear indicator for the development of cancer (Sulli, di Micco, and di Fagagna 2012).

The term tumour suppressor gene refers to proteins that play a vital role in DNA cell cycle checkpoints. The rapid progression of cancer can be attributed to these driver mutations, such as P53, which promotes cell cycle arrest for DNA repair or pro-apoptotic functions in damaged cells. The proliferation of cancer cells can lead to an increase in number of mutations, resulting in increased competitive expansion and competition for nutrients in the environment (Ozaki and Nakagawara 2011). Consequently, this expansion results in hyperplasia, tissue enlargement, dysplasia, abnormal cell growth, and neoplasia. Neoplasia is an abnormal growth of cells, but it is normally localized in one location and is clinically classified as stage 1 or stage 2. This classification facilitates the understanding of tumour growth and spread, with stage 0 indicating an in-situ tumour that has not spread, stages 1 and 2 indicating subsequent growth without spreading, stage 3 indicating local spread to surrounding tissue and stage 4 normally indicating metastatic spread to distant secondary sites. Under a microscope, tumour grades represent the appearance and behaviour of biopsied cancer cells. They range from grade 1 resembling normal cells to grade 3 exhibiting abnormal characteristics such as growth and dissemination. The

metastasis of cancer is a multi-step process that involves cancer cells escaping from the primary site, surviving in the circulation, and colonizing distant or nearby organs. (Hoshino et al. 2015).

A bidirectional and highly dynamic interaction between cancer cells and the tumour microenvironment (TMI) encapsulates all the exchanges between cell-cell and cell-ECM. The TMI consists of tumour cells, mesenchymal stromal cells, stromal fibroblasts, endothelial cells, immune cells such as macrophages and lymphocytes and the non-cellular components of the ECM such as collagen, fibronectin, hyaluronan among others (Paszek et al. 2005; Provenzano et al. 2006). Primary tumours can elicit changes to surrounding cells, exploiting Cancer Associated Fibroblasts (CAF) or tumour associate macrophages to elicit pro-inflammatory and proangiogenic responses. CAF play key roles in the TME through the mediation of tumour growth, ECM remodelling, drug resistance and metastasis. Through mediation of numerous signalling pathways, the heterogenous origin of CAF offers a broad range of characteristics and innate ability to utilise the surrounding ECM to support their growth. This environment supported by CAF also supports the viability of cancer stem cells (CSC). CSC can produce different cell phenotypes such as fibroblasts and endothelial cells, which further support growth and recurrence of the tumour through the production and secretion of growth factors and ECM components (Kulsum et al. 2019; Nair et al. 2017).

Changes in composition and architecture of ECM also leads to changes in stiffness and viscoelastic properties and these factors are increasingly recognised to play roles in tumour progression and patient prognosis. Increased collagen crosslinking and remodelling have been shown to increase tumour metastasis through integrin-dependent signalling pathways (K. R. Levental et al. 2009; Özdemir et al. 2014). Leading edges of some solid tumours exhibit aligned collagen fibres providing highways for collective and single-cell migration of cells away from the tumour core. Leading invasive cells can also remodelled the ECM to create paths for following cells to more easily migrate and disseminate (Conklin et al. 2011). Deregulation of the ECM can also trigger increased remodelling of the ECM by surrounding ‘normal’

cells, thus further perpetuating the metastatic cascade (Fang et al. 2014; Provenzano et al. 2008). The initial penetration and migration of cancer cells requires mechanical forces and stress imposed by the cell to rupture into the surrounding matrix (Hiramatsu et al. 2013; Kelley et al. 2014). Cell adhesion structures known as invadopodia are rich in F-actin-rich but differ from focal adhesions in acting as focal points to secrete high levels of ECM degrading enzymes. Invadopodia are thought to be required for initial breach of the BM surrounding a solid tumour, to permit initial invasion to occur. A simplified graphical representation of tumour invading and remodelling the surrounding and neighbouring ECM through invadopodium and increased release of MMP is shown in **Figure 1.5** (Hagedorn et al. 2013).

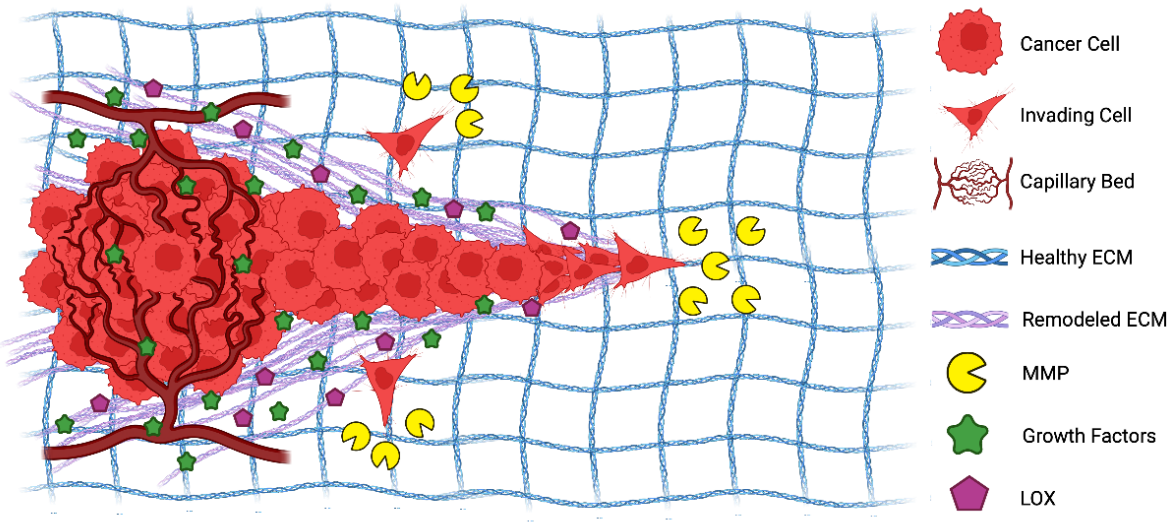

Figure 1.5 – ECM remodelling and disruption in tumour progression and metastasis
Simple schematic of tumour invading and remodelling the surrounding healthy tissue through single and collective cell invasion. Increased release of MMP at the leading edge and in single cells cause increased ECM degradation, exposing more binding sites coupled with a higher release of growth factors. Growth Factors accelerate the promotion of angiogenesis and proliferation causing increased fluid stress, solid stress, and hypoxia. ECM degradation also causes increases LOX release, further contributing to the stiffening of the surrounding tissue and creating a microenvironment even more conductive to tumour development and cancer cell invasion. Created with BioRender.com.

MMP are required for the breach and subsequent softening of the tissue at the leading invasion front enabling migration (Deryugina and Quigley 2006). Increased MMP activation also leads to increased release of factors such as growth hormones that are sequestered in the ECM and this can promote feedback loops to influence both cancer cell behaviour and tumour angiogenesis further amplifying tumour growth. MMP-dependent ECM degradation also exposes cryptic binding sites further driving cell-ECM interaction creating a localised microenvironment around tumours that is more conducive to invasion (Kessenbrock, Wang, and Werb 2015).

Fluid stress within the TMI is generated by blood and lymphatic flow through vessels, vasculature, and interstitial fluids (Sarntinoranont, Rooney, and Ferrari 2003). Solid stress is the impact seen by non-fluid components of the tumour due to the physical increase of pressure from ECM and uncontrolled proliferation of cells within the limited space. The uncontrolled growth of cells proliferating into each other and the consequent pressure on the TMI and surrounding tissue can constrict the vessels feeding the tumour and increase hypoxia (Chauhan et al. 2014; Cheng et al. 2009). Hypoxia-induced factors within the TMI also regulate MMP activation, enhance collagen production and increase LOX release leading to stiffening of the ECM (Gilkes, Semenza, and Wirtz 2014).

Although an area of recent research focus, the mechanisms by which increased mechanical stress in tumours contributes to malignant behaviour remains unclear but is rapidly expanding with the new developments in 3D methods in *in vitro* cell-ECM culturing. Vast mechanoregulatory circuits show links to physical cues from the ECM, through integrin adhesion, to intracellular pathways controlling cell function and phenotype. Cytoskeletal tension, mediated by matrix stiffness, can drive cell and focal adhesion activity in perturbing the tissue organization promoting malignant transformation of tumours (Paszek et al. 2005). Understanding the link between increased solid stress and increased metastasis or drug resistance are critical to determining targetable mechanisms for those patients exhibiting high stiffness tumours. Recent developments in more physiologically relevant *in vitro* models to assess these mechano-induced signals will provide means to develop a more

detailed understanding of the relationship between ECM-generated stress and cancer cell function.

1.4 *In vitro* methods exploring the cell-ECM relationship in 3D

The mechanical, chemical, and biological properties of tumour ECM and its 3D organisation *in vivo* are complex and as such represent a significant challenge to replicate in an *in vitro* setting. Due to its experimental simplicity, 2D culturing of homogenous cell populations on glass or plastic coverslips has been a standard for the analysis of biological processes. However, these conditions limit cell dimensionality, heterogeneity, and adhesive properties, reducing them to an X-Y plane on abnormally stiff surfaces. As a result, they are also exposed to an excessive and physiologically irreproducible degree of cell spreading, and gradients of nutrients, oxygen, and molecules that do not recapitulate that seen *in vivo* (Pampaloni, Reynaud, and Stelzer 2007; Smalley, Lioni, and Herlyn 2006).

Plating cells onto varying topographically manipulated substrates such as collagen, hydrogels, or silicone, provides variable stiffness, topography, and chemical composition of surface to which the cells adhere, sometimes known as 2.5D cell culturing (Doyle et al. 2009; S. H. Lee, Moon, and West 2008; Lehnert et al. 2004; Sodunke et al. 2007). Using adaptable variations in geometry, size, stiffness, and patterning of these surfaces has demonstrated the importance of substrate topography on cell differentiation, proliferation, and apoptosis (Lehnert et al. 2004; Thé et al. 2006).

Migration of cells has been shown to follow gradients of increasing concentrations of chemical factors in the ECM, including those of ECM proteins such as collagen or fibronectin, known as haptotaxis, and stiffness in the ECM, known as durotaxis (Rozario and DeSimone 2010). This process relies on a balance of adhesion and deadhesion with the ECM sufficient to support cell-ECM traction forces; if adhesion forces are too low, no traction can be formed, if they are too high the cell becomes immobilised (Palecek et al. 1997). This effect can also be cell and ECM dependent as gradients of fibronectin but not laminin can promote migration (Hartman et al. 2017). Matrix stiffness and viscoelasticity can be controlled *in vitro* through a variety of mechanisms such as matrix density, degradation, and non-enzymatic glycation (Mason et al. 2013) which will be further expanded on later in this section.

A range of 3D biomaterials have been developed to analyse and validate migratory and adhesive mechanisms seen in 2D and 2.5D cultures in a more physiologically relevant context. The ability to control the local environment and composition of the 3D matrix is the main factor for using an *in vitro* system when attempting to analyse the dynamics of cellular adhesion and migration in 3D (Lutolf and Hubbell 2005). Many factors influence 3D cell migration such as porosity, adhesive ligand, cell type, and matrix substrate, such as collagen (Grinnell 2003), Matrigel (Kleinman and Martin 2005), engineered hydrogels (Burdick and Anseth 2002; J. S. Miller et al. 2010; Raeber, Lutolf, and Hubbell 2005) or self-assembling peptides (Mata et al. 2009; S. Zhang 2003).

Such *in vitro* 3D methods of cell culture using tunable, mechanical, and non-synthetic substrates enable the effects of matrix stiffness on single cells to be assessed. Changes in stiffness can be achieved in tissue through increased density of the matrix (Kniazeva and Putnam 2009; Shamloo and Heilshorn 2010) however this also changes levels of porosity and number of cell binding sites in the scaffold. Some materials allow stiffness to be varied independently of matrix density. These materials, such as synthetic PEG-hydrogels, lack the native structure and topography of ECM found *in vivo*. Alginate is another commonly used material for 3D cultures, but this cannot be remodelled by the cell as occurs in more physiologically biomaterials (Genes et al. 2004). By contrast, type-I collagen can be remodelled by cells as *in vivo* and can be stiffened through the process of non-enzymatic glycation by molecules such as ribose. This process has been shown to induce ECM stiffening in ageing, diabetes, and cancer (Reigle et al. 2008; Yan et al. 2003).

Using this naturally occurring process of non-enzymatic glycation, methods for increasing stiffness of the matrix have been used to circumvent problems with changing the density of the matrix and use of less physiologically relevant synthetic materials. Using non-enzymatic glycation increases the stiffness of the matrix while maintaining a consistent porosity and number of binding sites for cells to engage with. It acts through a sequence of chemical reactions known as the Maillard reaction

(Ulrich and Cerami 2001). This is the process wherein reducing sugars form Schiff bases along with amino groups on proteins rearrange into Amadori products. Amadori products go on to form advanced glycation end products that cause increased crosslink formations on proteins (Hemmler et al. 2018; Hodge 1955).

Previous experiments have used glycation to stiffen the matrix during the polymerisation process, creating a hyperosmotic matrix enabling only the culturing of cells on the surface of the gels, not embedded within them. The injection of cells into pre-polymerised collagen matrices results in the disruption of the matrix architecture and inability to visualise evenly distributed single cells (Francis-Sedlak et al. 2009; Gostynska et al. 2017). However, the glycation of collagen immediately prior to its polymerisation enables the equal distribution of single cells at the desired concentration throughout the matrix and circumvents damage induced by injecting cells into pre-polymerised scaffolds (Mason and Reinhart-King 2013). A simplified graphical representation of the different methods in cell culturing and the mechanism in which non-enzymatic glycation induces increasing stiffness in matrices of the same collagen concentration can be found in **Figure 1.6**.

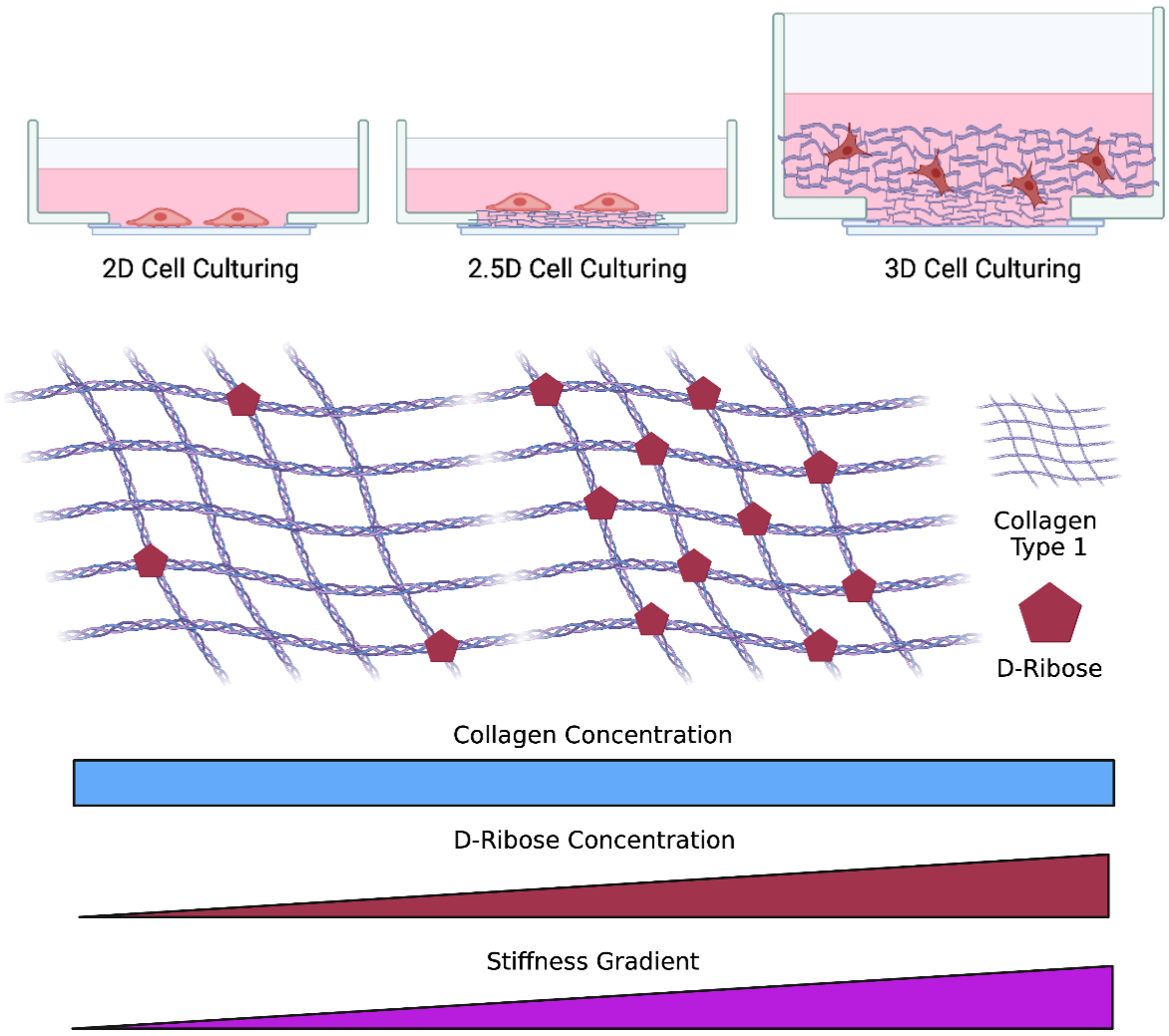

Figure 1.6 – Different methods in cell culturing and collagen-ribose matrix composition
Simple schematic of methods in techniques of single cell culturing. 2D single cells (Left) are platted on abnormally hard substrates such as glass and plastic. Single cells platted in 2.5D (Middle) are cultured on different biological substrates offering reduced stiffnesses and 3D structures over which to adhere and migrate. 3D single cells embedded in biological substrate (Right), such as collagen, offer a more physiologically relevant mechanical, adhesive, and structural properties. A schematic representation of collagen matrices of the same concentration with increasing levels of non-enzymatic glycation shows increased levels of stiffness coupled with increasing concentration of D-ribose. Created with BioRender.com.

1.5 Microscopy techniques for 3D single-cell imaging

Fluorescence microscopy, in which a sample is labelled with one or more fluorophores, is a routine method in most biological research laboratories. Fluorophores such as GFP can be used to label specific proteins in live cells, enabling their dynamics, subcellular localisation, and relationship to cell behaviour to be quantified (Lichtman and Conchello 2005). Fluorophores absorb light at one wavelength and emit light at another, longer wavelength. Use of specific wavelengths to excite and capture fluorophores results in high contrast images, unlike those achieved using transmitted light.

A range of different types of fluorescence microscopy exist, offering different resolution and sensitivity. Widefield microscopy is the simplest type, is relatively cheap and is widely used in most cell biology labs. Widefield microscopes excite the entire specimen and capture an image of the specimen using a camera. Although this approach can be useful for low resolution, 2D live imaging, widefield microscopy captures both in- and out-of-focus light, and therefore has a substantial disadvantage that the areas above and below the focal plane dominate over the in-focus signal. In thicker samples, the problems with of the out-of-focus light are amplified even further due to increased scatter and reduced penetration depth resulting in blurred images. Thus, although widefield microscopy can be helpful for some applications, it is unsuitable for 3D imaging in live or fixed specimens (Laurent et al. 1992).

Point-scanning microscopy techniques, such as confocal laser scanning microscopy (CLSM), provide better means to image complex 3D cell and ECM structures as out-of-focus light is removed. The CLSM captures the sample using point scanning illumination and eliminates out-of-focus light using a pinhole (Elliott 2020). Photomultiplier tubes are used to detect diffraction-limited volumes within focal planes coupled with high optical sectioning offering good depth and Z-resolution for the reconstruction of 2D images into 3D (Sheppard 2021). However, as CLSM produces images voxel by voxel in X, Y and Z, it greatly increases the duration of acquisition and exposure time of the sample to light. The high photon dependency of CLSM when imaging further into the sample, results in an increased level of

excitation required that can in turn increase the rate at which bleach occurs through the sample (Hell et al. 1993; Wang, Babbey, and Dunn 2005). CLSM still remains one of the most common methods for acquiring 3D samples due to its ability to penetrate samples and limit the excitation volume, but is less suited to more sensitive, live samples.

In live imaging, toxicity can be reduced by sampling fewer Z-planes (thus with lower Z-resolution) or increasing time between images. However, reduced temporal and Z-resolution can both result in errors in tracking objects over time and co-localization between different wavelengths (Comes et al. 2019). Adequate depth penetration into the sample requires increasing the working distance of the objective, which reduces magnifications achievable, and the amount of scattering observed. The scattering of light combined with interference from structural components results in out-of-focus fluorescence and a reduced signal-to-noise ratio. To reduce the signal-to-noise ratio, higher laser power can be used; however, over time, prolonged or repetitive exposure to light across multiple Z-planes and across multiple wavelengths leads to exponentially higher levels of photobleaching and phototoxicity. Photobleaching is the irreversible quenching of fluorescence in a sample that occurs due to the reaction between the excited fluorophore and oxygen, producing possibly toxic levels of reactive oxygen species (ROS) (Stephens and Allan 2003). Highly reactive, these ROS disrupt normal cellular function and can interfere with the natural mechanism attempting to be quantified. The imaging of 3D samples therefore requires the trade-off between multiple colour channels at a high temporal and axial resolution to capture the rapid dynamics of cells at the appropriate scale, without causing irreversible and damaging levels of photobleaching, impacting normal cell behaviour, or inducing cytotoxicity.

Instant structured illumination microscopy (iSIM) allows for the imaging of samples at higher speed and reduced levels of bleaching and phototoxicity due to its ability to acquire the total plane of view at a higher speed and reduced laser power than CLSM. By passing the laser beam through a converging microlens array and a galvanometric mirror, the iSIM scans a multifocal beamlet array across the sample.

This illuminates the imaging field with a converging laser beam. As a result of the multifocal fluorescence from the sample being rotated through a pinhole, out-of-focus fluorescence is eliminated. A second microlens array is used to contract each focal point twice, offering a two-fold improved resolution to that of widefield microscopes, a maximum Z-resolution of 280 nm and allowing instant visualisation of the entire field of view as opposed to the point-scanning method used in CLSM (Curd et al. 2015; Gustafsson 2000; Zhovmer and Combs 2021).

As iSIM utilizes optical hardware to image samples, it allows for high-speed, super-resolution imaging of biological samples in real time, without the need for specific fluorophores and over a large volume of interest (Winter et al. 2014; York et al. 2013). However, the illumination is still imposed across the entirety of the sample during imaging. This causes unnecessary photon excitation throughout the entire sample despite only capturing the focal plane of interest. The ability to reduce the effect of photobleaching and phototoxicity is limited by the nature of the illumination.

Lattice light sheet microscopy (LLSM) implements light sheet illumination to avoid excessive photon activation outside the in-focus area of interest. The illumination in a form of a Bessel beam, propagates indefinitely without changing its cross-sectional profile, which extends infinitely in X and Y thereby producing a sheet of light at the focal point. This enables capture of fluorescent signals perpendicular to the X-Y plane without unnecessary illumination of the sample in regions outside the plane of focus. Because excitation is limited to just the focal plane, the entire plane is detected instantly and reduces the amount of photobleaching that occurs outside of that region. This enables 3D cell samples to be captured at high signal-to-noise ratios, high axial resolutions, and high temporal resolutions without causing high levels of bleaching or cytotoxicity to the cells (Chen et al. 2014).

Both the iSIM and LLSM offer improvements in isotropic resolution and reduce the time it takes for data to be acquired all the while reducing bleaching and toxicity to live samples, advancing the field of live cell imaging. A simplified graphical

representation of the different illumination methods of point-scanning confocal, iSIM and LLSM are shown in **Figure 1.7.**

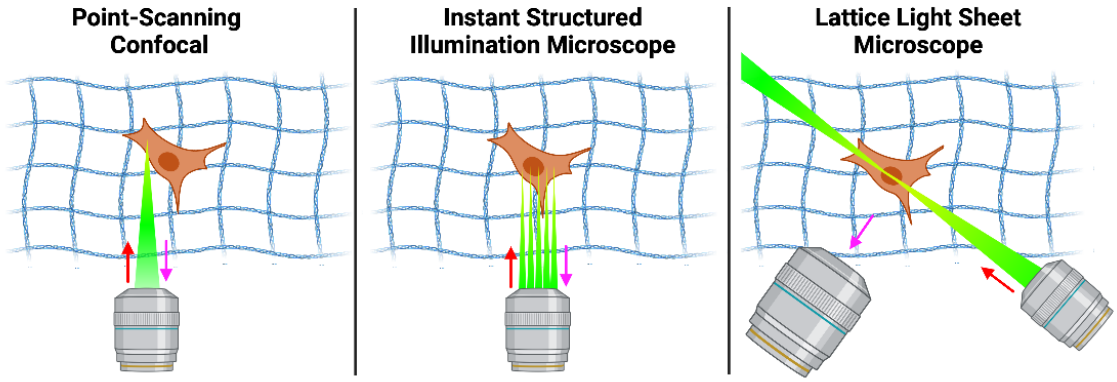

Figure 1.7 – Different methods of microscopy illumination for 3D samples. Simple schematic comparing methods in techniques of microscopy illumination between point-scanning confocal (Left), iSIM (Middle) and LLSM (Right). Red arrows point to direction of excitation beam and magenta arrows point to direction of emitted light. Point-scanning confocal systems illuminate samples point by point using a laser, with excitation above and below the focal point determined by objective lens working distance, while emission is collected primarily with a photomultiplier tube (PMT) behind a pinhole to exclude out-of-focus light. iSIM generates a set of beamlets by a lenslet array and focussed onto a sample. The resulting fluorescence image is passed through a set of pinholes to reject out of focus light, and then passed through a second lenslet array that focusses the beamlets. LLSM produces a sheet of light which extends across the focal plane being captured perpendicular to the X and Y plane. Created with BioRender.com.

These advances in live cell imaging have been utilised in recent years to dissect a more comprehensive understanding of 3D structures. The iSIM, through its abilities in rejecting out-of-focus light, multi-colour fluorescence imaging, standard dye compatibility, and depth penetration into 3D samples, with advanced acquisition speed and spatial resolution, has been used to image the cytoskeleton in red blood cells and fibroblast in 3D collagen gels (York et al. 2013). The LLSM, offering the same benefits as the iSIM but with more reduced phototoxicity to live samples due to the Bessel beam illumination method, has imaged sub-cellular dynamics in 3D over long time periods (Chen et al. 2014). However, no one has yet to apply the benefits of the iSIM and LLSM to the study of biochemical and biomechanical dynamics of

cancer cells and their relation the ECM. Using these approaches might help provide further insight into the detailed mechanisms that underpin cell invasion in 3D matrices of differing stiffnesses.

1.6 Hypothesis & Aims

We hypothesise that increasing stiffness of the ECM leads to increased cell migration through enhanced protrusive activity and actin dynamics to better impose traction and remodelling of the surrounding matrix.

The experiments in this thesis are designed to address the following aims:

1. Development and characterisation of a reproducible *in vitro* method for 3D single cancer cell culturing in collagen matrices of varying stiffnesses.
2. Characterisation of single cell cytoskeletal behaviour due to variations in matrix stiffness.
3. Investigating the cytoskeletal mechanisms used by single cells to remodel the surrounding matrix over time at different stiffnesses.

2 Material and Methods

2.1 Reagents and Plasmids

Table 2.1.1- Cell Culture Reagents

Reagents	Source	Reference
4-(2-hydroxyethyl)-1-piperazineethanesulfonic acid (HEPES)	Sigma	H0887
Cy3 mono-reactive dye	Cytiva	PA23001
D-Ribose	PanReac AppliChem	A2219
Dimethyl Sulfoxide anhydrous desiccate (DMSO)	Molecular probes	D12345
Dimethyl Sulfoxide (DMSO) (Freezing cells down)	Sigma	D2650
Dulbecco's Modified Essential Medium (DMEM)	Gibco	D6046
Fetal Bovine Serum (FBS)	Gibco	SV30160.03
Fibronectin	EMD Millipore Corp.	FC010
Imidazole	Acros Organics	122021000
L-glutamine	Gibco	2503-024
Lipofectamine 3000	Invitrogen	L3000-008
Sodium Chloride (NaCl)	Sigma	S3014
Opti-MEM	Gibco	11058021
Penicillin/Streptomycin	Sigma	P0781
Phosphate Buffered Saline (PBS) with calcium chloride and magnesium chloride	Sigma	D8662

Phosphate Buffered Saline (PBS) without calcium chloride and magnesium chloride	Sigma	D8537
Polybrene (Hexadimethrine bromide)	Sigma	107689
Polyethyleneimine (PEI)	Alfa Aesar	43896
Rat Tail Collagen I, High Concentration	Corning	354249
Sodium Bicarbonate	Sigma	S6014
Tris Hydrogen Chloride	G Sciences	RC-108
Trypsin/EDT	Sigma	T4174

Table 2.1.2 - Molecular Biology Reagents

Reagents	Source	Reference
Kanamycin	Sigma	BP861
isopropyl β-D-1 thiogalactopyranoside (IPTG)	Sigma	I6758
Luria-Bertani (LB) Agar and Broth	Sigma	L7025

Table 2.1.3 - Biochemical Assay Reagents

Reagent	Source	Reference
Bovine Serum Albumin (BSA)	Roche	BSAVHS-RO
Immersion oil	Zeiss	5101
Paraformaldehyde (PFA)	Sigma	93443
Triton X-100	Sigma	93443

Table 2.1.4 - Antibodies

Class	Antibody	Dilution	Source	Reference
Dye	Alexa647 NHS Ester (Succinate Ester)	2μg/μl	Invitrogen	A37573
Dye	Cy3	0.2mg/mL	Cytiva	PA23001
Dye	CNA35-EGFP	1μM	Addgene	Plasmid #61603
Dye	DAPI	1:500	Sigma	D9542
Dye	Phalloidin 568	1:500	Invitrogen	A12380

Table 2.1.5 – Imaging Plates, Tissue Culture Dishes and Coverslips

Material	Source	Reference
Ibidi Angiogenesis slide	Ibidi	81506
Ibidi µ-Dish 35 mm, low (polymer coverslip)	Ibidi	80136
5-mm-diameter cover slips	Warner Instruments	64-0700
T25 cm2 flasks	Cellstar	690175

Table 2.1.6 - Expression Plasmids

Plasmid	Type	Insert and Tag	Source
Lifeact-mScarlet	Lentiviral	LifeAct – an actin filament reporter, mScarlet tag	Gift from Campbell Lawson
CNA35-EGFP	Plasmid	pET28a-EGFP-CNA35	Gift from Maarten Merkx (Addgene plasmid # 61603 ; http://n2t.net/addgene:61603 ; RRID:Addgene_61603)

2.2 Methods

2.2.1 Molecular Protein Expression and Purification

2.2.1.1 Collagen Binding Protein – CNA35-EGFP

Collagen binding CNA35-EGFP was amplified, induced, and purified as detailed by *S. Aper et al. 2014*. E. coli BL21(DE3) competent bacteria encoding protein CNA35-EGFP were spread on kanamycin (50 μg/mL) Luria-Bertoni (LB) agar plates and incubated at 37°C overnight. Single colonies were picked to inoculate 8 mL LB medium cultures (10 g/L peptone, 10 g/L NaCl, 5 g/L yeast extract) with 30 μg/mL Kanamycin. Bacteria were grown overnight at 37°C and 250 rpm. Cells were then transferred to 400 mL LB 30 μg/ml Kanamycin medium cultures and further grown at 37°C and 250 rpm till optical density of 600 nm reached 0.6. Expression was induced by adding 0.5 mM isopropyl β-D-1 thiogalactopyranoside (IPTG) and performed for 20 hours at 25°C and 250 rpm. Bacterial harvesting was done by centrifuging for 10 min at 10,000 g. Pellets were resuspended in 8 mL Bugbuster (Novagen) supplemented with 8 μL Benzonase (Novagen) and incubated for 40 min at room temperature for protein extraction. Suspension was further centrifuged for 20 min at 16,000 g. The soluble fraction containing protein CNA35-EGFP was purified via Ni^{2+} affinity chromatography using the N-terminal 6xHis-tag. Chromatography column was loaded and washed through with washing buffer (20 mM Tris-HCl, 0.5 M NaCl, 30 mM imidazole) at pH 7.9. The soluble fraction of CNA35-EGFP kept on ice was loaded onto the column and washed with 8 column volumes of wash buffer. The His-tagged protein was eluted with elution buffer (20 mM Tris-HCl, 0.5 M NaCl, 500 mM imidazole) at pH 7.9. The eluted protein was kept away from light and on ice. Eluted protein was repeatedly concentrated using Amicon Ultra-4 Centrifugal Filter Units, frozen in liquid nitrogen and stored at -80°C.

2.2.2 Cell Culture

2.2.2.1 Cell Lines

Human cervical cancer cells (HeLa) and Human Embryonic Kidney Cells 293 (HEK-293T) cells were cultured in high glucose Dulbecco's Modified Eagle Media (DMEM) supplemented with 100 units/mL Penicillin and 10 mg/mL Streptomycin (PS), 10%

v/v heat-inactivated Foetal Bovine Serum (FBS) and 2 mM L-Glutamine (L-Glu). Cells were cultured in T25 cm^2 flasks and incubated at 37°C and 5% CO_2 in a sterile humidified incubator.

Cells reaching a confluence of 80-90% were passaged with Trypsin at 0.05% in EDTA diluted in Phosphate-Buffered Saline free of magnesium and calcium (PBS), for 5 min at 37°C. Once cells fully detached, complete DMEM was added to neutralize trypsin and centrifuged at 1200 rpm for 3 min in 15 mL tubes. The supernatant was aspirated, and cells resuspended in complete DMEM.

To freeze down cells, $1x10^6$ cells were suspended in 0.5 mL of cold DMEM, 0.4 mL FBS and 10% DMSO in cryovials over ice. Cryovials were frozen down at -80°C for two days before being transferred to liquid nitrogen storage.

Thawing of cells from 1 mL cryovial were defrosted at 37°C until fully thawed out. Cells were resuspended slowly in 10 mL of warmed complete DMEM and centrifuged at 1200 rpm for 3 mins. The resulting supernatant was aspirated, and cell pellet resuspended in 5 mL complete DMEM before being plated into a T25 cm^2 flask and incubated at 37°C and 5% CO_2 in a sterile humidified incubator.

2.2.2.2 Generation of Lentivirus stable cell lines with HEK 293T cells

Lentivirus construct of lifeact-mScarlet was generated using T25 cm^2 flask of HEK-293T cells at 30-40% confluence. HEK-293T cells were transfected with 0.9375µg of pMDG (viral envelop), 2.8125µg pD8.91 (viral packaging), 3.75µg of desired LNT vector (lifeact-mScarlet) and 22.5µg PEI in 500µl of Opti-MEM after 15 minutes incubation at room temperature. The DNA/PEI mixture was added to T25 cm^2 flask with 2 mL of complete DMEM for 6 hours at 37°C. DNA/PEI media was removed and replace with 3 mL Opti-MEM for 48 hours to collect generated lentivirus construct. Opti-MEM with Lentivirus was collected, centrifuged at 2000 rpm for 5 minutes and filtered through 0.22um filter to catch any remaining debris. Virus was stored at -80°C in cryovials or applied fresh to HeLa cells.

2.2.2.3 Lentivirus infection of HeLa cell lines

HeLa cell line were platted into T25 cm2 flasks and grown to 30-40% confluence. Complete media supplemented with 1/1000 polybrene (8 mg/mL) along with mScarlet lifeact lentivirus was added to HeLa flask for 24 hours at 37°C in a humidified sterile incubator. Media containing virus was removed and replaced with complete DMEM. Cells were passaged 2 more times to remove any remaining lentivirus particles. Highly expressing HeLa lifeact-mScarlet cells were selected for homogeneity from the top 30% according to fluorescent intensity of expressing. Sorted cells were grown in T25 cm^2 flasks and amplified for experimental use and freezing down.

2.2.2.4 Plating cells in 2D

Dishes and coverslips for 2D cell plating were initially coated in 1/1000 high concentrated collagen diluted in Opti-MEM and 0.1% acetic acid solution. Dishes were incubated 30 min at 37°C and washed 3 times 5 minutes with PBS before drying. Cells were then platted at the required density for 2D imaging.

2.2.3 3D Collagen-Ribose Matrices

2.2.3.1 3D collagen-ribose matrices.

Type-I highly concentrated collagen isolated from rat tail tendon extracted in 0.02N Acetic Acid with a stock solution of approximately 10 mg/mL was used to recreate a reproducible and stable replica for *in vivo* ECM. To mimic changes of stiffness in the ECM, without affecting changes to the topography, D-ribose was used to non-enzymatically glycate collagen for 30 min on ice prior to gel polymerization, for 3 final collagen-ribose matrices of 0-, 50- and 200-mM ribose (Mason et al. 2012).

Matrices of different ribose concentrations were prepared on ice with a final collagen concentration of 2 mg/mL, 20 mM HEPES, 100 μg/mL fibronectin, 0.3% $NaHCO_3$ (w/v) and 14.5 mM NaOH in complete Opti-MEM (± $2x10^5$ Cells). Collagen-ribose mix was left to polymerize for 30 minutes at 37°C before adding 3 10 min washes of PBS before adding complete Opti-MEM. Schematic representation **Figure 2.1.**

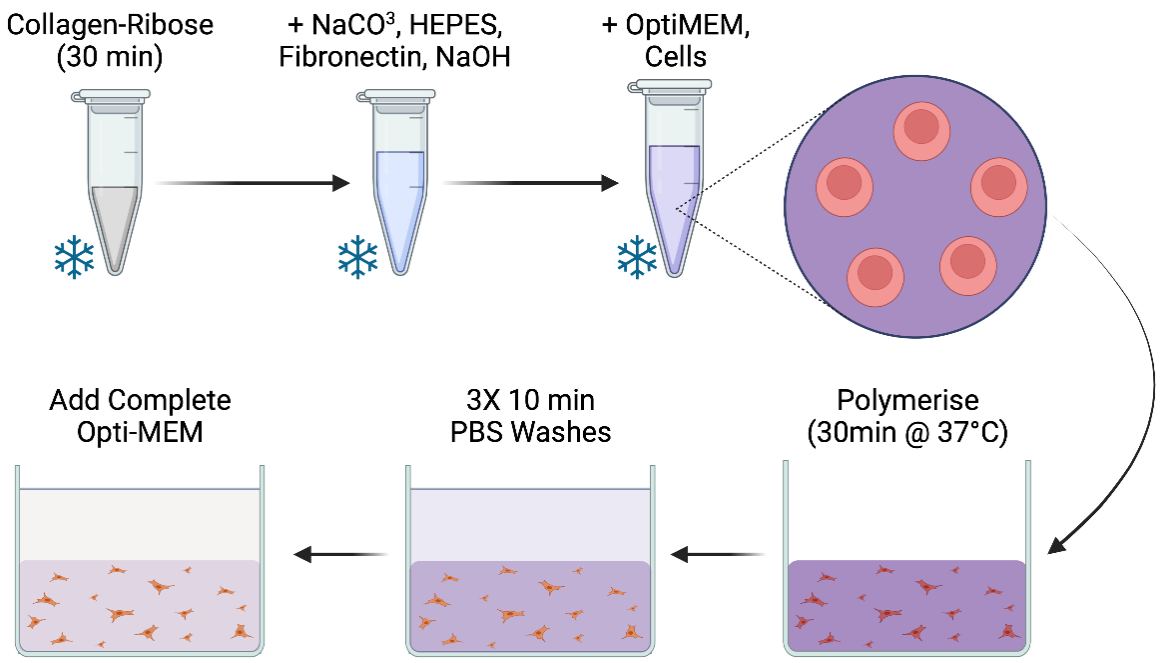

Figure 2.1 – Schematic for embedding single cells in polymerising collagen-ribose matrices.
The collagen-ribose mix is left on ice for 30 minutes, for non-enzymatic glycation. Polymerisation inducing buffer is added to neutralize pH of mix, followed immediately by cells suspended in Complete Opti-MEM whilst all the time on ice. Total mix is carefully homogenised on ice while carefully avoiding disturbances and bubbles. Plate required volume in/on desired dish or coverslip and leave to polymerise for 30 minutes at 37°C. Once polymerised, three PBS washes (without magnesium chloride and calcium chloride) for 10 minutes is performed to remove any unattached dye. Finally add complete Opti-MEM before imaging. Created with BioRender.com.

2.2.3.2 Post-polymerisation matrix and cell staining.

Cells and collagen gels were fixed for 30 min in 4% Formaldehyde (PFA, PeqLab-30201) at 37°C and washed 3 times with PBS. Cell samples were permeabilized with 0.1% Triton (Sigma-T9284) in PBS for 1 hour and blocked-in blocking buffer (3% Bovine Serum Albumin (BSA), 0.1% Triton in PBS) for 1 hour at 37°C. Following blocking, dyes were added to blocking buffer at the desired dilution and incubated with sample overnight at 4°C before being washed three times 10 minutes in PBS. Samples were stored and covered with PBS at 4°C until imaged.

2.2.3.3 Pre-polymerisation fluorescent labelling techniques of collagen-ribose matrices.

In order to clearly visualise the topography and dynamics of collagen matrices, several collagen labelling techniques were applied with the aim of not implicating changes in the matrix structure or stiffness. The goal is to allow a systemic and reproducible method of study for clear fluorescent collagen labelling whilst also being compatible for the simultaneous imaging of live cells and their behaviour.

2.2.3.3.1 Collagen Binding Protein CNA35-EGFP use for pre-polymerisation labelling.

Concentrated CNA35-EGFP was used at 1 μM and added with the collagen polymerising buffer solution. Once collagen matrix fully polymerised, three 10 min PBS washes were performed gently to clear any unbound dye before adding complete Opti-MEM.

2.2.3.3.2 Cy3 Mono-reactive Cyanine Dye of Rat Tail Collagen Type 1.

Amersham Cy3 Mono-reactive Cyanine Dye (Cy3) was used on ice for 1 mg rat tail collagen type 1 and 0.1 M $NaHCO_3$ solution (pH 9.3 in Opti-MEM, 0.2 μm sterile filter). Cy3 solution was primarily solubilised in $NaHCO_3$, vortexed and incubated on ice till cold. Collagen was pipetted into Cy3- $NaHCO_3$ solution for a final volume of 1 mL, avoiding bubbles and exposure to light before incubating on a roller for 1 hour at 4°C. Cy3 solution was added to 8kDa molecular weights cut off dialysis tube with polystyrene floating cap and inverted for dialysis. Cy3 solution was dialysed in 500 mL of 0.1% Acetic Acid dH20 for 2 hours at 4°C, 500 mL 0.1% Acetic Acid dH20 overnight at 4°C and finally 500 mL 0.1% Acetic Acid in PBS overnight at 4°C. Cy3 collagen solution is stored at 4°C protected from light.

Pre-stained collagen was added at 1:3 Cy3 to collagen ratio before ribose incubation on ice, adapted to maintain a final concentration of 2 mg/mL collagen-ribose solution.

2.2.3.3.3 Alexa-647 NHS Ester (Succinimidyl Ester) fluorescent labelling of collagen-ribose matrices pre-polymerisation.

Alexa-647 NHS Ester (Succinimidyl Ester) (Alexa647-SE) stock solution was dissolved in DMSO to 2 μg/μL. Alexa647-SE was used at 0.4 μg/ mg of collagen and added with polymerisation buffer solution. Once collagen matrix fully polymerised, three 10 min PBS washes were performed gently to clear any unbound dye before adding complete Opti-MEM. Alexa647-SE DMSO stock solution is viable for 3-months before inconsistencies in fluorescence begin to occur.

2.2.4 Atomic Force Microscopy

2.2.4.1 AFM dish preparation for collagen-ribose matrix stiffness measurements.

Ibidi μ-Dish 35 mm with a polymer coverslip were scored using a scalpel down the centre and across half the dish, careful not to cut through the bottom of the dish. 200 μL of made-up of liquid collagen-ribose was platted over the scored half of the dish and allowed to fully polymerise before performing PBS washes and adding Opti-MEM, as stated above. Scoring of the dish provides a greater 3D surface upon which to allow the collagen-ribose matrix to polymerise, greatly reducing the likelihood of the collagen detaching from the dish bottom. Samples were left unfixed to not induce additional crosslinking and changes in sample stiffness.

2.2.4.2 Atomic Force Microscopy collagen-ribose matrix imaging.

AFM images containing stiffness data was obtained using Nano Wizard 3 AFM (JPK Instruments). The whole AFM system kept in an isolation cupboard, a Halcyonics i4 vibration isolation system, to minimise the effects of ambient vibrations on the readings obtained from the cantilever tip. The cantilevers used in all AFM experiments were SD-qp-SCONT-TL-10 with a PPMA bead at 5μm radius glued to the end with an approximate spring constant of 0.013N/m taken in liquid prior measurements. This enables the measurement of the collagen meshwork as opposed to individual fibres. Images were recorded on quantitative imaging (QI) mode, which records a complete force-distance curve for each pixel without exerting lateral forces on the sample. The set point was set at 1nN, 10 μm Z length at a

2μm/s extension speed. The cantilevers were calibrated by measuring the thermal fluctuations within. Schematic representation **Figure 2.2.**

Thank you to Ishan Costello and Liisa Hirvonen for their collaboration and help with all the work done on the AFM.

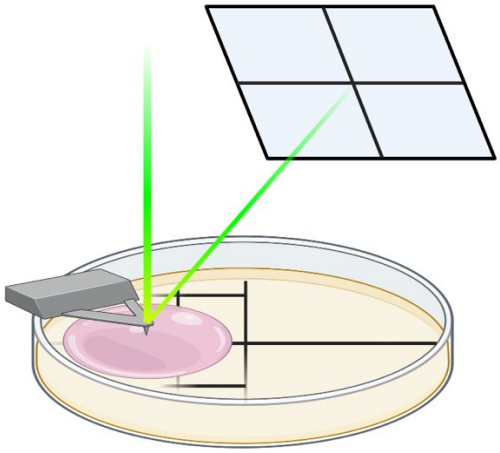

Figure 2.2 – Simplified schematic of AFM method for sample measurement. Collagen-ribose matrix free of cells, pink, was allowed to polymerise around scratches made on coverslip, black lines. Sample was measured by laser movement off AFM cantilever as it touches down on the sample. Created with BioRender.com.

2.2.5 Instant Structured Illumination Microscope

2.2.5.1 iSIM Angiogenesis plates preparation for 3D collagen-ribose matrices imaging.

Ibidi Angiogenesis plates were used for iSIM fixed and live cell imaging of 3D collagen-ribose matrices. 10 μL of liquid collagen-ribose mix was left to polymerize for 30 minutes at 37°C before adding 3 times 50 μL of PBS and final 50 μL of complete Opti-MEM for imaging.

2.2.5.2 Capturing 3D dynamics of single HeLa cells in collagen-ribose matrices using iSIM.

Live 3D collagen-ribose matrices were imaged using Visitech iSIM module mounted to Nikon Eclipse-Ti2 inverted microscope within a humidified chamber maintained at 37˚C. Collagen-ribose matrices and HeLa lifeact-mScarlet samples were imaged

using 40x WI (NA 1.3) and 60x oil (NA of 1.2) and post-magnification of 1.5 used. Excitation wavelengths used were 488 nm for CNA-35 EGFP, 561 nm for HeLa mScarlet and 641 nm for Alexa647-SE. Colour images were imaged consecutively in order to gain in imaging acquisition speed.

Live 3D imaging of single cells across 0-, 50- and 200-mM collagen-ribose matrices were imaged at 1-hour post polymerisation with a temporal resolution of 10-minutes for a period of 3 hours. Laser power and exposure time was optimised for increased acquisition speed through Z, fluorescence intensity, reduced bleaching and minimum phototoxicity across both colour channels. NIS-Elements imaging software (**Table 2.3.1**) was used to capture images and save in .nd2 format. During acquisition NIS-Elements software is used for multiple single cell location positioning in X, Y and Z to capture total cell and surrounding collagen over time. Imaging of Z-stack was carried out at 1 μm spacing with 25 μm above and below the cell for a total of 51 Z-slices over 50 μm.

Thank you to the Nikon Centre for their help on the work done using the iSIM.

2.2.6 Lattice Light Sheet Microscopy

2.2.6.1 LLS 5-mm coverslip 3D collagen-ribose matrices preparation.

5-mm coverslips for lattice light sheet were initially coated in 1/1000 high concentrated collagen diluted in Opti-MEM and 0.1% acetic acid solution. Coverslips were incubated 30 min at 37°C and washed 3 times 10 minutes with PBS before drying. 14 μL of made-up liquid collagen-ribose matrices, as specified above, were carefully pipetted as to not collapse over edges of dried coverslip and allowed to fully polymerise away from any vibrations or possible shocks. Once fully polymerised, gently perform PBS washes and add complete Opti-MEM to not dislodge sample from coverslip.

2.2.6.2 Capturing 3D dynamics of single cells in collagen-ribose matrices using LLS microscope.

A Janelia Lattice Light sheet, built by the Microscopy Innovation Centre (MIC) at King's College London, was used to perform high temporal resolution, low-

phototoxicity live cell imaging (Chen et al. 2014c). A fast-switching spatial light modulator (SLM) diffracts incident light to produce a light sheet based on previously calculated binary phase patterns for each wavelength. The excitation objective (Special Optics custom, NA 0.65) and the detection objective (Nikon Apo LWD 25xW, NA 1.1) are suspended from above at an angle of 31.5 degrees with respect to one another, with their ends dipped in a media-filled and temperature-controlled bath. The lattice light sheet created in the XY plane at their common foci intersects the specimen obliquely. Excitation and emission lines: Ex 560 nm - Em 600-25 nm; Ex 642 nm - Em 677-25 nm. As the specimen is moved through the light sheet, fluorescence is recorded as a series of 2D images on a Hamamatsu Orca Flash 4.0 v2 sCMOS camera with an effective magnification of 62.5X. These are then deskewed, deconvoluted and assembled into a 3D image, with this process repeated to build a 4D data set. Images were saved in .tif format.

Samples were imaged at 30 second temporal resolution over 30 minutes at the maximum X (512 pixels), Y (512 pixels) and Z (200 slices) limitations of the LLS.

Thank you to Dylan Herzog and MIC for their help and collaboration on all the work done with the LLS.

2.3 Data Analysis

2.3.1 Software

Table 2.3.1 - Software

Software name	Source
Alignment Fourier Transform	Developed by OakesLab and Stramer lab KCL.
Correct 3D Drift	https://imagej.net/plugins/correct-3d-drift (1.0.6)
Fiji	Open-source platform for biological image analysis (Schindelin et al., 2012)
JPK System	JPK NanoWizard 3
Matlab	MathWorks 2020b
NIS-Elements imaging software	Nikon Version 4.51.01
2D Particle Image Velocimetry	Developed by Stramer lab KCL.

2.3.2 Collagen Volume Fill Analysis

Raw 3D images of collagen colour channel were imported into Fiji. A gaussian filter of 10 pixels was applied to a duplicate and subtracted from the original 3D image in Fiji to remove background. 3D processed images were measured across stack with 'Measure Stack' plugin, providing an output of % Area and used to calculate % total Volume Fill.

2.3.3 AFM curve analysis for collagen matrices.

The Young's Modulus of collagen-ribose matrices were extracted by Hertz model fitting method on the top 10% of the AFM indentation curve (Highlighted with red

circle in **Figure 2.3**) using the JPK AFM software (**Table 2.3.1**). Hertz fitting was performed on the top 10% of the extension curve to remove indentations along the curve when breaking past different viscoelastic barriers of the matrix (Highlighted with green circle in **Figure 2.3**) from model fitting calculations. Each curve was visually checked to verify a clean contact point (orange arrow), extension, and retraction curve with no interference from unpolymerized collagen debris or fibre attachments. Information on the adherence of substrate can be found highlighted in the purple circle.

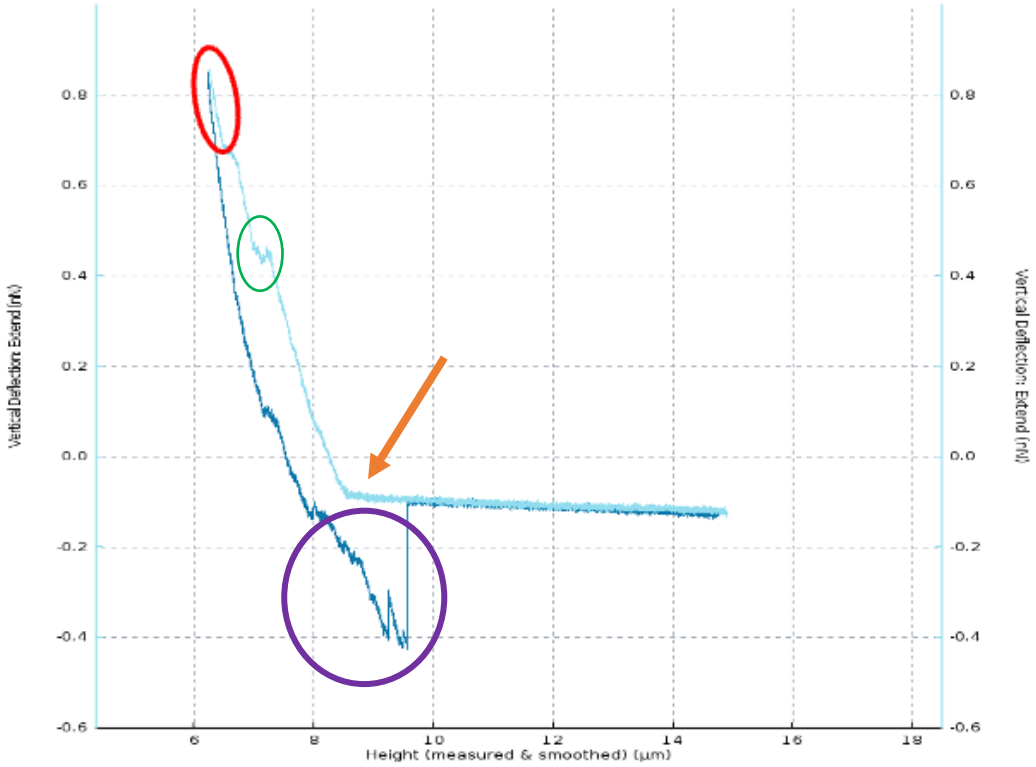

Figure 2.3 – Example AFM Force-Distance Curve measurement of collagen-ribose matrix.
Consists of Height (µm) and Vertical Deflection (pN). Extension curve in light blue, retraction curve in dark blue, point of resistance highlighted by red circle, contact point shown by orange arrow and adhesion properties highlighted by purple circle. Points of viscoelastic deformation highlighted by green circle.

2.3.4 LLS raw data deconvolution and deskewing.

Janelia open-source executable code was used for post-acquisition deconvolution and deskewing of data produced by the lattice light-sheet microscope. This software

was developed by Eric Betzig's group at HHMI's Janelia Research Campus (cudaDeconv, Janelia, 2007).

2.3.5 Single Cell Surface Area to Volume Ratio Measure and Object Centroid.

Raw 3D images of HeLa lifeact-mScarlet cells were imported into Fiji. A Gaussian of 100 pixels was applied to a duplicate and subtracted from 3D image with a Gaussian of 2 in Fiji to best remove background and create the clearest segmentation for thresholding the cell membrane. Processed image was converted to 8-bit image and set to a threshold of 8-255 for a binary image. Fill Holes package was applied and particles8 package used to filter out all objects no connected to main body of cell leaving one binarized 3D object. The 3D Object Counter plugin provides a measurement of Surface Area in μm^2, Volume in μm^3 and the X, Y and Z coordinates of object centroid.

2.3.6 4D Drift correction of iSIM and LLSM Image Samples in Fiji.

4D images acquired with the iSIM and LLSM of cell and collagen were imported and run through ‘Correct 3D Drift’ Fiji plugin. Drift correction was done on the collagen channel consisting of feature rich structure across the entire image and entirety of time points across all 3 dimensions. The cell was corrected using the drift measured tantamount collagen channel. The drift parameters were selected to include the maximum level of drift seen over time. Maximum Intensity Projections (MIP) were performed off these drift-corrected images.

2.3.7 Alignment Fourier Transform

Alignment Fourier Transform (AFT) was used as a method to quantify the degree of alignment in fibrillar structures seen across the ECM. AFT measurements were performed in MATLAB on the MIP through Z of drift-corrected collagen images. Parameters with a window size of 8.5 μm, an overlap of 50% and a neighbourhood radius of 2 vectors were selected. Images of vectors overlayed on raw image and the corresponding angle heatmap were saved as tiff. Order parameter of the AFT analysis representing the angle between the orientation of a central reference vector

and its neighbours. The order parameter represents values between -1 and 1, with 1 representing perfect alignment, 0 random orientation, and -1 opposite alignment. AFT code available at https://github.com/OakesLab/AFT-Alignment_by_Fourier_Transform.

2.3.8 2D Patchwork Cross-Correlation and Flow Speed Quantification.

Post drift correction and MIP of time lapses, 2D collagen and cell images were run through a 2D patchwork cross-correlation code in MATLAB codified by Dr. Stefania Marcotti. This code analysis the cross-correlation between source ROI of 3 μm at T=n within a larger search ROI of 6 μm at T=n+1 across 2 μm grid points in X and Y. Displacements with a cross-correlation above a coefficient value of 0.3 were kept. This was run across the full time-lapse series to measure the speed of actin dynamics and collagen displacement as reflected by the measurement in μm/min. Flow speed between time points and average flow speed measures were extracted from interpolated data. 2D cross-correlation code available at https://github.com/stemarcotti/PIV.

Thank you to Stefania Marcotti for her advice on best input parameters for the quantification of collagen displacement by the cell on 2D MIP Time-Lapses.

2.3.9 3D Volume Cross-Correlation and Flow Speed Quantification.

Post 3D drift correction of time lapse series, 3D collagen tiff files were run through a 3D volume patchwork cross-correlation code created in MATLAB. This code analysis the cross-correlation between source ROI volume of 3 μm in X-Y and 5 μm in Z at T=n within a larger search ROI of 6 μm in X-Y and 10 μm in Z at T=n+1 across 2 μm grid in X-Y and Z. Displacements with a cross-correlation above a coefficient value of 0.3 were kept. This was run solely on the collagen channel across the full time-lapse series in 3D to measure the force imposed by the cell on its surrounding matrix as reflected by the measure of collagen displacement in μm/min. Flow speed between time points and average flow speed measures were extracted from interpolated data.

3D cross-correlation code available at https://github.com/alex0gorey/3D-Cross-correlation.git

2.3.10 Statistics

All statistical tests were performed using one/two-way ANOVA tests (GraphPad Prism). Error bars represent min to max, box-and-whiskers containing $25^{th}/75^{th}$ percentile, the median line and showing all data points. Significance was taken as $p<0.001$ (***), $p<0.01$ (**) and $p<0.05$ (*) and non-significance (ns) values with $p>0.05$ were assigned in figures as shown.

2.3.11 Supplementary Videos

Supplementary Videos can be found at this link: https://drive.google.com/drive/folders/1FwJnR4Vrxn_53ktcqa8L0fN2NeFJyN1U?usp=sharing

3 Characterization and mechanical properties of fluorescently labelled 3D collagen-ribose matrices on single cell morphology.

3.1 Introduction

The 2D culturing of homogenous cell populations on glass or plastic coverslips has been the long-standing standard for the analysis of biological processes. However, these conditions limit normal cell dimensionality, heterogeneity, and adhesive properties, reducing them to an x-y plane on abnormally stiff surfaces. The majority of investigations and publications into the role matrix stiffness plays in cell migration has largely been performed on the dynamics of 2D cells behaviour platted on synthetic surfaces. The plating of cells onto varying topographical substrates such as collagen, hydrogels, and silicone, provides 3D manipulability of the topography to which cells adhere but do not reflect the cell behaviour of a 3D environment. To validate any migratory and adhesive properties seen in 2D, the development of 3D biomaterials to modulate and control 3D matrix properties, structures and stiffnesses has opened the door to more physiologically accurate studies *in vitro*. The ability to control the local environment and composition of the 3D matrix is the main factor for using an *in vitro* system when attempting to analyse the dynamics of cellular migration in 3D. However, when moving to 3D cell culturing methods, more factors need to be considered, such as porosity, soluble gradients, adhesive ligands, 3D migration, cell type to matrix substrate and differences in stiffness, making it far more complex than 2D cell culture.

The mechanical, chemical, and biological properties of the ECM and its 3D organisation *in vivo*, are incredibly complex to replicate in an *in vitro* setting. The ECM has varying and unique local compositions, providing crucial biochemical and biomechanical cues to all tissues and organs, in multicellular organisms. The biomechanical properties of the ECM have been recognised to play various roles in mediating cell behaviour and health, required for cellular differentiation, proliferation, and homeostasis. This structural and chemical scaffold is therefore essential in the morphogenesis of tissue development. Different pathologies and their prognosis, such as cancer, are promoted by alterations in the natural stiffness of the ECM, influencing cell morphology, differentiation, traction force generation, focal adhesion formation and the dynamics of migrating cells.

For the simultaneous study of the effects of ECM on single cells, and vice versa, rat tail collagen-1 matrices provide a more compatible *in vivo* similarity of the ECM, being the predominant matrix protein in all tissues, and 3D collagen gels replicate many of the adhesive, topographical and structural properties. To maintain a consistent and reproducible matrix topography, with minimal changes in porosity, and increasing solely the stiffness of the matrix, D-ribose with collagen enables the increase of the number of collagen crosslinks, non-enzymatically, without altering the matrix density, which is a major factor in cell migration(Mason et al. 2013; Mason and Reinhart-King 2013). Topographical characteristics, therefore, remain constant and enable the isolation of stiffness as the solely affected characteristic of the matrix.

Real-time visualisation of collagen is important when developing methods in biomechanics and tissue engineering. Using collagen's autofluorescence (Glassman, Bryam-Smith, and Garfield 1995) and Second-Harmonic Generation (SHG) (Campagnola et al. 2002) limits the number of exogenous factors influencing the collagen. However, it offers limited contrast and resolution while requiring specialised imaging hardware not readily available to all. Stains used in histology, such as picrosirius red (Junqueira, Bignolas, and Brentani 1979), cannot be used unless on fixed samples, and therefore eliminate the ability for live cell imaging. The fluorescent labelling of collagen allows for much higher contrast and resolution of matrix structures applicable to a greater number of microscopy techniques.

Matrix post-polymerisation fluorescent labelling methods, such as CNA35-EGFP (Aper et al. 2014), are too lengthy for imaging the initial impact the matrix has on cell morphology. Therefore, pre-polymerisation fluorescent labelling offers a greater visualisation of collagen structure across a greater number and more accessible range of fluorescent microscopes, as opposed to other techniques, such as SHG on multi-photon systems. This labelling will be explored through a variety of methods such as CNA35-EGFP, Cy3 mono-reactive dye and Alexa647-SE to determine the best fluorescent labelling of collagen structure. However, these components introduce another exogenous factor, possibly impacting the polymerisation, stiffness, and topography of the matrix.

To verify the integrity of both unlabelled and fluorescently labelled matrices, multiple methods for the measure of elasticity and stiffness of samples can be used. Particle tracking micro-rheology (Hoffman et al. 2006; Liu et al. 2006) uses thermal vibrations of fluorescent particles or markers to calculate their displacement using the fluctuation-dissipation theorem. This method can allow for the measurement of local mechanical properties but involves a further injection of exogenous properties, possibly adding another factor to the matrix. Micropipette aspiration (Hochmuth 2000; Oh et al. 2012) utilises negative pressure when aspirating sections between 1 to 5 μm to measure the deformation, but it cannot measure the homogenous stiffness distribution. To circumvent additional factors influencing the collagen and to measure the uniform stiffness of collagen matrices, AFM quantitative imaging (Hirvonen et al. 2020; Levental et al. 2010; Mahaffy et al. 2004) provided the best method for uniform matrix stiffness measurements by imposing a micro-indentation with a bead of a known size, and the resulting force-indentation curve used to calculate stiffness through predictions of the Hertz model.

When investigating the cytoskeletal structure of cells, one of the main components that allow the cell to rapidly adapt to and influence its surroundings is actin (Sagot et al. 2002). Present in both monomeric ATP-bound globular actin (G-actin) and polymeric filamentous actin (F-actin), regulators of actin allow cells to form a variety of structures, such as filopodia and pseudopodia, to explore, impact and utilise the surrounding ECM. Filopodia and pseudopodia, both rich in actin, are intricately controlled and modified as determined by the specific needs of the cell and dynamically remodelled to overcome specific barriers (Krause and Gautreau 2014). F-actin is therefore a prime candidate for exploring the cytoskeletal organisation of the cell when imaging in 3D matrices.

HeLa cells were infected with the Lifeact-mScarlet lentiviral construct to observe the effects of 3D collagen-ribose matrices of increasing stiffness on single-cell morphology. mScarlet has a quantum yield of 0.7, higher than the quantum yield of other monomeric red fluorescent proteins (mRFP), and an extinction coefficient of

100,300$M^{-1}cm^{-1}$, resulting in the highest brightness of the mRFP spectral class, 3.5-fold higher than that of mCherry (Bindels et al. 2016). Using mScarlet coupled with lifeact will therefore allow for greater stability, reduced laser power, reduced cytotoxicity, and greater performance in imaging of 3D cytoskeleton relative to the ECM.

To decipher the subcellular processes in live samples, advances in microscopy are constantly being pushed to capture the workings of cells with the least amount of influence. An important balance is required to obtain the highest resolution from samples without causing loss of signal, aberrations, and minimal bleaching. To capture the full scale of single cells and the surrounding matrix, 3D microscopy techniques need to be equipped for adequate depth penetration and z-resolution. To meet these criteria at the scale of single cells and the surrounding matrix, the iSIM and LLSM offer the best options for the clear and concise 3D imaging of single cells embedded in collagen.

The iSIM is a system designed for the capture of high-resolution images at high frame rates and real-time display of images making it a very practical method in live cell imaging (Curd et al. 2015; Winter et al. 2014). As opposed to the LLSM, it illuminates the entirety of the sample during imaging, therefore making the risk of bleaching and phototoxicity to the sample greater than the fine Bessel beam illumination provided by the LLSM. However, the iSIM captures a greater volume of the sample, enabling the complete capture of cells and the surrounding collagen structure when imaging. The LLSM ultrathin light sheet illuminates only the field of view and allows for high axial resolution with negligible bleaching (Chen et al. 2014).

3D matrices offer the possibility of a mechanobiological investigation, over a variety of lengths and time scales, from homogenously seeded single cells to heterogenous multicellular organoids *in vitro.* Single-cell studies enable an analysis of cell-ECM relationships and eliminate any cell-to-cell effects. HeLa was the first human cell line established and is a widely used model and standard for studying human cellular biology. It is therefore an ideal cell line to explore the development of new live cell

imaging techniques and cell-ECM dynamics across matrices of increasing stiffnesses in 3D. Refining the cell density allows for enough distance between single cells to not influence each other but most importantly to have single cells within the optimum Z-range of the microscope. The optimum position within the matrix for imaging samples is far enough away from the influence of the coverslip, which has high stiffness that changes cell behaviour, while close enough to minimise scatter and aberrations. These methods in 3D cell seeding establish a protocol to utilise different microscopy techniques with relative ease to better explore the cell-ECM relationship before pursuing any live cell imaging.

3.2 Results

3.2.1 Increasing ribose concentrations increases the stiffness of collagen matrices without affecting their topography or structure

To establish the characteristics of *in vitro* rat tail collagen I matrices and assess the effects of stiffness using non-enzymatic glycation with D-ribose, samples were left to polymerise free of any effect from dyes or fluorescent labelling reagents. With 3 final concentrations of 0-, 50- and 200-mM ribose, the stiffness of the matrices was expected to increase with ribose concentration but maintain a consistent topography, as established by Mason et al. 2013. Stiffness quantifications of the matrices were obtained by using the AFM before post-polymerisation fluorescent labelling for structural visualisation and quantification.

CNA35-EGP, containing domains for collagen adhesion protein, offers a highly specific and accurate method for fluorescently labelling already polymerised collagen, clearly visualising ECM structure (Jong et al. 2014). 3D fluorescent images of matrices were acquired with the iSIM, across 50 μm in Z with 1 μm spacing. Representative MIP images across 50 μm in Z and 152 μm in X, as shown in **Figure 3.1.A,** showed consistent 3D matrix topography across ribose concentrations. Volume fill analysis of the full 3D data set post-polymerisation labelled matrices was performed across 152x109x50 μm volumes of the matrix and confirmed an average of 35% collagen volume fill as demonstrated in graph **Figure 3.1.B.**

AFM stiffness measurements performed on 0-, 50- and 200-mM ribose samples showed an increase in Young's Modulus of the matrix with increasing ribose concentration, represented in graph **Figure 3.1.C.** This confirms the correlation of ribose crosslinking with matrix stiffness in collagen matrices, previously demonstrated by Mason et al., 2013.

All subsequent 3D collagen-ribose matrices were considered correctly polymerised and of the corresponding ribose stiffness if cell-free areas met the approximate 35% volume fill.

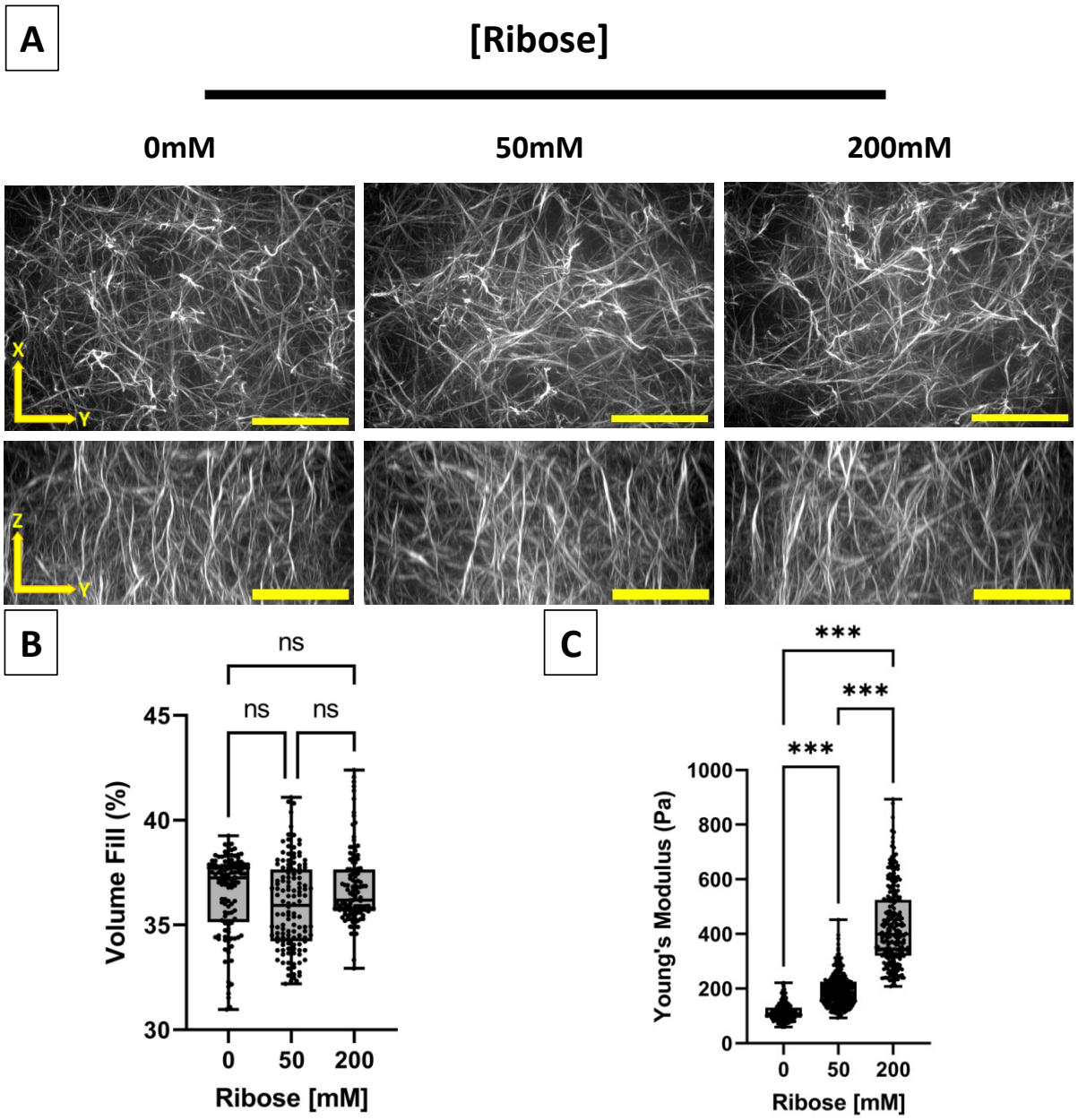

Figure 3.1 – Higher ribose concentrations increase stiffness in collagen type-1 matrices.
A) Representative MIP images through Z and X from iSIM, labelled post-polymerisation with CNA35-EGFP at 0-, 50- and 200-mM ribose. **B)** Graph showing quantification of collagen volume fill across 0-, 50- and 200-mM ribose matrices. **C)** Graph showing stiffness measurements of collagen matrices at 0-, 50- and 200 mM from AFM. Graphs represent at least 120 measurements across five experimental repeats. Scale bars represent 30µm. Error bars represent min to max, box-and-whiskers containing 25th/75th percentile and the median line. Asterisks indicate statistical significance between ribose conditions when tested with Tukey's HSD post-hoc test following significant one-way ANOVA test (***=p<0.001, ns = non-statistically significant).

3.2.2 CNA35-EGFP perturbs the polymerisation process of collagen-ribose matrices

CNA35-EGP, a highly specific collagen binding protein, provided a clear labelling method for polymerised collagen matrices as shown in **Figure 3.1.A**. This seemed the most accurate candidate for labelling pre-polymerised collagen and avoiding unspecific fluorescent binding of samples. Tested as a method for pre-polymerisation labelling to maintain the high specificity for binding to collagen showed a detrimental impact on the polymerisation process of collagen-ribose matrices eliminating all collagen matrix integrity. Imaging of the matrix showed a complete loss of collagen structure, with no visible collagen fibre topography across all ribose conditions, displayed by representative MIP images in **Figure 3.2.A**. Volume fill analysis, **Figure 3.2.B**, had a significantly higher quantity of collagen across all 3 ribose conditions in comparison to corresponding unlabelled control samples from **Figure 3.1**. AFM stiffness measurements showed no variation across ribose conditions between CNA35-EGFP labelled samples as displayed in graph **Figure 3.2.C**, indicating that CNA35-EGFP labelling destroyed stiffness derived from polymerisation and non-enzymatic glycation but causing a uniform stiffness measurement of the collagen concentration instead.

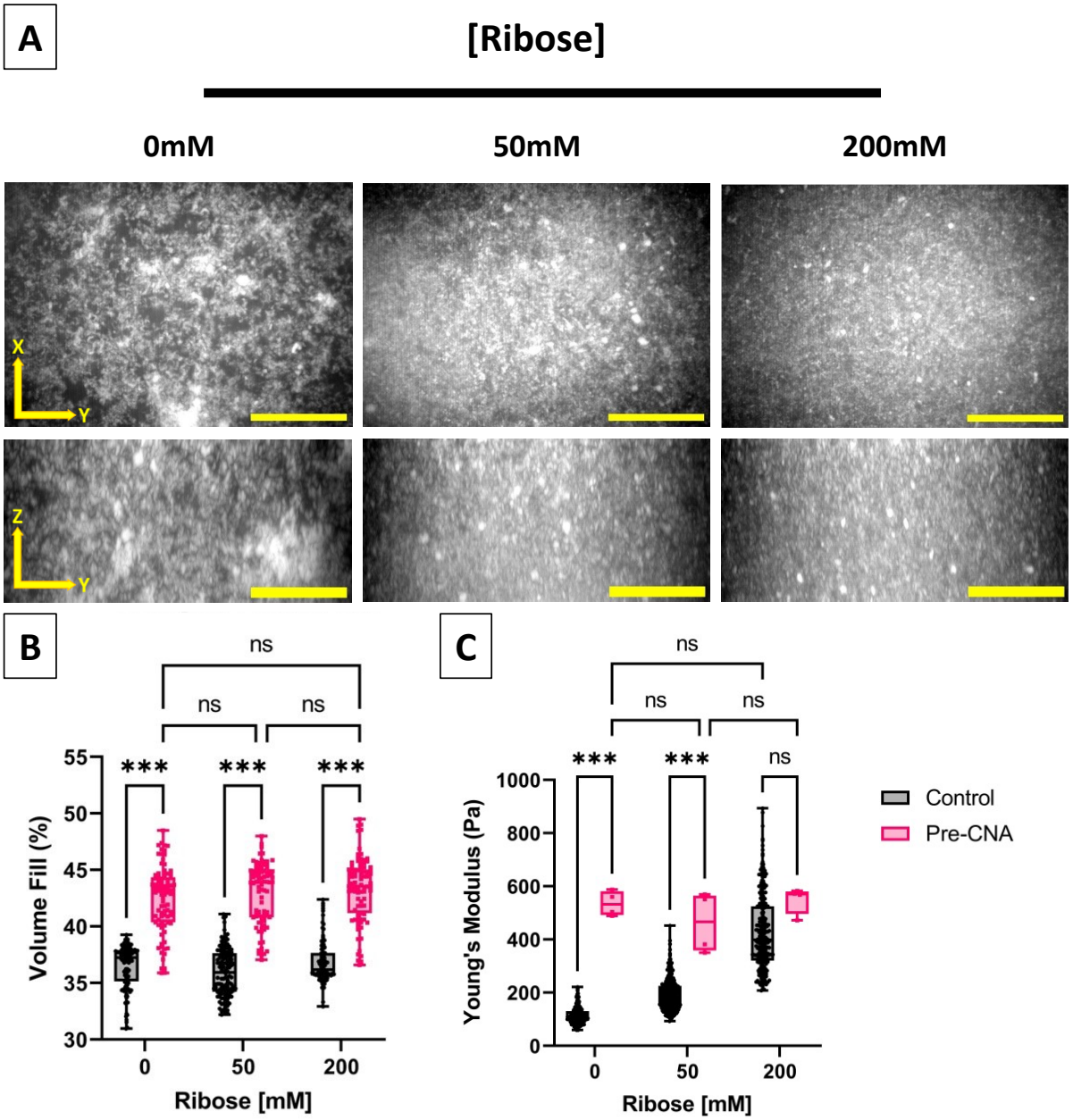

Figure 3.2 – CNA35-EGFP pre-polymerisation causes the complete loss of matrix integrity.
A) Representative MIP images through Z and X from iSIM of CNA35-EGFP labelled collagen matrices at 0-, 50- and 200-mM ribose. **B)** Graph showing quantification of CNA35-EGFP labelled collagen volume fill across 0-, 50- and 200-mM ribose matrices. Graph represents 87 CNA35-EGFP measurements across 3 experimental repeats. **C)** Graph showing stiffness measurements of CNA35-EGFP labelled collagen matrices at 0, 50 and 200 mM with AFM. Graphs represent 3 CNA35-EGFP measurements across 1 experimental repeat. All scale bars represent 30µm. Error bars represent min to max, box-and-whiskers containing 25th/75th percentile and the median line. Asterisks indicate statistical significance between ribose conditions and labelling techniques when tested with Tukey's HSD post-hoc test following significant two-way ANOVA test (***=p<0.001, ns = not statistically significant).

3.2.3 Staining collagen with Cy3 dye influences the topography of collagen-ribose matrices.

Due to the significant impact of CNA35-EGFP on collagen polymerisation sites, resulting in the complete loss of matrix topography and structure, this method was not deemed to be suitable for labelling collagen-ribose matrices pre-polymerisation. Though CNA35-EGFP is successfully used in staining fixed and histology sections for collagen (Aper et al. 2014), we determined that pre-dying collagen with a dye would provide a better and more stable means of visualising native structure as has been previously shown by others (Doyle 2018).

Collagen with Cy3 mono-reactive dye as a technique for fluorescent visualisation of collagen showed no interference with the polymerisation process of collagen-ribose matrices but had a higher level of collagen and fluorescent aggregation, leading to inconsistency in matrix topography. Representative MIP images in **Figure 3.3.A** through Z and X show these aggregations highlighted by magenta circles. This effect was reflected in the volume fill analysis, displayed in **Figure 3.3.B**, showing a significant variation compared to controls in 200 mM ribose condition and between Cy3 samples of 0- to 50- and 200-mM ribose. AFM measurements also showed a significant increase in 200 mM Cy3 ribose stiffness compared to the corresponding unstained control samples and other Cy3 samples as shown in **Figure 3.3.C.**

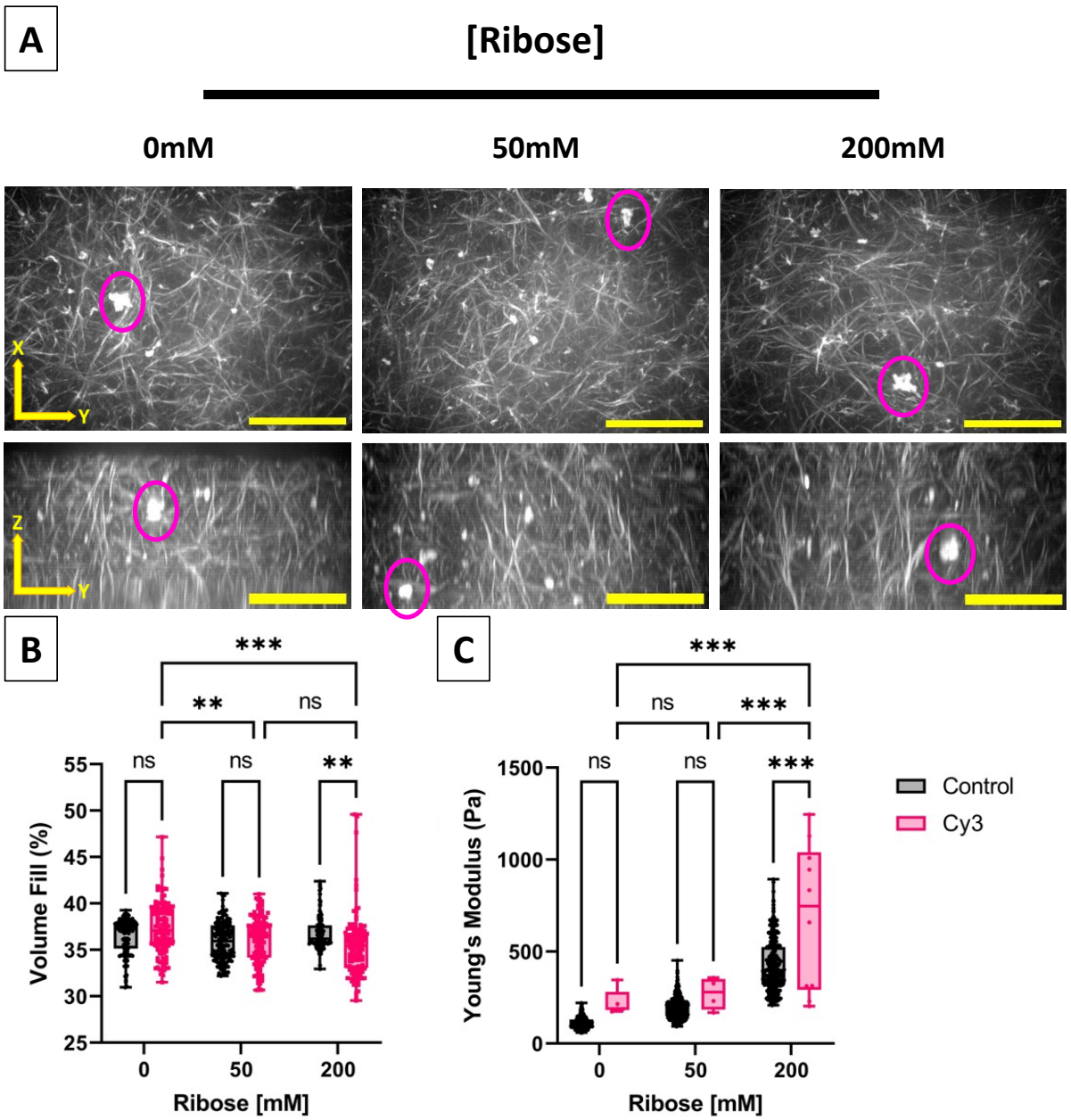

Figure 3.3 – Cy3 mono-reactive dying of collagen shows aberrations in the matrix topography and stiffness.
A) Representative MIP images through Z and X from iSIM of Cy3 mono-reactive dye-stained collagen matrices at 0-, 50- and 200-mM ribose. **B)** Graph showing quantification of Cy3 stained collagen volume fill across 0-, 50- and 200-mM ribose matrices. Graph represents at least 122 Cy3 volume measurements across five experimental repeats. **C)** Graph showing stiffness measurements of Cy3 stained collagen matrices at 0, 50 and 200 mM with AFM. Graph represents 5 Cy3 measurements across 1 experimental repeat. All scale bars represent 30µm. All magenta circles highlight aggregates in the matrix. Error bars represent min to max, box-and-whiskers containing 25^{th}/75^{th} percentile and the median line. Asterisks indicate statistical significance between ribose conditions and labelling techniques when tested with Tukey's HSD post-hoc test following significant two-way ANOVA test (**=p<0.01, ***=p<0.001, ns = not statistically significant).

3.2.4 Alexa647-SE is a viable pre-polymerisation labelling method for collagen-ribose matrices.

The inconsistency in collagen preparations using Cy3 mono-reactive dye, lack of reproducibility in the collagen topography and the long-time scale of its preparation rendered Cy3 an unsuitable and costly method for consistent collagen matrix staining.

To avoid aberrations that might influence cell behaviour, and cause difficulties with fluorescent imaging without influencing the matrix structure and stiffness, further exploring of collagen labelling was needed. Alexa647-SE, being incorporated directly with polymerisation buffer, provided an instant uniform labelling of collagen-ribose matrices at small concentrations (0.4 μg/ mg of collagen) and no labelling of the cell. This method vastly reduced variations in collagen structure and sample preparation time, while residing at a longer wavelength than Cy3, therefore further minimising the phototoxicity of samples for future live cell imaging.

Alexa647-SE matrix showed a structure consistent with that of control samples across 0-, 50- and 200-mM ribose along with no significant difference in volume fill or AFM stiffness measurements (**Figure 3.4.A/B/C**). With consistent and even labelling this approach is a much more reproducible method for collagen labelling. The use of Alexa647-SE for pre-polymerisation collagen labelling was therefore chosen as the approach for all future experiments, with verification of matrix properties via the volume fill criteria and inferred stiffnesses.

Thank you to Ishan Costello and Liisa Hirvonen for their collaboration and help with all the work done on the AFM.

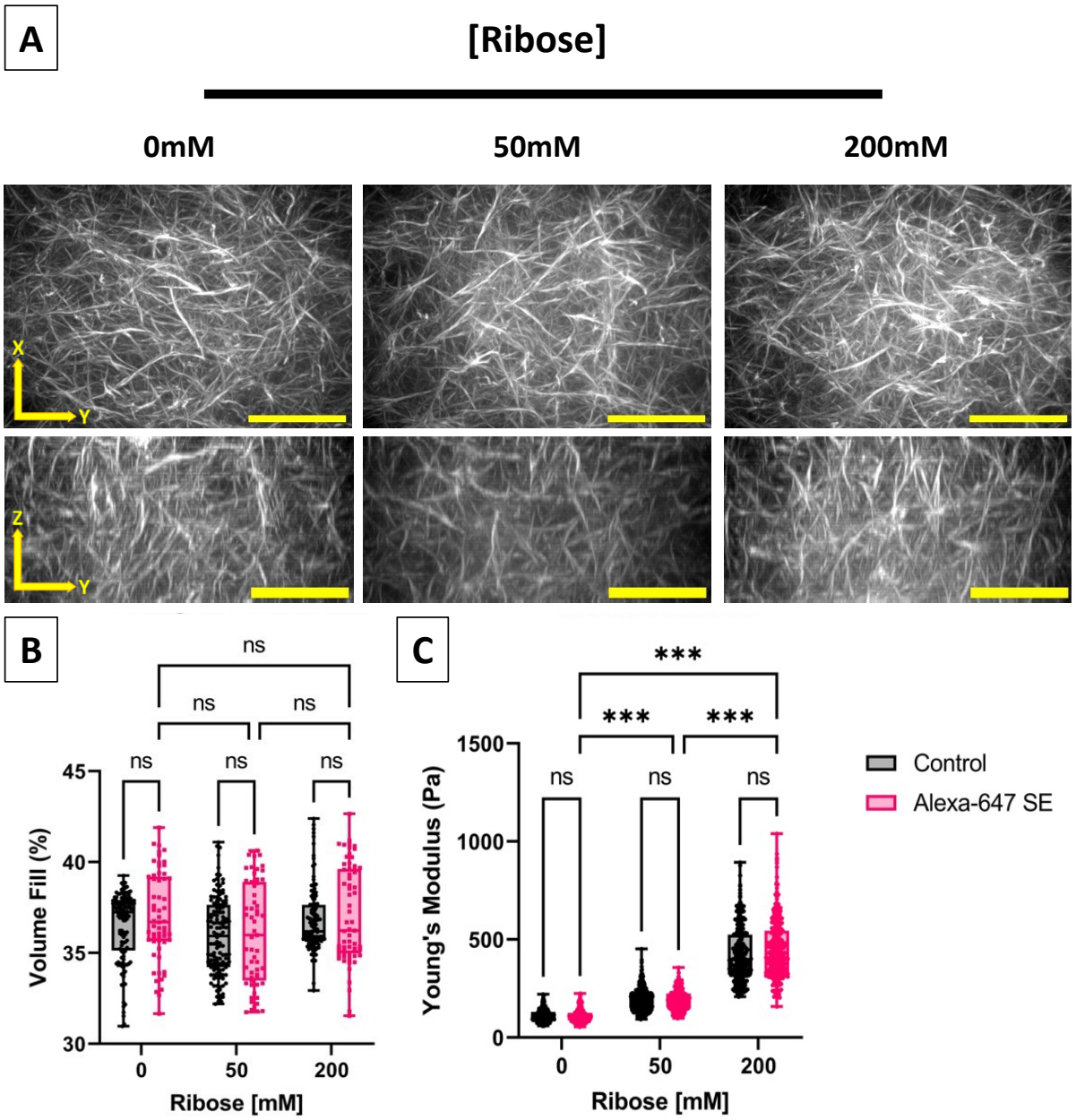

Figure 3.4 – Alexa-647-SE is a viable approach for the pre-polymerisation labelling of collagen-ribose matrices.
A) Representative MIP images through Z and X from iSIM of Alexa647-SE labelled collagen matrices at 0-, 50- and 200-mM ribose. **B)** Graph showing quantification of Alexa647-SE labelled collagen volume fill across 0-, 50- and 200-mM ribose matrices. Graph representing at least 61 Alexa647-SE measurements across 3 experimental repeats. **C)** Graph showing stiffness measurements of Alexa647-SE labelled collagen matrices at 0-, 50- and 200-mM ribose with AFM. Graphs representing at least 230 Alexa647-SE measurements across 5 experimental repeats. All scale bars represent 30µm. Error bars represent min to max, box-and-whiskers containing 25th/75th percentile and the median line. Asterisks indicate statistical significance between ribose conditions and labelling techniques when tested with Tukey's HSD post-hoc test following significant two-way ANOVA test (***=p<0.001, ns = not statistically significant).

3.2.5 Matrix fibrillar features have a consistent degree of organisation when labelled with Alexa647-SE and across ribose concentrations.

Alexa647-SE provided a consistent labelling method of the collagen fibrillar structures with consistent volume fill and stiffness measurements to that of unlabelled samples. To quantify the degree of alignment between neighbouring structures, in control and Alexa647-SE pre-polymerised labelled collagen-ribose matrices, Alignment by Fourier Transform (AFT) was performed on MIP images in Z and subsequently quantified anisotropy through Fourier transformation (Marcotti et al. 2021). AFT is measured on a scale of 1, perfectly aligned, 0, randomly orientated, to -1, being orthogonally aligned with neighbouring structures.

AFT measurements provided a vector field overlay of the original image analysed and a heatmap for vector angle as displayed with representative images in **Figure 3.5**. Collagen-ribose matrices showed a degree of alignment with neighbouring structures due to connecting collagen fibres but not completely uniform in alignment across the entire sample. All 3 ribose conditions, in both post-polymerised CNA35-EGFP, noted unlabelled, and Alexa647-SE pre-polymerised labelled collagen-ribose matrices, showed no statistically significant difference in the order parameter of collagen fibres, as displayed by the graph of **Figure 3.5**. However, when overlaying structures are measured using AFT, the overlayed vector and consequent heatmap display an average of the two, as displayed in the zoomed region in **Figure 3.5**.

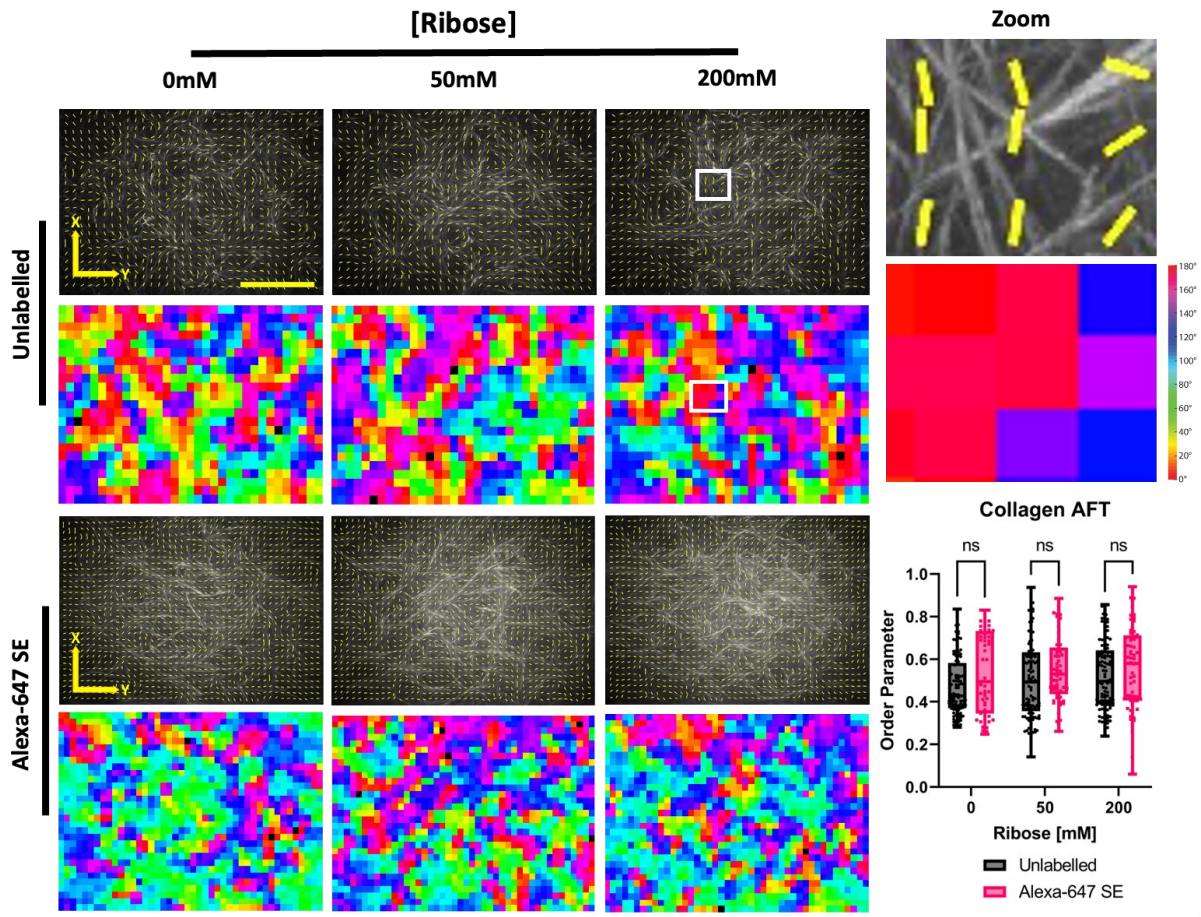

Figure 3.5 – AFT measurements show no effect of ribose or Aleaxa646-SE on the degree of collagen fibre alignment.
Representative MIP images through Z from iSIM overlayed with AFT vectors of CNA35-EGFP post-polymerised labelled (Row 1) and Alexa647-SE pre-polymerised labelled (Row 3) with corresponding angle heatmaps below (Row 2 and 4) across 0- (Column 1), 50- (Column 2) and 200-mM (Column 3) ribose matrices. Zoomed region of interest from the highlighted white box of vector overlay and angle heatmap (Column 4) and a graph showing AFT order parameter of Unlabelled and Alexa647-SE labelled collagen matrices at 0-, 50- and 200-mM ribose. Graph representing at least 90 measurements across 5 experimental repeats. All scale bars represent 30µm. Error bars represent min to max, box-and-whiskers containing 25th/75th percentile and the median line. Asterisks indicate statistical significance via a two-way ANOVA test (ns = not statistically significant).

3.2.6 LLSM offers a greater resolution through Z, but a reduced total volume captured.

There are pros and cons to the use of iSIM vs LLSM for 3D imaging of single cells and the surrounding matrix. With both having a 0.11 μm per pixel resolution in X and Y, the LLSM images through the sample at an angle of 31.5 degrees. Once the raw images were de-skewed and de-convoluted, the resulting image of the LLSM is a parallelepiped and offers twice the resolution through Z. This does however impact the volume it images, capturing less of the surrounding matrix and only the entire volume of smaller cells, as shown with MIP images through Y of both iSIM and LLSM across collagen and actin in **Figure 3.6**. Due to the availability of microscopes and interest in temporal resolutions at different time points, the iSIM was used for imaging cells at 1-hour and the LLSM at 24-hours post-polymerisation.

Thank you to Dylan Herzog and MIC for their help and collaboration on all the work done with the LLSM.

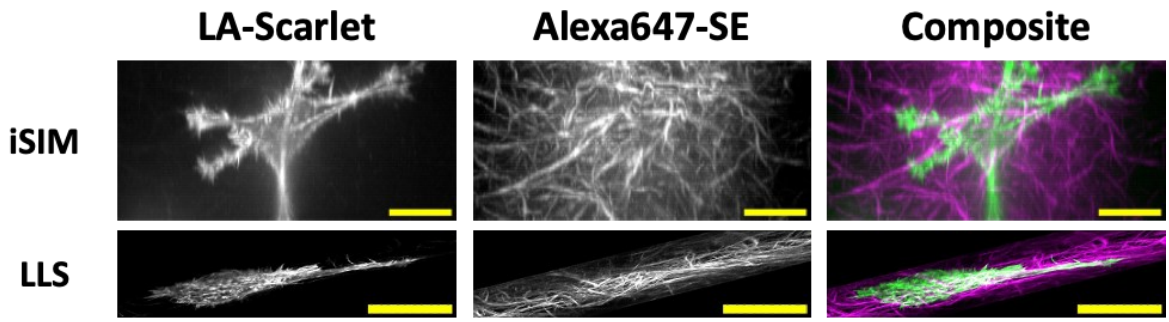

Figure 3.6 – iSIM offers a greater image volume while the LLSM offers a greater resolution in Z.
Representative MIP images in Y acquired on iSIM (Row 1) and LLSM (Row 2) of single HeLa Lifeact-mScarlet cells (Column 1), Alexa647-SE labelled collagen (Column 2), composite (Column 3). All scale bars represent 20 μm.

3.2.7 Collagen matrix stiffness impacts single-cell morphology at 1-hour post polymerisation.

To study the initial impact of collagen matrices of increasing stiffness on single cell morphology, HeLa lifeact-mScarlet cells were used to visualise the fluorescence of the actin cytoskeleton and the surrounding matrix. Moreover, using mScarlet coupled with Alexa647-SE labelled collagen provided a reduced degree of bleaching to samples during imaging. Cells were seeded at a low concentration and suspended uniformly during the collagen polymerization process. Regions of collagen, unperturbed by seeded HeLa lifeact-mScarlet cells, were imaged, and used to validate the matrix topography and stiffness using volume fill analysis as shown in previous figures. If collagen-ribose matrices met the volume fill criteria when images were analysed, then samples were considered validated for further phenotypic characterisation.

To image regions of interest, entire single cells and the surrounding matrix were selected with at least a 15 μm distance from the imaging chamber walls and coverslip. Staying within 150 μm of the coverslip limited aberrations and scattering from the collagen. At 1-hour post-polymerisation, cells are captured early in their adaptation to the surrounding matrix. This early time point, therefore, enables the characterisation of the initial cell morphology as a direct result of contact with the local matrix topography and stiffness.

Single HeLa cells imaged using the iSIM, 1-hour after polymerisation in 0-, 50- and 200-mM collagen-ribose matrices, displayed a range of phenotypes that were specific to the surrounding stiffness. Across all three ribose concentrations, a range of F-actin features was seen that have previously been observed by others in cells in 3D (Mason and Reinhart-King 2013). Representative MIP through 50 μm in Z of lifeact-mScarlet and Alexa647-SE labelled collagen, along with their composites and zoomed region of interest, are shown in **Figure 3.7**.

Single HeLa lifeact-mScarlet cells in 0 mM collagen-ribose matrices assembled fine F-actin structures such as filopodia and lamellipodia. Filopodia are long, thin unbranched actin protrusions that cells use to explore the surrounding environment - highlighted with green arrows in **Figure 3.7**. These play a key role in detecting the surroundings of the cell, relaying information on structure, stiffness, and adhesion sites for the upregulation of protrusion development. Lamellipodia are thin, broad sheet-like protrusions, mediated though Arp2/3 branching, coming off the main body of the cell that show no distinct F-actin fibres but provide a wide surface area for the cell to cover in exploring the surrounding ECM. The representative image of a HeLa cell in 0-mM collagen-ribose matrix shows clear filopodia extending off the lamellipodia and into the surrounding collagen. These remaining-actin structures remained close to the cell body and extended in all directions.

Single HeLa lifeact-mScarlet cells embedded in 50 mM collagen-ribose matrices showed a more defined protrusive phenotype. At 1-hour post polymerisation, HeLa lifeact-mScarlet cells showed no clear polarity but extended pseudopodia, displaying clearly distinct F-actin fibres along the protrusion from off the cell body in a multitude of directions into the surrounding collagen matrix. These F-actin-rich structures, as highlighted in **Figure 3.7** with yellow arrows, also showed some level of alignment with collagen fibres.

In 200 mM ribose collagen gels, HeLa lifeact-mScarlet cells showed a clearly defined protrusive phenotype expanding further out into the matrix and displaying characteristics such as stress fibres and arcs spanning the length of the protrusion and cell body, shown with red arrows in **Figure 3.7**. potentially anchoring focal adhesion sites linking the cell to the ECM, highlighted by the orange arrow in **Figure 3.7** to apply greater levels of force on their surroundings. However, there was still no clear polarity to the cells.

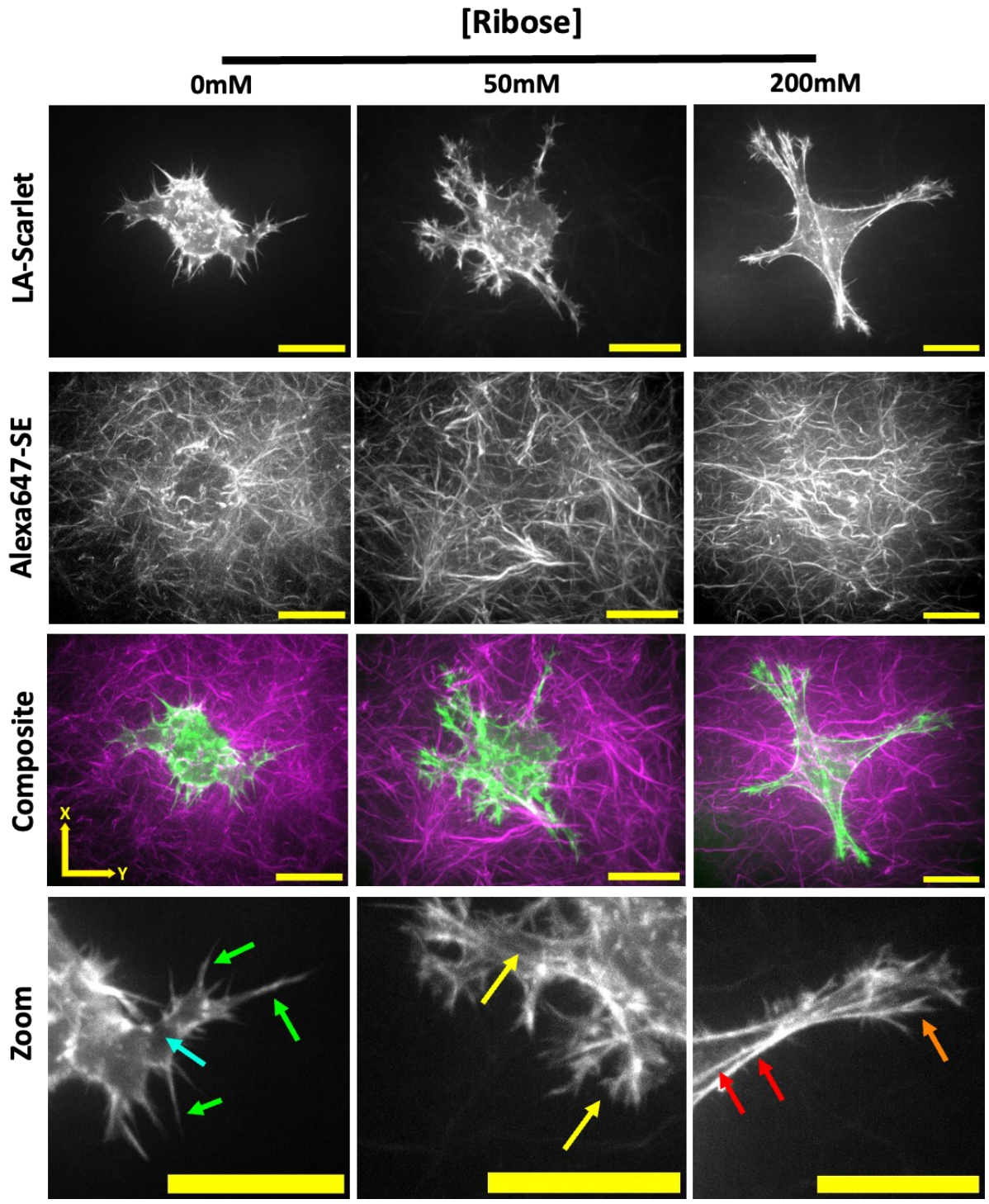

Figure 3.7 – The initial impact of matrix stiffnesses on single cells induces different F-actin structures and phenotypes.
Representative MIP images in Z acquired on iSIM of single HeLa lifeact-mScarlet cells (Row 1), Alexa647-SE labelled collagen (Row 2), composite (Row 3) and zoomed Region of interest (Row 4), across 0-, 50- and 200-mM ribose matrices. Green arrows point to filopodia, blue to lamellipodia, yellow to pseudopodia, red to actin stress fibres and orange to possible focal adhesion sites. All scale bars represent 20 μm.

3.2.8 Single cells lose their initial morphology after 24-hours in 3D collagen-ribose matrices.

As opposed to 1-hour post-cell seeding, 24-hours enables the cell to adapt to the ECM and start to impose its influence on the surrounding structures. Using the same protocol, single cells were embedded in collagen-ribose matrices of increasing stiffness and imaged using the LLSM at 24-hours post-polymerisation to visualise the morphological changes of the cell. Cells across 0-, 50- and 200 mM collagen-ribose matrices showed fewer but more defined actin structures and levels of polarity. Representative MIP through Z of Lifeact-mScarlet and Alexa647-SE labelled collagen, along with their composites and zoomed region of interest are shown in **Figure 3.8.**

HeLa Lifeact-mScarlet cells in 0 mM collagen-ribose matrix at 24-hours still have filopodia present however have replaced lamellipodia for actin-rich and defined pseudopodium, highlighted with a yellow arrow in **Figure 3.8**. In 3D single-cell migration this is known as the leading edge being the main traction force generator for cell motility. With filopodia stretching along the pseudopodium length and end, green arrows in **Figure 3.8**, imply a continued exploration of the matrix ahead of the cell migration for information relaying. This leading-edge observes higher alignment with that of collagen fibres, but it is not clear without live cell imaging if the cell has aligned itself to the collagen or has imposed traction force and realigned the collagen towards it.

50 mM collagen-ribose single cells, **Figure 3.8**, displayed a clear leading edge with pseudopodia, highlighted by a yellow arrow, protruding from the cell body with a defined polarity. Other structures such as lamellipodia and filopodia, as highlighted by blue and green arrows, were also visible in these samples.

Cells embedded in 200 mM collagen-ribose matrices again showed a distinct polarity and the presence of clearly defined pseudopodia and stress fibres, highlighted in

Figure 3.8. Notably, collagen fibres were orientated along the length of the pseudopodia. This indicates a great amount of traction force being generated on the surrounding matrix by the cell.

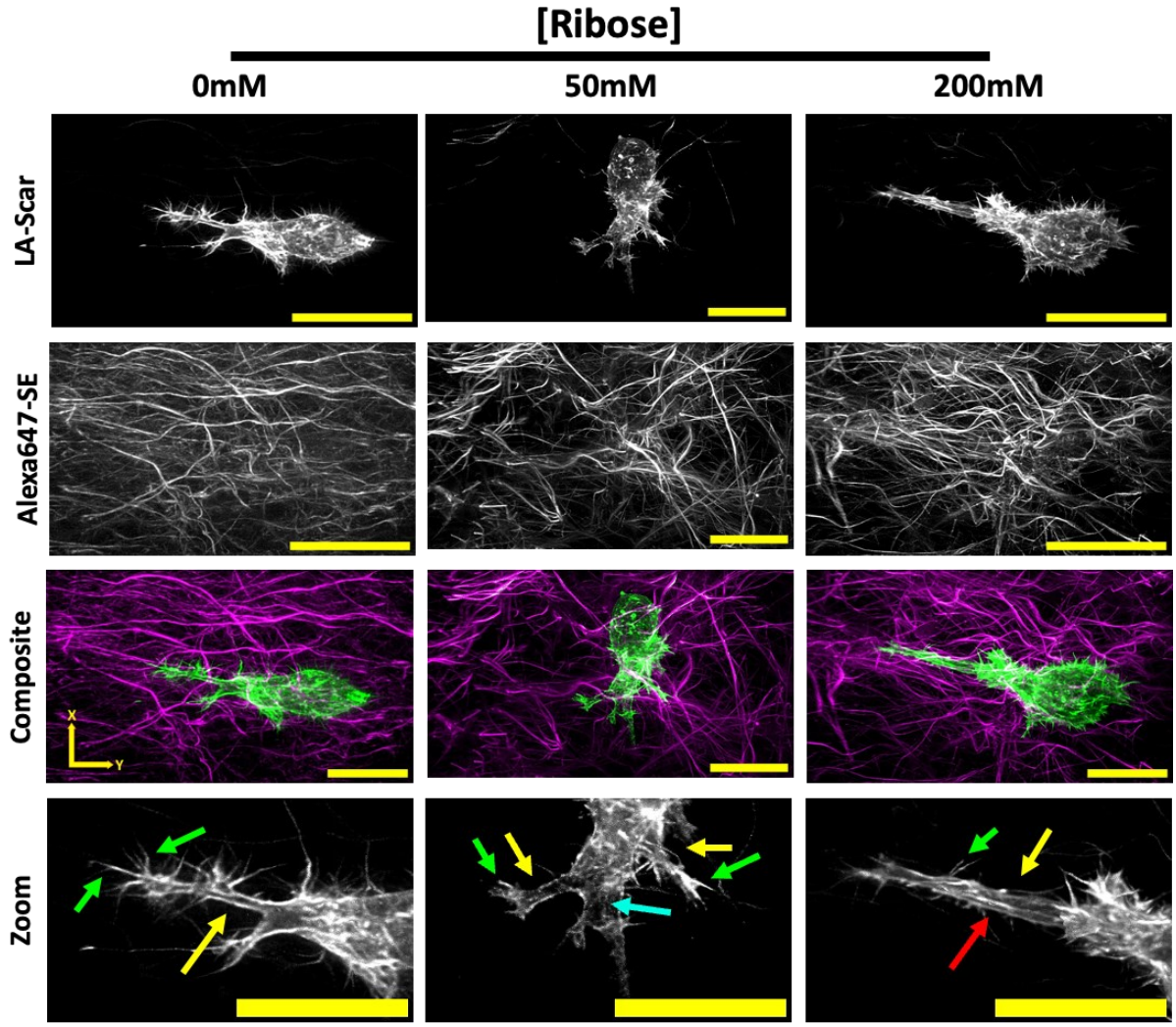

Figure 3.8 – Single cells adapt their morphology to better navigate the surrounding matrix, despite differences in stiffness.
Representative MIP images in Z acquired on LLSM of single HeLa lifeact-mScarlet cells (Row 1), Alexa647-SE labelled collagen (Row 2), composite (Row 3) and zoomed Region of interest (Row 4), across 0-, 50- and 200-mM ribose matrices. Green arrows point to filopodia, blue to lamellipodia, yellow to pseudopodia and red to actin stress fibres. All scale bars represent 20 μm.

3.2.9 Single cells show an increase in surface area to volume ratio with increasing stiffness at 24-hours.

When looking at 3D objects an important factor in understanding their morphology is the comparative surface area to the volume it has. The surface area is the external layer of the object, and the volume refers to the total amount of space within the object. In the case of single cells, as seen in **Figures 3.7 and 3.8**, their shape is intrinsically linked to their physiology, the plasma membrane being that of the surface area and the volume being everything contained within. To better understand if the phenotype observed in single cells translated into changes in volume and surface area, 3D measurements of HeLa lifeact-mScarlet embedded in 0-, 50- and 200 mM collagen-ribose matrices at 1- and 24-hours were performed.

Cells within 0 mM collagen-ribose matrix 1-hour post-polymerisation showed a significantly lower surface area to volume ratio compared to 50- and 200 mM matrices as demonstrated in **Figure 3.9**. No statistically significant changes to the surface area to volume ratio were seen at 24-hours between matrices of increasing stiffness, indicating this initial low surface area to volume ratio is lost upon cell adaptation to the ECM conditions.

It is important to note that due to the limited volume captured by the LLSM as compared to the iSIM, and the mesenchymal migratory phenotype adapted by single cells at 24-hours, smaller cells were imaged in their entirety, as displayed in the Volume graph at 24-hours in **Figure 3.9**.

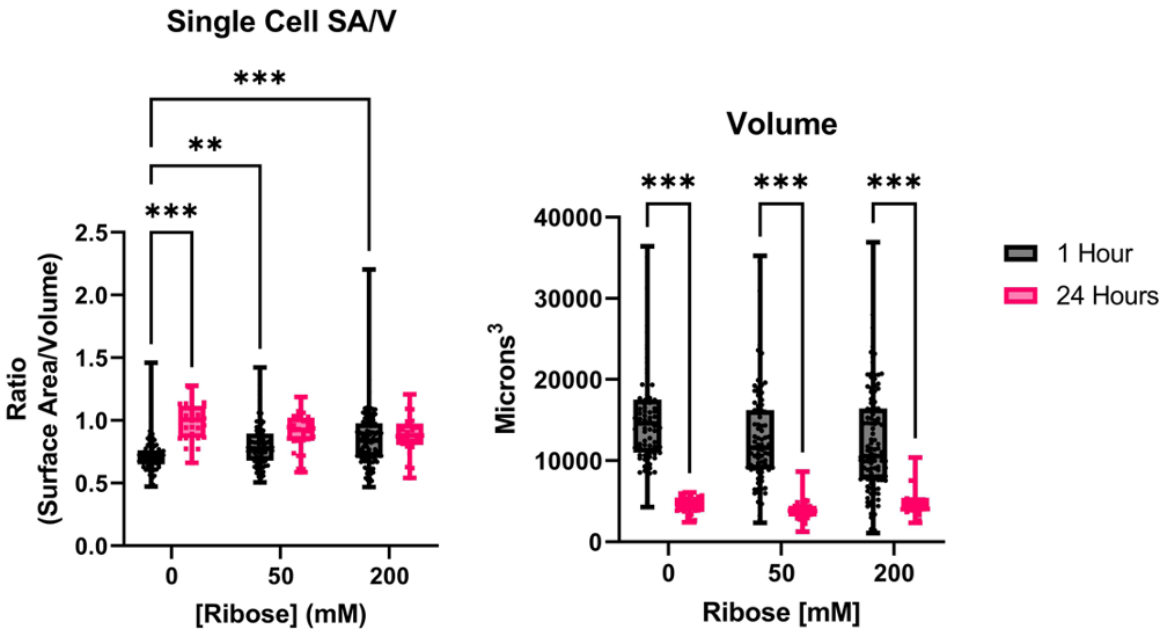

Figure 3.9 - Single cells show an increase in surface area to volume ratio with increasing stiffness at 1-hour.
Graphs showing surface area to volume ratio and volume measurements of HeLa lifeact-mScarlet cells across 0-, 50- and 200-mM collagen-ribose matrices. Graphs representing at least 70 measurements across 5 experimental repeats. Error bars represent min to max, box-and-whiskers containing 25th/75th percentile and the median line. Asterisks indicate statistical significance between ribose conditions and time points when tested with Tukey's HSD post-hoc test following significant two-way ANOVA test (**=p<0.01, ***=p<0.001).

3.2.10 Collagen-ribose matrices show a higher degree of alignment after 24-hours of single-cell seeding across all ribose conditions.

To ascertain the impact of single cells on the surrounding matrices' degree of alignment after 24-hours, AFT measurements were performed on MIP images in Z of collagen fibres surrounding cells at 1- and 24-hours. Samples from 1-hour were imaged on the iSIM and 24-hours on the LLSM across matrices 0-, 50- and 200-mM ribose. AFT measurements provided a vector field overlay of the original image analysed and a heatmap for vector angle as displayed with representative images in **Figure 3.10**.

Collagen-ribose matrices showed a significantly higher degree of alignment with neighbouring structures at 24-hours than that of 1-hour across all 3 collagen-ribose matrices and at 24-hours no statistically significant difference was seen in the degree of alignment across ribose conditions, as displayed by the graph of **Figure 3.10**.

Though not displayed, no significant difference in the order parameter was seen between matrices without embedded cells and matrices embedded with cells imaged at 1-hour. There was also no significant difference in the order parameter between control and cell-free regions of collagen matrices at 24-hours across all 3 ribose conditions.

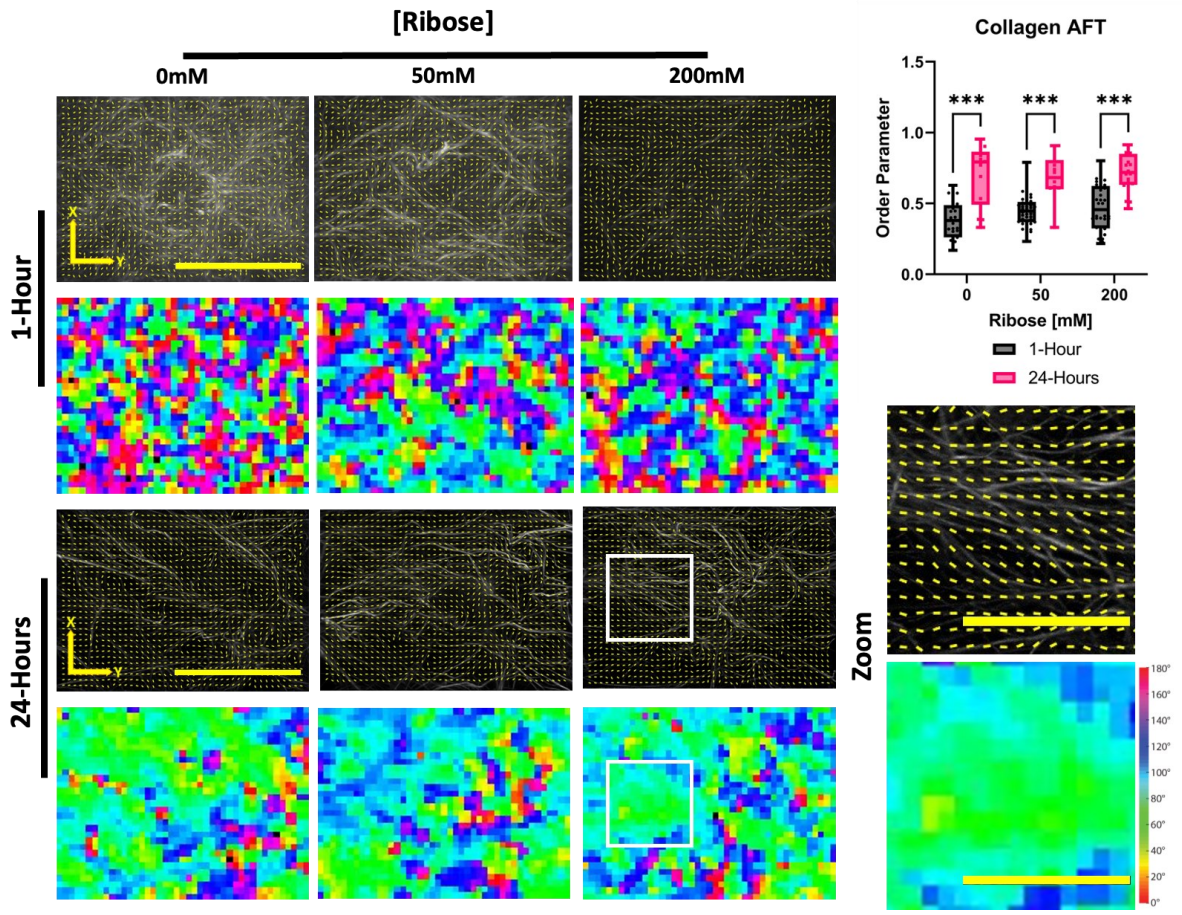

Figure 3.10 - AFT measurements show higher levels of collagen fibre alignment after 24-hours across all ribose conditions.
Representative MIP images through Z overlayed with AFT vectors Alexa647-SE pre-polymerised labelled matrices from iSIM at 1-hour (Row 1) and LLSM at 24-hours (Row 3) with corresponding angle heatmaps below (Row 2 and 4) across 0- (Column 1), 50- (Column 2) and 200-mM (Column 3) ribose matrices. Zoomed region of interest from the highlighted white box of vector overlay and angle heatmap (Column 4) and a graph showing AFT order parameter of 1- and 24-hour collagen matrices at 0-, 50- and 200-mM ribose. Graph representing at least 32 measurements across 4 experimental repeats for 1-hour samples and 17 measurements across 3 experimental repeats for 24-hour samples. All scale bars represent 15 μm except Zoom regions with a scale bar of 10 μm. Error bars represent min to max, box-and-whiskers containing 25th/75th percentile and the median line. Asterisks indicate statistical significance between time points when tested with Tukey's HSD post-hoc test following significant two-way ANOVA test (***=p<0.001).

3.3 Discussion

3.3.1 Isolating stiffness as the only changing variable while visualising collagen structure and organisation

The data in this chapter demonstrates a reproducible method of increasing *in vitro* matrix stiffness through the non-enzymatic cross-linking of collagen with ribose. Though using ribose crosslinking as the only method for increasing matrix stiffness, it displays consistent results in collagen fibre structure organisation, porosity and increasing stiffness relative to ribose concentration. However, previous authors (Mason and Reinhart-King 2013) noted a possible influence of receptors for advanced glycation end products (RAGE) in increased angiogenesis and controlled for this with the use of anti-RAGE blocking antibodies. In this thesis, no steps were taken to control for the impact RAGE might have on single-cell morphology. In future research using this method of sugar-inducing crosslinking in collagen, controlling for RAGE on samples would be carried out.

The use of AFM indentations to collect force curves on the sample of interest allows for the estimation of young's modulus by fitting linear elastic contact mechanical models, such as the Hertz model. It has been noted that measuring soft biological samples might be affected by the stiffness of the rigid surfaces on which it is placed (Stylianou et al. 2019). To circumvent this influence, measurements of collagen-ribose matrices were performed at least 300 μm above the coverslip.

When measuring collagen samples of such low stiffness, further problems arise when extracting stiffness measurements from force curves. Though the bead used is large enough to apply force across a network of collagen, as opposed to an individual fibre, initial attempts at fitting the whole curve showed no discernible difference in matrix stiffness. This is thought to be due to the partially unpolymerized and viscous surface against which the AFM touches down (Elosegui-Artola et al. 2022). Indentation curves also showed consistent multiple drawbacks during the indentation phase due to the force of the AFM breaking past viscoelastic layers in the collagen. We therefore only used the final 10% of the indentation curve to extract estimated Young's modulus measurements of overall matrix stiffness to eliminate the

impact of initial surface contact and disruptions caused by these viscoelastic barriers breaking. This showed measurements, away from these interferences, to have a higher stiffness of the matrix when increasing ribose concentration. Measurements of individual collagen fibres in the matrix would enable a more representative measure of the properties felt directly by the cell interactions in the matrix.

AFM stiffness measurements for samples containing embedded single cells are not practical as there is no way to visualise where the AFM touches down and selectively choose local regions to measure. This makes it impossible to determine if the measurements are of the matrix or cell itself and offer no useful information.

The ECM has been shown to have a high degree of alignment in different tissues and pathologies, such as cancer (Ouellette et al. 2021) and fibrosis (Park et al. 2020). This is thought to play a critical role in the mechanical properties of the ECM, with reduced flexibility and increased stiffness compared to unaltered ‘basket weave’ ECM (Mascharak et al. 2021). Though AFT analysis allows the efficient quantification of anisotropy of the collagen fibres relative to neighbouring structures it is important to note that AFT measurements are limited to MIP and cannot resolve overlaying structures any other way than by averaging them. However, coupled with 3D volume fill analysis, shows the consistency of structural topography in collagen fibre organisation. Therefore, 3D volume fill analysis is done on all consecutive experiments in regions unaffected by cells to verify the correct polymerisation of collagen-ribose matrices and consequently validate their stiffness.

This technique allows for a reproducible and consistent method for truly isolating out stiffness as the sole changing variable in 3D matrices that is more physiologically relevant whilst avoiding limitations such as increasing collagen density, consequently affecting matrix structure and pore size. This enables a standard against which to verify any future manipulation of the matrix through 3D volume fill analysis, AFT and AFM measurements to maintain similar, but not identical, topography and porosity throughout the matrix whilst increasing stiffness.

3.3.2 Fluorescently labelling collagen-ribose matrices allows for better resolution and greater flexibility for imaging.

The use of unstained collagen in 3D matrix cell culturing has been successfully visualised with techniques such as SHG coupled with multi-photon microscopy (Streets et al. 2014) or confocal reflectance (Yang and Kaufman 2009). This allows the matrix to remain unchanged by further external factors. This however has the disadvantage of requiring specialised microscopy techniques not necessarily available to everyone, a reduced signal-to-noise-ratio compared to fluorescent techniques and is tied to the limitations of those microscopes in future live cell imaging (Campagnola et al. 2002; J. H. Lee et al. 2016).

The ability to visualise collagen fluorescently opens the door to utilising a greater number of fluorescent microscopes. Post-polymerised labelling with CNA35-EGP allows for very specific labelling of the collagen but requires hours of incubation and a multitude of washes to obtain a clear signal, therefore, being too time-consuming for early imaging of single cells (**Figure 3.1**). Pre-labelling techniques for the clear visualisation of the matrix at early time points cause another factor to possibly influence the polymerisation process, as seen with CNA35-EGFP. This complete loss of structure is most likely due to the size and location of CNA35-EGFP and its binding site on the collagen. CNA35-EGFP is therefore better utilised on fixed 3D matrices for collagen visualisation but not pre-polymerisation labelling (**Figure 3.2**).

Cy3 initially stains unpolymerized collagen before incubating with ribose and can be prepared for consistent labelling of the matrix in a batch-dependent manner. However, due to the lengthy time scale preparation of the initial Cy3-collagen mix, this leaves it more susceptible to being exposed to changes in heat, pH, shock, and contamination. This has been shown to affect the integrity of the matrix, such as in **Figure 3.3**, where collagen and fluorescent aggregation occurred. Though Cy3 does not interfere with the polymerisation of collagen-ribose matrices, these aggregates could play a role in the local stiffness and impact single-cell behaviour. Coupled with the long time-scale preparation and lack of reproducibility this is not the most efficient method for visualising the matrix.

In using Alexa647-SE, we eliminate the time spent exposing it to elements that could affect the collagen and incorporate it directly with the polymerisation buffer. It requires a very small concentration for good labelling and plays no interfering role in the structure or stiffness of the matrix as displayed by AFM, AFT and volume fill analysis (**Figure 3.4 & 3.5**). Alexa647-SE has the added advantage of further minimising phototoxicity under fluorescent imaging due to it residing at a further length scale on the emission spectrum than GFP or RFPs. This will be an essential factor for cell survival in future chapters when undergoing live cell imaging in 3D.

3.3.3 LLSM offers greater resolution and speed of acquisition over a smaller sample volume

Fluorescent imaging of cells in 3D is highly phototoxic due to the increased laser power required to image at depth and repetitive scanning of samples through Z. Using Alexa647-SE, residing in a minimal phototoxic wavelength, combined with the use of Hela lifeact-mScarlet cells at a higher quantum yield, pre-emptively reduce the phototoxic impact on live samples for future experiments. An important balance of factors for cell survival, such as the correct selection of microscope for obtaining the correct scale, best resolution, appropriate speed acquisition, sufficient depth penetration and laser power for minimal phototoxicity is vital for 3D sample image acquisition. The iSIM offers the same resolution as the LLSM in X and Y but has a slower acquisition time in Z and requires the successive imaging of colour channels. To compensate for this, reduced exposure time and greater Z distance are applied to accelerate image acquisition impacting not only the Z-resolution but the signal-to-noise ratio. Minimising the amount of laser power also reduces the bleaching of the sample, as the design of the iSIM causes the entire sample to be illuminated during imaging.

Due to the Bessel Beam design of the LLSM, only the focal plane is illuminated nearly eliminating the bleaching of the sample and allowing for rapid sequential colour channel imaging in 3D. The LLSM captures images through Z at an angle and once deconvoluted and deskewed offers 2.3 times the resolution in Z as opposed to the iSIM. However, the LLSM images over a reduced volume therefore only capturing small cells in their entirety or partial sections of larger ones. These are important factors that will need to be considered when proceeding with future experiments in live cell imaging and the degree of dynamics looking to be captured.

3.3.4 Single-cell morphology and its relationship to ECM stiffness evolve with time.

The imaging of single cells and surrounding collagen-ribose matrix at 1- and 24-hours provides useful indications of single-cell behaviour and cytoskeletal structure regarding surrounding matrices of increasing stiffness. It has been previously reported an increase in cell spreading on stiffer substrates when culturing cells in 2D is a significant predictor of cellular traction (Califano and Reinhart-King 2010). Translated into 3D, similar results of increased spreading of cells are seen in matrices of increasing stiffness (Mason et al. 2013). We have not investigated cell-specific relationships to the ECM in this thesis but should be further investigated using the established method developed here.

We observed a significant degree of surface area to volume ratio increase with that of increasing 3D collagen-ribose matrix stiffness almost immediately, as shown by single-cell images captured 1-hour post polymerisation (**Figure 3.7**). Due to the time scale of the polymerisation process and the required washes to remove unbound Alexa647-SE, 1-hour was the earliest time point possible to start imaging single cells in collagen-ribose matrices. Low stiffness matrices showed cells with a less stable cytoskeletal phenotype when adapting to their new environment, displaying lamellipodia and filopodia as the most prominent features. These are designed for exploring and sensing the local surrounding ECM, crucial in single cell adaptation and migration, in search of supportive structures to exert traction forces on. With no clear polarity or direction and coupled with the fine actin phenotype, this would indicate that low stiffness matrices offer an insufficiently stable environment to support HeLa cells in developing greater cytoskeletal structures at 1-hour post-polymerisation.

With increasing stiffnesses of the surrounding collagen-ribose matrices, more defined cytoskeletal structures extend further into the surrounding matrix at higher stiffnesses. Cells imaged showed a more developed actin phenotype, with pseudopodia rich in filamentous actin and greater levels of organisation, extending further from the cell body into the matrix. With still no clear polarity to the cell, it

however shows a more stable surrounding matrix upon which to adhere and upregulate protrusion activity at early time points. At the highest degree of matrix stiffness, 200 mM collagen-ribose, the surrounding fibres indicate having structural support stable enough for stress fibres and focal adhesions to form at the same period. 200 mM collagen-ribose matrices display a clear actin-rich phenotype expanding out from the cell body into the surrounding structure strongly adhering and developing actin stress fibres.

At 24 hours cells share a similar phenotype despite changes in stiffness, with highly directional actin-rich pseudopodium coming off the cell body far into the surrounding matrix. In lower stiffness matrices especially, the cells have lost fine actin structures, such as lamellipodia, for a more defined actin-rich phenotype (**Figure 3.8**). It is important to note at this stage that due to the reduced total volume captured by the LLSM, cells imaged in their entirety are of a reduced volume, as shown in **Figure 3.9**, and therefore more likely to acquire a migratory phenotype with the ability to manoeuvre through collagen pores of this size. It can also be noted the leading edge of these cells display a higher level of collagen fibre alignment. Future 3D imaging of single HeLa lifeact-mScarlet cells and their surroundings with the LLSM will include cells of a greater volume, to avoid this bias. However, due to the limitations of the LLSM, only regions of interest will be imaged.

AFT measurements at 24-hours showed a high degree of matrix re-organisation by the cells, with a much higher order parameter of alignment of the collagen structure across all three ribose conditions (**Figure 3.10**). This indicates that however stiff the surrounding matrix, single cells can impose a significant degree of re-organisation that is missing from cell-free regions of the same sample. Though HeLa cells are not known to have a highly migratory phenotype compared to other cell lines, it is not possible to know for sure of previous cell activity in that region. From this, we can only conclude, though unsure of the possible influence of cells despite heterogeneous cell activity, that the cell activity impacts the local environment directly in the vicinity and a series of further experiments on cell-free areas would be required to evaluate the impact of matrix re-organisation at known distances from the

cell. Due to time constraints, long-term imaging over time of cell-free regions was not performed but would be interesting to explore in future experiments.

With reduced filopodia and a reduced number of pseudopodia at 24-hours, cells have adapted more defined actin-rich cytoskeletal structures to navigate the surrounding matrix. Early time points, therefore, indicate a heavy initial influence of the surrounding matrix structure and stiffness on the cytoskeletal organisation of single cells adapting to their surroundings. At 24-hours results from the change in single cell morphology and re-organisation of the local collagen matrix indicate the cell can influence its surroundings even with matrices of increased stiffness.

The imaging of single cells and collagen at 1- and 24-hours provides useful indications of cell behaviour and cytoskeletal structure regarding surrounding matrices of increasing stiffness however, live cell imaging will allow for a better understanding and dissection of the cell-ECM relationship. To further investigate the dynamics of single-cell activity across different stiffnesses and on the surrounding collagen structures, live 3D imaging of these cells and collagen-ribose matrices at 1- and 24-hours will help determine the cause and effect between the two over time, as explored in greater depth in chapter 4.

4 Mesoscale characterisation of the impact of ECM stiffness on embedded single cells.

4.1 Introduction

Cells physiologically occupy a three-dimensional space within the ECM, and influence both the matrix organisation and neighbouring cells in a complex and dynamic manner. Through mechano-coupling (mechanical force transduction) and biochemical coupling (translated into biochemical signals), specific cellular responses are activated in response to the surrounding matrix properties and structure. Using this series of signalling pathways, directly linked to the cytoskeleton, or deriving from integrin signalling pathways, single cells can rapidly alter and adapt their morphology through changes in protein-protein interactions, conformation, activation, or gene expression. The tight regulation of F-actin cytoskeletal structures, and the distortions these structures impose on the cell membrane, enable cells to better explore, adhere and facilitate cell migration. Cytoskeletal protrusive structures discussed in the previous chapter, such as filopodia, lamellipodia and pseudopodia, rely on dynamic behaviour to effectively function (van Helvert, Storm, and Friedl 2017; Pedersen and Swartz 2005). Imaging these protrusions in 3D over time will offer a greater insight into the complex relationship ECM stiffness has on single-cell behaviour.

Developments and advances in microscopy have transformed how 3D cellular mechanisms are investigated in cell biology. These constantly evolving techniques and models have enabled the study of cell morphology, gene expression and ECM deposition and organisation to be visualised and imaged in real-time. Observing these dynamic changes offers insight into the molecular workings and behaviour of cells but is not without its challenges. Some techniques that offer improvements in spatial resolution either lead to much slower imaging or a much higher photon dose, which leads to photobleaching and phototoxicity (Tinevez et al. 2012).

Fluorescent imaging of live cells in 3D requires fast image acquisition, high-depth penetration and a non-destructive intensity of excitation whilst maintaining cellular temperature, pH, and CO_2 levels. This balance must be obtained at the appropriate temporal resolution (TR) for the desired dynamics to be captured whilst avoiding light scattering within deep samples. The iSIM, being a widefield technique, allows for the

recording of large fields of view, working with any form of fluorophore and requiring low excitation power to capture multiple colour channels in 3D at a depth of over 100 μm. The iSIM illuminates the entire sample during imaging, increasing the rate of bleaching as opposed to the Bessel beam illumination method of the LLSM (Curd et al. 2015; Fiolka et al. 2012; Winter et al. 2014; Zhovmer and Combs 2021). The LLSM offers the benefits of low levels of photobleaching and phototoxicity coupled with very fast multiple colour image acquisition in 3D, offering the highest TR in 3D to better capture physiological processes (Chen et al. 2014).

Photobleaching is the irreversible quenching of fluorescence in a sample that occurs due to the reaction between the excited fluorophore and oxygen, producing possibly toxic levels of reactive oxygen species (Stephens and Allan 2003). Increased excitation and exposure time causes accelerated bleaching of the sample and rate of deterioration (E. Wang, Babbey, and Dunn 2005). This is further amplified when imaging in 3D, across multiple colour channels and over time. It is therefore vital to minimise bleaching by adjusting the laser power, exposure time, Z-resolution, and TR to limit cell cytotoxicity and loss of signal to noise due to photobleaching (Conchello and Lichtman 2005). Though many methods have been developed to process images for noise reduction, ultimately imaging at the highest signal-to-noise ratio offers the best opportunity to localise structures and follow the dynamics of cell functions (Lanza et al. 2014; Luisier et al. 2010).

When imaging cells in 3D materials, such as collagen-ribose matrices, interfering structures, increased aberrations and scattering with depth also lead to reduced imaging quality (Hell et al. 1993; Wilson and Jacques 1990). Though many advances in microscopes have increased the quality of images at greater depth within a sample it is still one of the limiting factors of many microscopes in 3D imaging (Egner, Schrader, and Hell 1998). Many techniques, often due to hardware and optics, obtain higher resolution but at the cost of acquisition speed. The higher the acquisition speed the better the dynamics that can be captured and therefore analysed and quantified. 3D imaging across multiple colour channels and large distances in Z greatly amplifies the acquisition time, even further limiting the TR.

This chapter aims to use the single HeLa lifeact-mScarlet cell model established in the previous chapter to analyse cytoskeletal dynamics in response to changing 3D ECM stiffness. This information is important to ascertain the interplay between the surrounding ECM and the formation of highly dynamic and heterogeneous protrusions. As the LLSM became available later in the project, early time points were imaged over a longer period and at lower TR with the iSIM to reduce phototoxicity and capture more of the surrounding matrix for early dynamics. The LLSM offered higher TR of reduced phototoxicity for the imaging of cells, allowing the capture of dynamics in established cells and already remodelled collagen at 24 hours, as seen from initial images and AFT analysis in the previous chapter.

4.2 Results

4.2.1 ECM stiffness induces different morphological characteristics and dynamics after initial seeding

To further explore our initial findings, HeLa lifeact-mScarlet cells and the surrounding collagen dynamics were imaged using 3D time-lapse microscopy. Initial imaging was performed on single cells 1-hour post-embedded in 0-, 50- and 200-mM collagen-ribose matrices at a TR of 10 minutes over 2 hours. The combined use of lifeact-mScarlet and Alexa647-SE collagen enabled the consecutive imaging of both colour channels with the iSIM, taking approximately one minute per channel. These imaging parameters showed no detrimental effects on cell health and allowed the capturing of the dynamic features of single cells and the surrounding matrix during the initial stages of adaptation to the surrounding matrix.

Single cells imaged at 1-hour in low stiffness 0-mM collagen-ribose matrices showed rapid protrusion and retraction of filopodia, highlighted by green arrows, and lamellipodia, highlighted by blue arrows. Filopodia and lamellipodia in 0-mM collagen-ribose matrices remained close to the cell body without extending far into the surrounding matrix. Cells showed no specific protrusion directionality or remodelling to the surrounding matrix causing little to no displacement of collagen fibres. Similar types of cytoskeletal structures were visualised throughout the imaging period, favouring faster turnover across a greater variety of axes, as is highlighted by representative MIP images in **Figure 4.1.A** and **Supplementary Video 4.1.A**.

Cells captured in 50-mM collagen-ribose matrices at 1-hour post-embedding, exhibited more lamellipodia, highlighted by blue arrows, elongating further into the surrounding matrix and with a reduced speed of turnover as compared to cells in 0-mM ribose. Lamellipodia spread over a large surface area with some apparent directionality, indicating the presence of the leading edge and showed a reduced number and length of filopodia around the cell body compared to cells in 0-mM ribose. Defined pseudopodia, highlighted by yellow arrows, had a smaller surface area but F-actin structures that showed greater co-alignment with collagen fibres

than those seen at 0-mM ribose. This co-alignment of protrusions with collagen fibres appeared to result in displacement of the ECM during these dynamic changes in cell morphology, as is represented in **Figure 4.1.B** and **Supplementary Video 4.1.B**.

HeLa lifeact-mScarlet cells embedded in 200-mM collagen-ribose matrices showed numerous clearly defined pseudopodia, highlighted by yellow arrows, expanding into the surrounding matrix immediately at 1-hour post-embedding. Initial pseudopodia showed no clear directional bias, but a number consolidated into long actin-rich protrusions that appeared to contact the collagen fibres at the tips. The dynamic behaviour of these protrusions was coincident with visible deformation and displacement of proximal collagen fibres during the 2-hour imaging period. Dynamic pseudopodia that did not associate with collagen fibres retracted back to the cell body, whereas protrusions with visible ECM association tended to become stabilised as shown in the MIP images in **Figure 4.1.C** and **Supplementary Video 4.1.C**.

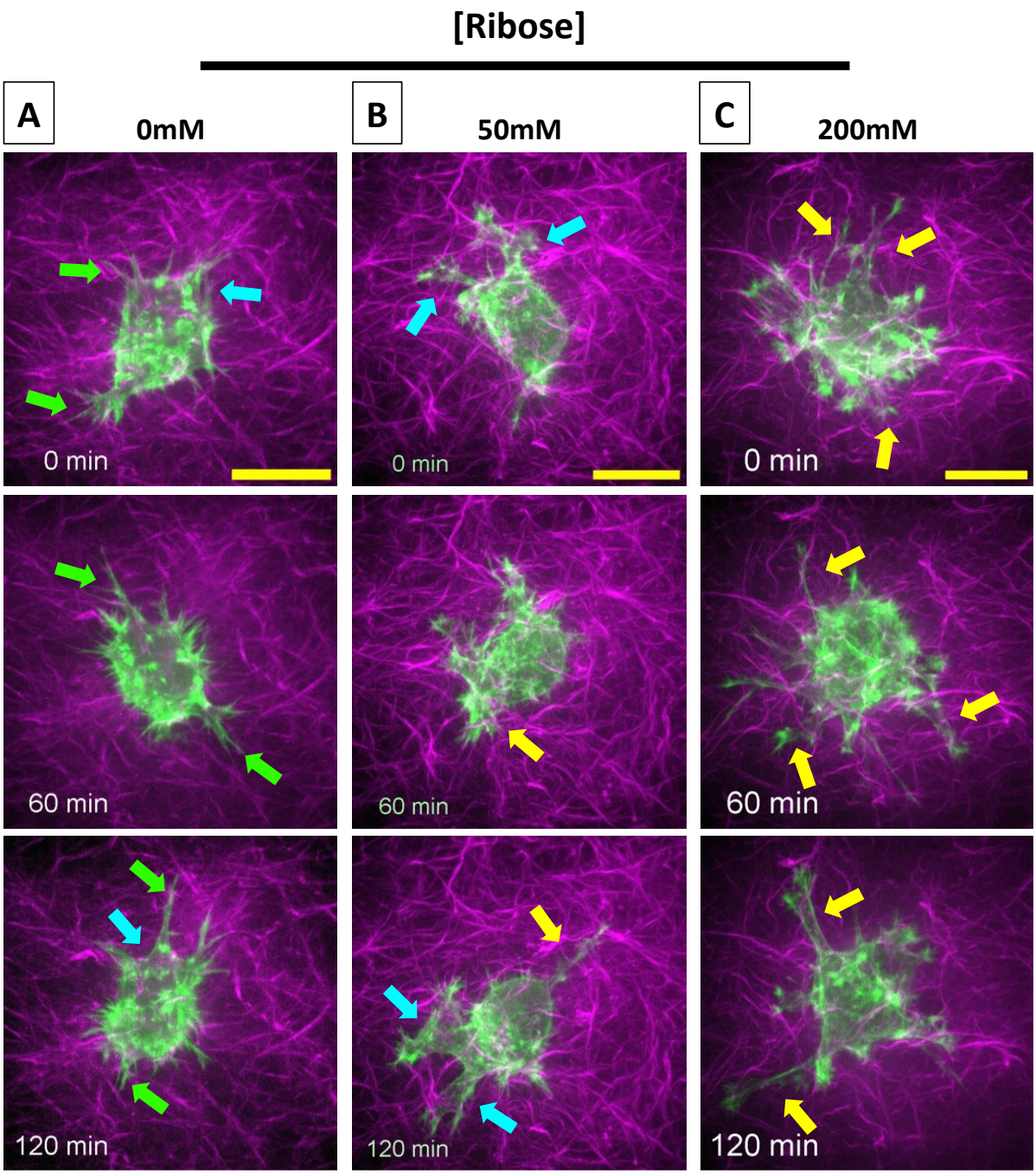

Figure 4.1 – Higher stiffness matrices induce greater and more defined protrusive cytoskeletal structures.
A) Representative MIP images in Z acquired on iSIM of single HeLa lifeact-mScarlet cells (Green) embedded in collagen (Magenta) at TR of 10 min 0-mM collagen-ribose matrix, **B)** 50-mM collagen-ribose matrix and **C)** 200-mM collagen-ribose matrix. Green arrows point to filopodia, blue to lamellipodia and yellow to pseudopodia. All scale bars represent 20 μm.

4.2.2 Single cells display a more uniform morphology across stiffnesses at 24-hours to better navigate the surrounding ECM.

Following on from the initial findings in Chapter 3 of single cells at 24-hours embedded in 0-, 50- and 200-mM collagen-ribose, the dynamics at different stiffnesses were imaged using LLSM. A TR of 30 seconds for the imaging of both colour channels sequentially was achieved for 30 minutes before deconvolution and deskewing achieved a final Z-resolution of 0.2 μm. This TR enabled the capturing of the finer dynamics of single-cell activity and remodelling of the surrounding collagen matrix at increasing stiffnesses.

Due to the reduced volume imaged with the LLSM, the cells acquired were of a smaller volume and displayed a migratory phenotype more adapted for mobilising through pores. Cells displayed a unidirectional migratory phenotype across all collagen-ribose matrices, aligning to varying degrees with the matrix. Cells embedded in 0-, 50- and 200-mM collagen-ribose matrices showed similar F-actin-rich leading protrusions, with defined F-actin fibres, highlighted by yellow arrows and retractive end of the cell highlighted by red arrows. 15-minute MIP images in Z of the HeLa lifeact-mScarlet and Alexa647-SE labelled collagen are displayed in **Figure 4.2.A/B/C** and the full 30-second TR available in **Supplementary Video 4.2.A/B/C**. This data showed, despite more developed actin structures in matrices of higher stiffnesses at 1-hour, single cells of a smaller volume adapt similar migratory morphologies at 24-hours regardless of higher stiffness matrices.

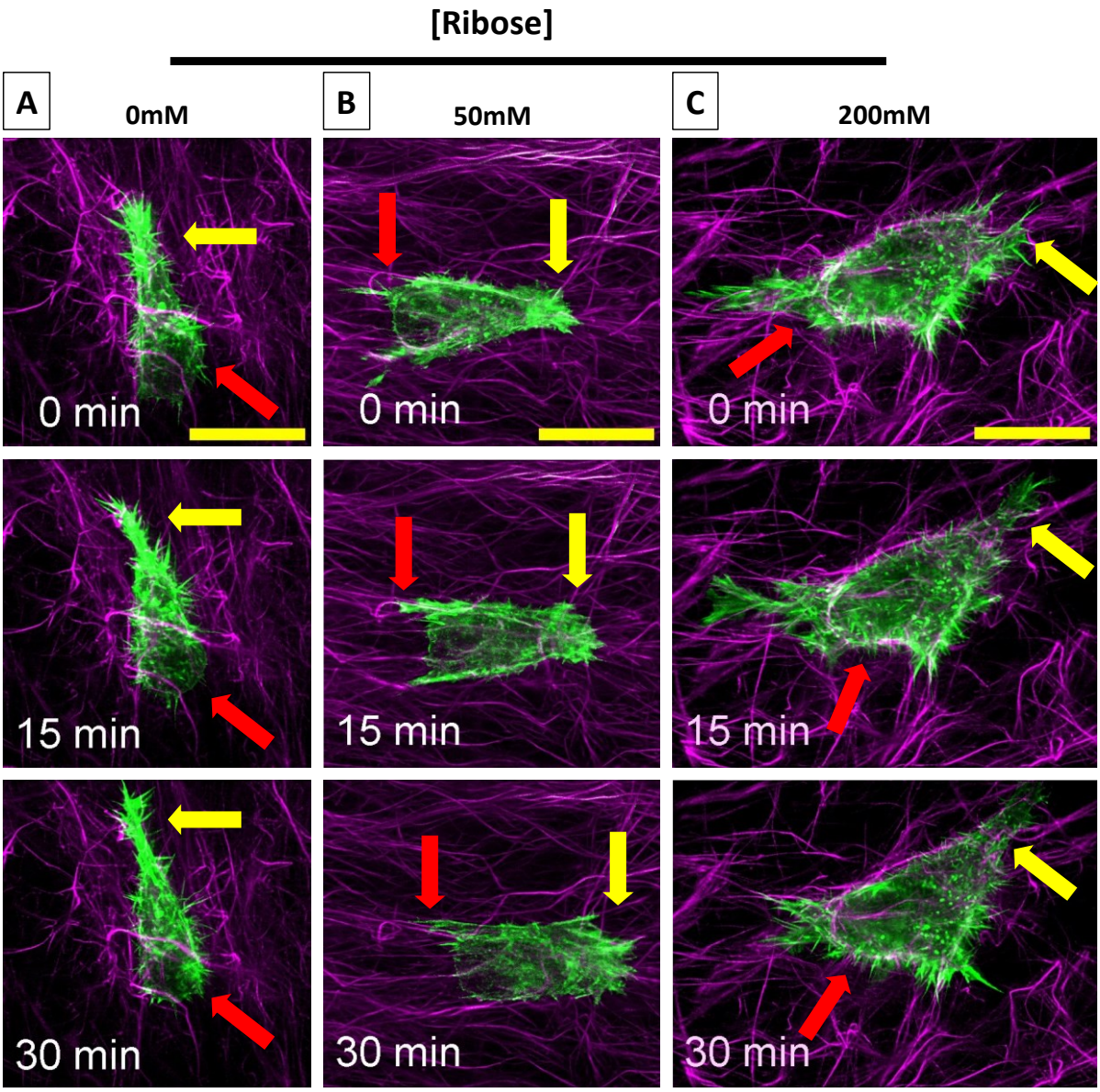

Figure 4.2 – Single cells embedded for 24-hours adapt similar morphologies despite increased stiffnesses of matrices.
Representative MIP images in Z acquired on LLSM of single HeLa lifeact-mScarlet cells (Green) embedded in collagen (Magenta) at TR of 5 min. **A)** 0-mM collagen-ribose matrix. **B)** 50-mM collagen-ribose matrix. **C)** 200-mM collagen-ribose matrix. Yellow arrows point to leading edge and red to retracting cell body. All scale bars represent 20 μm.

4.2.3 Significant bleaching of both cells and collagen occurs when imaging over time in 3D with the iSIM and LLSM.

The rate of sample bleaching relative to the first time point can cause difficulties when attempting to analyse samples. It is important to determine the long-term effect of delivering light onto a live specimen via different techniques, such as widefield illumination of the iSIM versus light sheet illumination of the LLSM, when imaging in 3D at varying TRs.

Images acquired on the iSIM over 1000 by 1400 pixels, with 51 Z-slices, across 2 colour channels and over 13 time-points resulted in a total of 1,326 planes with constant illumination of the whole sample during acquisition. The 3D imaging parameters and TR of 10 minutes for 2 hours, showed significant bleaching of Alexa-647-SE labelled collagen between the first and last time points**.** The rate of bleaching of lifeact-mScarlet was less severe between the first and last time points most likely due to the recovery of new fluorescently labelled actin occurring between imaging series (Tinevez et al. 2012), as displayed and quantified in **Figure 4.3.A/C**.

Samples imaged using LLSM showed a significant degree of bleaching relative to the first time point and of an equal level in both channels. Images acquired on the LLSM over 512 by 512 pixels, with 200 Z-slices, across 2 colour channels and over 61 time-points equalled a total of 24,400 planes, illuminated solely by the light sheet across the sample. Despite the HeLa lifeact-mScarlet cells' ability to recover when imaged under these parameters and TR, this resulted in the same rate of bleaching as the Alexa647-SE labelled collagen (with no significance being seen at the same time points between channels), as is displayed and quantified in **Figure 4.3.B/D.**

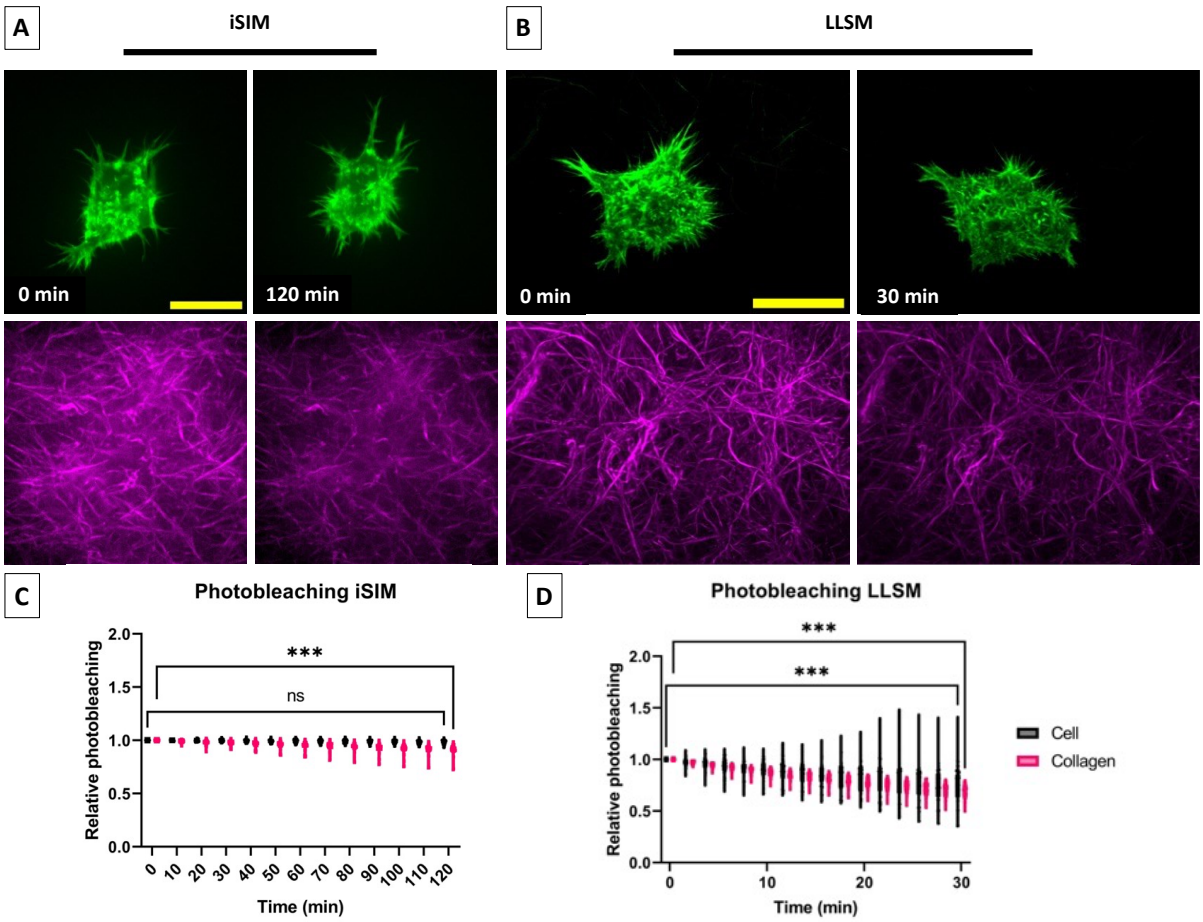

Figure 4.3 – Collagen bleaching is significant when imaging over time, but cell bleaching becomes more significant at higher TR.
A) Representative MIP images of single HeLa lifeact-mScarlet cells (Green) embedded in collagen (Magenta) in Z, acquired on iSIM of 0 and 120 minutes at a TR of 10 minutes and **B)** LLSM at 0 and 30 minutes at a TR of 30 seconds. **C)** Quantification of the rate of bleaching from cell and collagen fluorescence over 120 minutes at 10-minute TR relative to the first time point on iSIM. Graph representing 63 measurements across 5 experimental repeats. **D)** Quantification of the rate of bleaching from cell and collagen fluorescence over 30 minutes at 30-second TR relative to the first time point on LLSM. Graph representing 58 measurements across 5 experimental repeats. All scale bars represent 20 μm. Error bars represent min to max, box-and-whiskers containing 25th/75th percentile and the median line. Asterisks indicate statistical significance between ribose conditions and labelling techniques when tested with Sidaks multiple comparison post-hoc test following significant two-way ANOVA test (ns = not statistically significant, ***=p<0.001).

4.2.4 Cells embedded in 50-mM collagen-ribose at 1-hour show a higher mobilisation within the matrix compared to other stiffnesses.

These single cells imaged at 1- and 24-hours post-embedding show morphological turnover and displacement within the matrix. At 1-hour post embedding in collagen-ribose matrices of 0-, 50- and 200-mM, single cells showed restructuring of the cytoskeleton and protrusions, as represented by temporally coloured edges of single cell imaged with the iSIM at 10-minute intervals over 2-hour period in **Figure 4.4.A.** Cells imaged on the LLSM at 30-second TR over 30 minutes showed a consistent morphology over time, as represented by MIP temporally coloured edges of 5 min intervals in **Figure 4.4.B.**

Centroid tracking enabled the magnitude of morphological changes over time by the single cell to be quantified. The measured magnitude of centroid shifts between time points, across X, Y and Z dimensions, showed no significant difference between ribose conditions in either 1- and 24-hour post-embedding samples. However, a significantly higher degree of centroid shift in cells embedded in 50-mM collagen-ribose matrices for 1-hour was seen compared to 0-mM or 200-mM ribose conditions, as is represented in **Figure 4.4.C**.

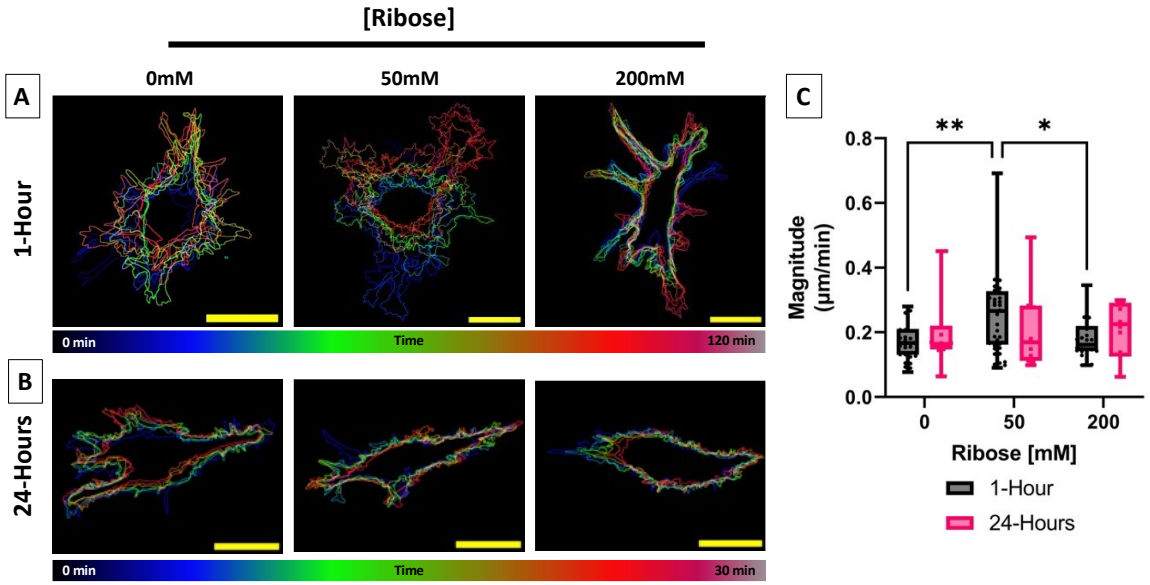

Figure 4.4 - Cells embedded in 50-mM collagen-ribose for 1-hour show a higher ability to mobilise within the matrix.
A) Representative MIP images of single HeLa lifeact-mScarlet cell edges temporally colour coded from raw cells acquired on iSIM across 0-, 50- and 200-mM collagen-ribose matrices of 0 and 120 minutes at a TR of 10 minutes and **B)** LLSM at 0 and 30 minutes at a TR of 5 minutes. **C)** Quantification of centroid magnitude shift over time in X, Y and Z at 1- and 24-hours across 0-, 50- and 200-mM collagen-ribose matrices. Graph representing at least 18 measurements across 3 experimental repeats. All scale bars represent 20 μm. Error bars represent min to max, box-and-whiskers containing 25th/75th percentile and the median line. Asterisks indicate statistical significance between ribose conditions when tested with Tukey's HSD post-hoc test following significant two-way ANOVA test (*=p<0.05, **=p<0.01).

4.2.5 Actin dynamics, 1-hour post-embedding, show increased degrees of retraction across all ribose conditions.

Cell motility and the corresponding changes in morphology are required for single cells to navigate and remodel the surrounding matrix topography through the extension and retraction of structures such as lamellipodia and pseudopodia. These can be indicators of disease progression, such as invasive tumour cells and ECM remodelling that drive metastasis (Sahai and Marshall 2003). ADAPT, a plugin for the analysis of cellular morphodynamics (Barry et al. 2015), enabled the measurement of cell membrane protrusion, retraction, and velocity in 2D on MIP images through Z time-lapse series. Analysis of single cells at 1-hour post-embedding across matrices of 0-, 50- and 200-mM collagen-ribose with 10-minute TR displayed clear regions of cell membrane protrusion, highlighted by green arrows, and retraction, highlighted by red arrows in **Figure 4.5.A/B/C**.

Cellular morphodynamics analysis showed a higher percentage of the cell membrane retracting in all three ribose conditions compared to protruding, implying higher tractional forces towards the cell centre on the surrounding ECM. These dynamic actin movements along the cell membrane occurred at an equal speed to each other and across stiffnesses, as represented by edge velocity maps for 0-, 50- and 200-mM collagen-ribose samples in **Figure 4.5.A/B/C** and quantified by percentage and speed in graphs of **Figure 4.5.D/E.** Full 10-minute TR over 2 hours of ADAPT edge velocity maps available in **Supplementary Video 4.5.A/B/C**.

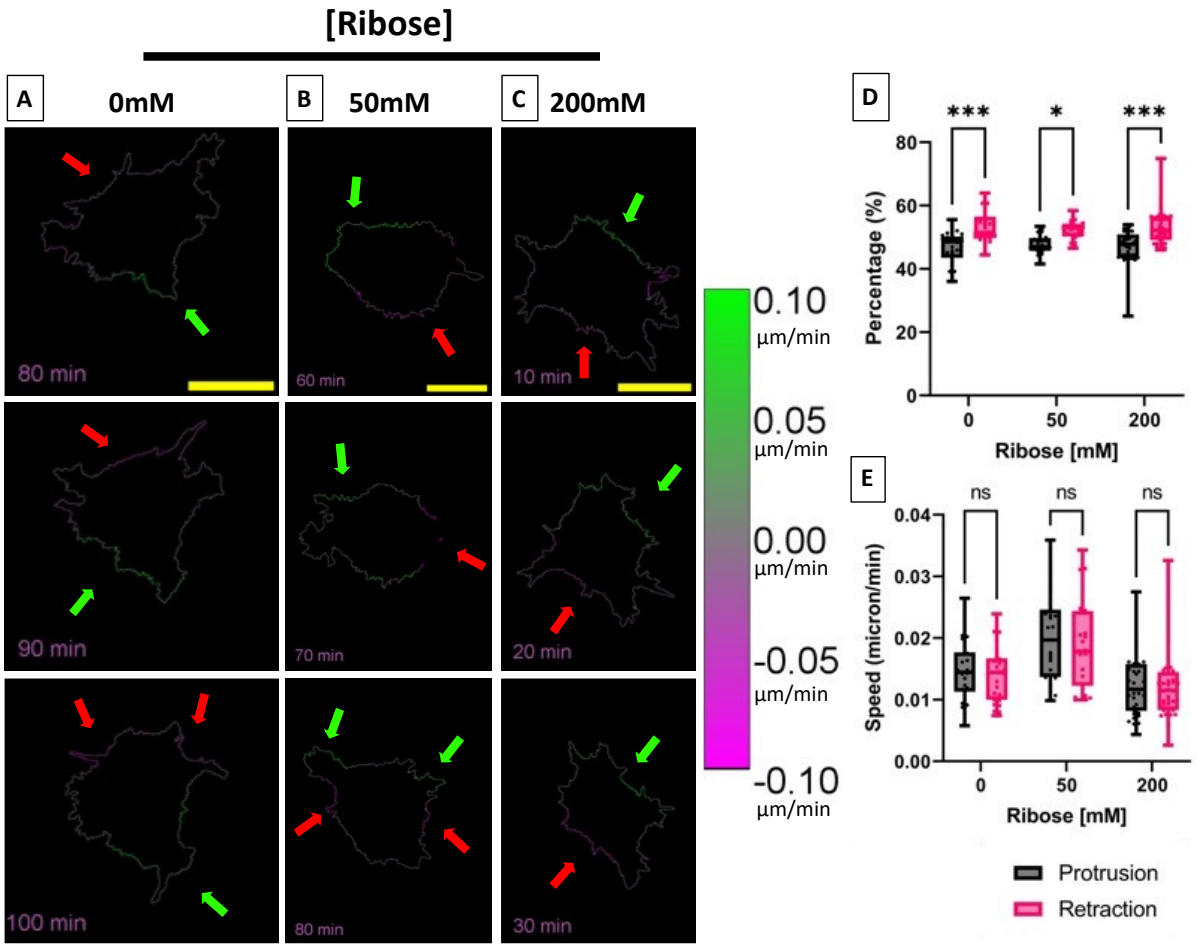

Figure 4.5 – Single-cell analysis of membrane dynamics 1-hour post-embedding show an increased degree of retraction across all ribose conditions.
A) Representative MIP images of single HeLa lifeact-mScarlet cell 1-hour post-embedding edges coloured for protrusion (green) and retraction (red) speed acquired on iSIM across 0-, **B)** 50- and **C)** 200-mM collagen-ribose matrices at a TR of 10-minutes over 2-hour period. **D)** Quantification of cell membrane protrusion and retraction as a percentage and **E)** velocity. Graph representing at least 31 measurements across 3 experimental repeats. Green arrows point to cell membrane extension and red retraction. All scale bars represent 20 µm. Error bars represent min to max, box-and-whiskers containing 25th/75th percentile and the median line. Asterisks indicate statistical significance between protrusion and retraction of ribose conditions when tested with Tukey's HSD post-hoc test following significant two-way ANOVA test (ns = not statistically significant, *=p<0.05, ***=p<0.001).

4.2.6 Actin dynamics, 24-hours post-embedding, show increased degrees of retraction in 0- and 50-mM ribose conditions.

Actin dynamics along the membrane of single cells at 24-hours post-embedding analysed using ADAPT across matrices of 0-, 50- and 200-mM collagen-ribose with 30-seconds TR displayed clear regions of extending protrusion, highlighted by green arrows, and retracting protrusions, highlighted by red arrows in **Figure 4.6**.

Cellular morphodynamics analysis again showed a higher percentage of the cell membrane retracting compared to protruding in cells in 0- and 50-mM collagen-ribose gels, but not 200-mM. These membrane dynamics occurred at an equal speed to each other and across stiffnesses, as represented by edge velocity maps for 0-, 50- and 200-mM collagen-ribose samples in **Figure 4.6.A/B/C** and as quantified by percentage and speed in graphs of **Figure 4.6.D/E.** Full 30-second TR over 30 minutes of ADAPT edge velocity maps are available in **Supplementary Video 4.6.A/B/C**. The results seen from ADAPT analysis showed consistent speeds of cell membrane protrusion and retraction but had an increased percentage of membrane protrusion in 50-mM at 1-hour and 200-mM at 24-hours post embedding.

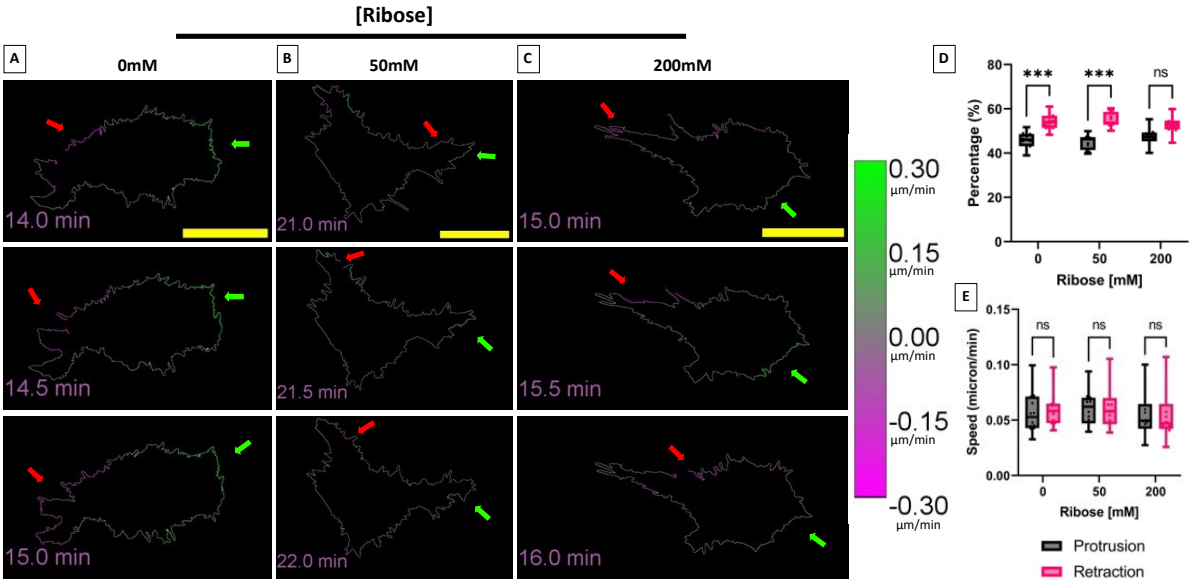

Figure 4.6 - Single-cell analysis of membrane dynamics 24-hours post-embedding show an increased degree of retraction in 0- and 50-mM ribose conditions.
A) Representative MIP images of single HeLa lifeact-mScarlet cell edges coloured for protrusion (green) and retraction (red) speed acquired on LLSM across 0-, **B)** 50- and **C)** 200-mM collagen-ribose matrices at a TR of 30-seconds over 30 minutes. **D)** Quantification of cell membrane protrusion and retraction as a percentage and **E)** velocity. Graph representing at least 12 measurements across 3 experimental repeats. Green arrows point to cell membrane extension and red retraction. All scale bars represent 20 μm. Error bars represent min to max, box-and-whiskers containing 25th/75th percentile and the median line. Asterisks indicate statistical significance between protrusion and retraction of ribose conditions when tested with Tukey's HSD post-hoc test following significant two-way ANOVA test (ns = not statistically significant, ***=p<0.001).

4.2.7 Sub-sampling LLSM TR shows reduced membrane speed measurements.

With no difference in the speed of protrusion and retraction of the cell membrane measured in matrices of different stiffnesses, significantly higher speeds were seen at 24-hours. When compared directly, ADAPT analysis showed a significant increase in the speeds measured at 24-hours of the cell membrane protrusion (**Figure 4.7.A**) and retraction speed (**Figure 4.7.B**) compared to 1-hour. To verify the impact of TR on the speed of the cell membrane measured, LLSM data from one cell was sub-sampled from 30-seconds to 10-minute, matching the TR of iSIM data.

TR sub-sampled data showed a decrease in the cell membrane speeds measured both during protrusion and retraction as opposed to full TR at 30-seconds, as is displayed in **Figure 4.7.C.** This shows the direct influence TR has on the outcome of structures measured, with higher TR resulting in higher dynamics of cell membrane speeds measured.

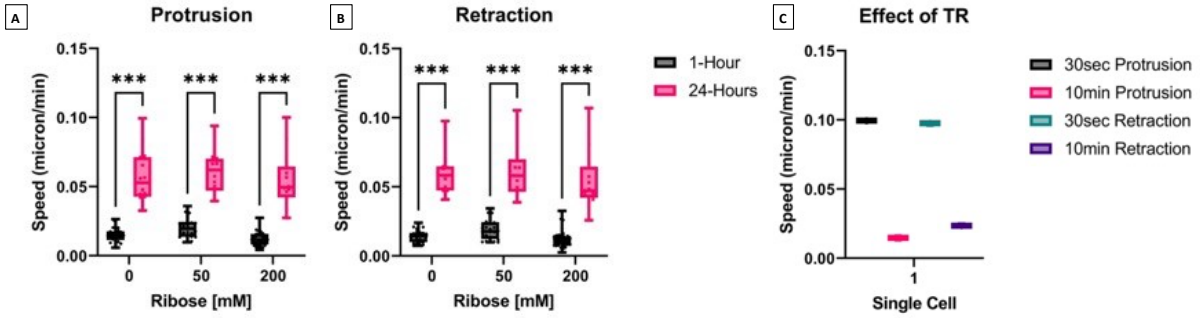

Figure 4.7 – TR sub-sampled data shows a decreased measure of protrusion and retraction cell membrane speed.
A) Quantification of cell membrane protrusion speed and **B)** retraction speed from iSIM data at 10-minute TR and LLSM data at 30-second TR. Both graphs represent at least 12 measurements across 3 experimental repeats. **C)** Quantification of cell membrane speed protrusion and retraction on same data set at 30-second and sub-sampled 10-minute TR. Error bars represent min to max, box-and-whiskers containing 25th/75th percentile and the median line. Asterisks indicate statistical significance between ribose conditions and different time points when tested with Tukey's HSD post-hoc test following significant two-way ANOVA test (***=p<0.001).

4.2.8 Stiffer collagen matrices show increased displacement by cells 1-hour post-embedding.

Analysing the impact of the cell on the surrounding matrix over time is important to understand the potential contributions of the cell protrusions to the remodelling of the ECM. The degree of remodelling in the surrounding matrix is directly influenced by the cell, as was seen in the AFT analysis from the previous chapter. Cross-correlation of time points to measure the maximum shift of ECM structure over time from single cells was initially performed in 2D on MIP images of 3D acquired iSIM images at 1-hour post-embedding (Yolland et al. 2019).

Cells in 0-mM ribose collagen gels assembled filopodia and lamellipodia that did not expand far into the matrix. Extending areas of the cell membrane showed the movement of collagen coincident with associated protrusive structures, highlighted by orange arrows. Additionally, a higher degree of displacement was seen in areas showing retracting protrusions, highlighted by white arrows, as displayed by composite, velocity and directional maps in **Figure 4.8.A**. Collagen fibres in 50-mM ribose gels showed no change in the matrix displacement but the movement appeared to be further from the cell centre compared to 0-mM ribose gels, as displayed in **Figure 4.8.B**. Collagen fibres in 200-mM ribose gels showed a higher speed of displacement compared to 0-mM ribose gels. Protrusion impact on the surrounding matrix showed a low displacement on extending protrusion but more significant on areas of heavy adhesion and support as displayed in **Figure 4.8.C** and reflected in the schematic and graph of 2D cross-correlation **Figure 4.8.D/E** respectively. Full time-lapse series of composite and velocity and directional maps available in **Supplementary Video 4.8.A/B/C**.

The 2D analysis provided a useful measure of collagen displacement and is relatively fast to perform, however, it omits the Z-axis information that likely affects the interpretation of the results. An algorithm to measure the structural shift in 3D, described in **Chapter 2.3.9**, was developed to analyse the full impact seen across all three axes from an initial source volume into a larger search volume along a common grid in the following 3D image stack, as represented by the schematic in

Figure 4.8.F. When collagen displacement was analysed in 3D, higher degrees of collagen displacement were noted compared to 2D analysis of corresponding collagen-ribose samples. When the Z-dimension is accounted for, a significant increase in the collagen displacement is seen in 50- and 200-mM collagen-ribose compared to 0-mM matrices, as displayed in **Figure 4.8.G**.

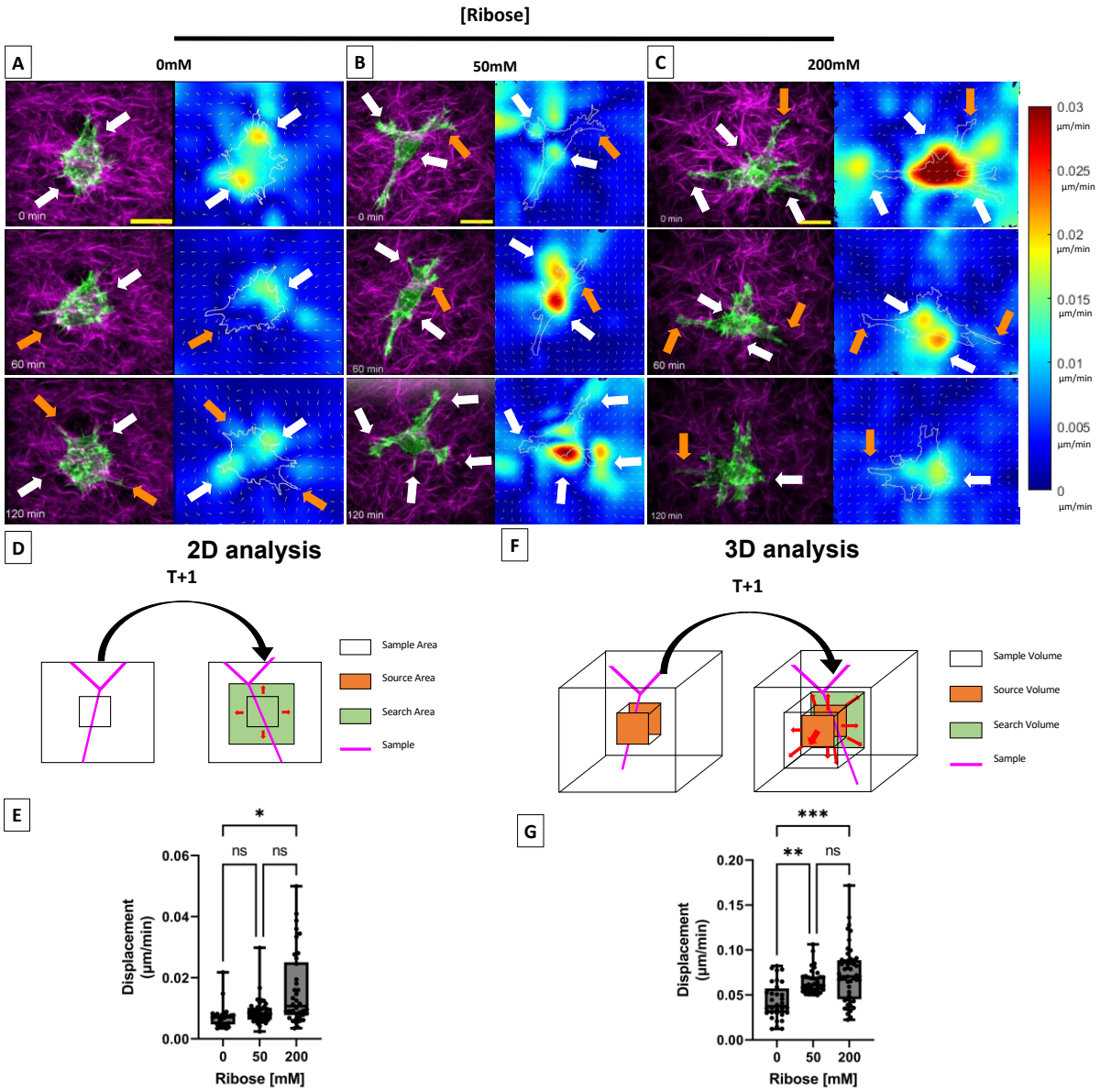

Figure 4.8 - 3D volume flow speed quantification at 1-hour shows a significant increase in displacement at higher stiffnesses and collagen-ribose matrices. **A)** Representative MIP images in Z acquired on iSIM of single HeLa lifeact-mScarlet cells (green) embedded in collagen (magenta) imaged 1-hour post embedding (TR of 10 mins) with corresponding 2D flow speed heatmap, vectors and cell edge of collagen displacement at 0-mM ribose **B)** 50-mM ribose and **C)** 200-mM ribose. **D)** Schematic representation of the 2D cross-correlation between two-time points of collagen sample (magenta) from source volume (orange) within larger search volume (green) of the following time point to quantify the maximum displacement. **E)** Quantification of collagen displacement at 1-hour post-embedding from 2D cross-correlation. **F)** Schematic representation of 3D volume cross-correlation between two-time points (magenta) from the source volume (orange) within a larger search volume (green) of the following time point to quantify the maximum displacement. **G)** Quantification of collagen displacement at 1-hour post embedding in 3D. Graphs represent at least 26 measurements across 4 experimental repeats. Orange arrows highlight protrusion extension and white arrows retraction. All scale bars represent 20 µm. All scale bars represent 20 µm. Error bars represent min to max, box-and-whiskers containing 25th/75th percentile and the median line. Asterisks indicate statistical

significance between ribose conditions when tested with Tukey's HSD post-hoc test following significant one-way ANOVA test (ns = not statistically significant, *=p<0.05, **=p<0.01 ***=p<0.001).

4.2.9 Stiffer collagen matrices show decreased displacement by cells 24-hours post embedding.

Analysis of single cell-dependent displacement of collagen 24-hours post-embedding in 0-, 50- and 200-mM imaged on the LLSM was initially performed in 2D, as displayed by composite MIP, velocity and directional images in **Figure 4.9.A/B/C**. Measurement of the MIP images in Z of the collagen colour channel and at 30-second TR, cross-correlation analysis showed a significantly higher degree of collagen displacement in the 50-mM collagen-ribose matrices compared to 200-mM, as represented in the graph in **Figure 4.9.D**.

As with 1-hour samples, higher measurements of collagen displacement were seen in 3D cross-correlation measurements over time as opposed to 2D analysis. 3D LLSM data needed to be sub-sampled to a TR of 5-minutes, for a reduced time of analysis, to be completed within the thesis time frame. Both 0- and 50-mM collagen-ribose matrices showed a significantly higher collagen displacement than 200-mM matrices when analysed across 3D, as displayed by the graph in **Figure 4.9.E**.

To verify that photobleaching of collagen did not affect the analysis of cross-correlation, data sets from both microscopes and TR were compared across all ribose conditions by the first half and final half of time points. This showed the photobleaching of collagen under these parameters had no significant effect in the analysis of the cross-correlation between time points of the samples, as is displayed in **Figure 4.9.F**.

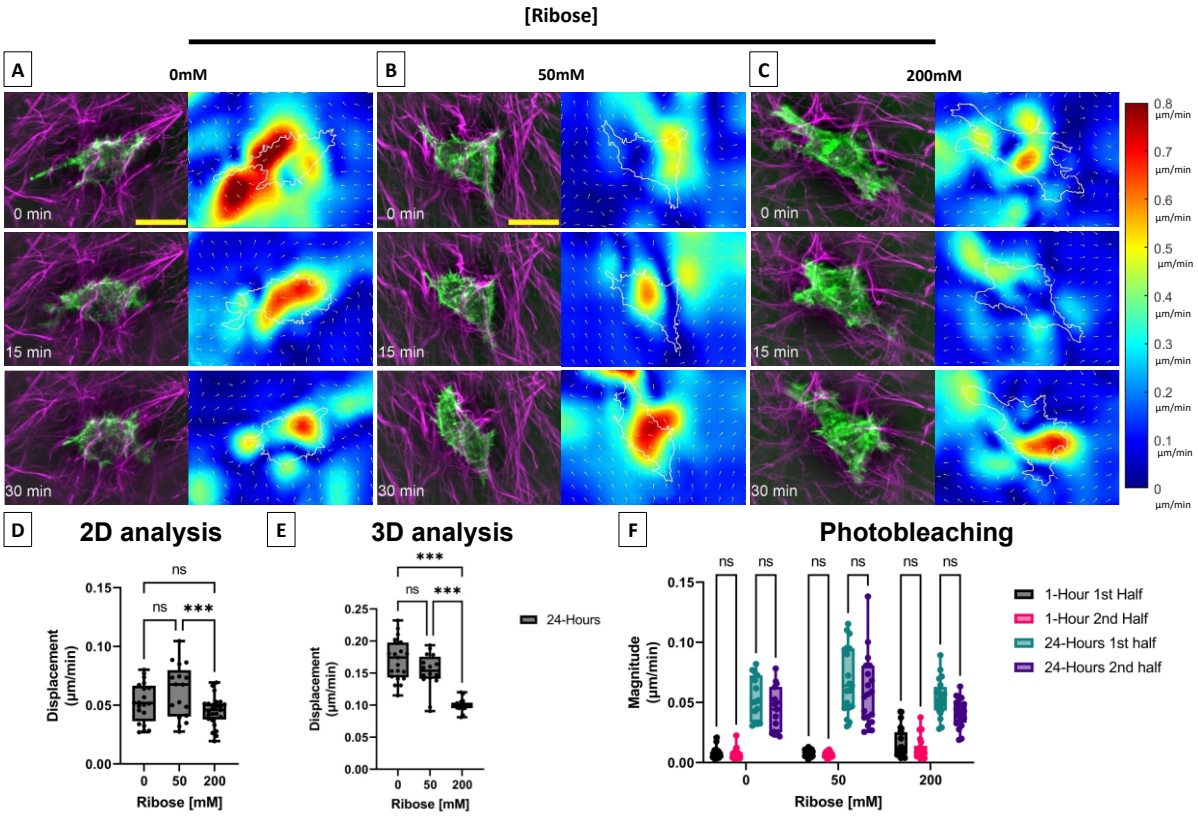

Figure 4.9 - 3D volume flow speed quantification at 24-hours shows a significant increase in displacement at lower collagen-ribose matrices, unaffected by bleaching.
A) Representative MIP images in Z acquired on LLSM of single HeLa lifeact-mScarlet cells (Green) embedded in collagen (Magenta) imaged 24-hours post embedding with a TR of 30 seconds with corresponding 2D flow speed heatmap, vectors and cell edge of collagen displacement at 0-mM ribose **B)** 50-mM ribose and **C)** 200-mM ribose. **D)** Quantification of collagen displacement at 24-hours post single cell embedding across 0-, 50- and 200-mM in 2D and **E)** 3D. **F)** Graph quantifying the 1st vs 2nd half of time-lapse series PIV analysis in 2D at 1- and 24-hours. Graphs representing at least 18 measurements across 3 experimental repeats. All scale bars represent 20 µm. Error bars represent min to max, box-and-whiskers containing 25th/75th percentile and the median line. Asterisks indicate statistical significance between ribose conditions and different time points when tested with Tukey's HSD post-hoc test following significant one-way ANOVA test (***=p<0.001, ns = not statistically significant).

4.3 Discussion

4.3.1 3D live single-cell imaging increases imaging and processing time compared to 2D

Imaging single cells in 3D collagen matrices over time using both the iSIM and LLSM resulted in large data files leading to memory intense processing. When storing images from samples across greater Z-distances, Z-resolutions, colour channels and increased time-points, greater memory capacity and RAM to transfer, open and process raw microscopy data is required. The compression, visualisation, processing, and analysis of this data have become more complex and require more advanced computational skills due to increased numbers of parameters seen in 3D and higher detail of biological data (Comes et al. 2019; Gibbs et al. 2021).

Most tools available for biological-image analysis have been developed for 2D images such as the ADAPT program (Barry et al. 2015) and 2D cross-correlation (Yolland et al. 2019) used in this chapter. In the case of ADAPT, no version is available for 3D data sets and therefore was performed on the MIP of our single cells. These results may offer indications of single cell activity however, to fully extrapolate, without loss of data, requires further investing in the developments of analysis tools specifically across all 3D. 3D cross-correlation analysis, developed to measure collagen displacement without needing to minimise data, yielded significantly different magnitudes and trends between 2D and 3D analysis. Evidenced by 50-mM collagen displacement at 24-hours being higher than 0-mM in 2D analysis but lower in 3D, as displayed in **Figures 4.9.D** and **E**.

The trade-off for the ability to image the entirety of 3D live cell data sets is the significantly higher time to process and run analysis. 2D cross-correlation offered the advantage of analysis being performed on MIP in minutes as opposed to the equivalent 3D data set requiring days/weeks. Sub-sampling of LLSM from 30-second TR to 5-minute TR was performed for 3D collagen displacement analysis to be completed on time for this thesis. Though offering greater insight into the dynamics of single cells embedded in collagen, when analysed across all dimensions significant development and time were required. Many more advances are required

to reduce the analysis time and keep up with ever-bigger data sets that accompany advances in live cell imaging.

4.3.2 Z-resolution and TR impact the outcome of analysis performed in 3D live cell imaging.

The data from this chapter demonstrated the successful methods used for capturing the 3D dynamics of single HeLa lifeact-mScarlet cell embedded in Alexa647-SE labelled collagen-ribose matrices of increasing stiffnesses. Cell dynamics were captured at 1-hour post-embedding on the iSIM and 24-hours on the LLSM. Due to the iSIM illumination method and properties, minimal laser power, exposure time and depth penetration were required to avoid cytotoxicity and scattering (Curd et al. 2015; Zhovmer and Combs 2021). A larger distance between Z-planes and the consecutive imaging of colour channels also enabled the acquisition of samples at a 10-minute TR without inducing cell visible toxicity. Due to the properties of the LLSM, solely the plane of interest is illuminated and enabled the rapid acquisition through Z of both colour channels sequentially. This resulted in a maximum TR of 30-seconds, offering even greater insight into the dynamics of the cell-ECM relationship over time (Chen et al. 2014).

Although cell death was not induced, samples suffered greater degrees of photobleaching in both fluorescent channels with every 3D time-point acquired. The differences in microscopy illumination and TR impacted the samples in different ways. Due to the widefield illumination mode of the iSIM, collagen labelled Aleaxa647-SE photobleaching was greater, but the low TR enabled the fluorescent recovery of HeLa lifeact-mScarlet which reduced apparent photobleaching in this channel. The LLSM showed similar photobleaching in both channels, likely because the higher TR decreased the lifeact-mScarlet fluorescence recovery time and light sheet illumination reduced the exposure to light. It is important to note for all future experiments, fluorescence labelling methods become a limiting factor for photobleaching unless done at high TR where the cell is unable to sufficiently recover. Loss of signal and structure can have an important impact on the analysis and quantification of data and should be properly verified in all future work (Tinevez et al. 2012). However, although photobleaching was significant in many samples, it did not contribute to the analysis of data under these parameters as shown in **Figure 4.9.F**.

Data acquired from both the iSIM and LLSM showed significant variations in the quantification of cell membrane retraction and protrusion speed. Differences in the Z-resolution and TR at which the samples were imaged also contributed to the quantification of dynamic structures. Sub-sampled data from the LLSM, **Figure 4.7**, showed a significant variation in the membrane protrusion and retraction speeds measured when going from 30-second TR to 10-minute TR. Due to the effect TR plays in analysis, the higher the TR achieved, the closer it is to capturing the true real-time dynamics of structures being imaged. This careful balance between 3D resolution, volume ROI required, and acquisition speed of structures, are all pivotal in how close to the true dynamics of single cells in 3D matrices are captured. To appropriately compare the dynamics of single cells and matrices of varying stiffnesses, microscopy techniques should remain as consistent as possible, as Z-resolution and TR influence the outcome and interpretation of analysis (Comes et al. 2019). iSIM and LLSM datasets have differences in temporal and spatial resolution and are therefore not directly comparable but can be used for comparative measurements influenced by stiffness. For future work, the experimental protocol of acquisition should be adapted and consistent for greater interpretation of microscopy images.

4.3.3 Traction forces of the cell on the surrounding matrix are greater in stiffer matrices

The dynamics of single cells imaged at 1-hour post embedding showed the stiffness of matrices to have an immediate impact on the morphology and dynamics of single cells, with a more protrusive phenotype evident under higher stiffnesses. Previous studies of epithelia cultured on stiff 2D substrates and softer more compliant 3D matrices showed increased integrin expression and cytoskeletal structure with that of stiffer substrates (Yeung et al. 2005). Soft matrices caused a rapid turnover of fine actin structures (**Figure 4.1.A)**, largely comprising filopodia and lamellipodia, that showed minimal deformation of the surrounding collagen (**Figure 4.8.G**). This coupled with higher rates of cell membrane retraction (**Figure 4.5.D**) and the small magnitude of centroid shift (**Figure 4.4.C**) showed that single cells were unable to mobilise within or adhere stably to softer matrices. In contrast, the stiffest (200-mM) matrices showed higher protrusive activity (**Figure 4.1.C**), directly imposing high displacement on the surrounding matrix (**Figure 4.8.G**) due to increased adhesion coupled with higher rates of membrane retraction (**Figure 4.5.D**). This accurately reflects what previous studies have demonstrated, showing low stiffness substrates cell adhesion to be labile with cortical actin being diffusely distributed, and high stiffness substrates increasing adhesion strength and actin bundle development and aligned fibres generating higher forces (Doyle et al. 2015; Hall et al. 2016; Solon et al. 2007).

Cells in 50-mM collagen-ribose matrices exhibited a high turnover of membrane protrusion (**Figure 4.1.B)** and showed a significant degree of collagen displacement (**Figure 4.8.G**). These results coupled with a significantly higher centroid shift (**Figure 4.4.C**) indicate a more mobile phenotype with the cell upregulating traction forces on the ECM. However, the lower stiffness of the collagen compared to 200-mM conditions may not support the high traction forces, leading to less consistent ECM deformation compared to higher stiffness environments. Though cells presented a heterogenous degree of mobility and activity, imaging over 2-hours at early time points showed the ECM stiffness correlated with the stability of the cell cytoskeleton. Softer ECM provided little support for the cell to impose traction forces and no tangible directional protrusion. The increased cell traction forces still require a

high degree of cytoskeletal stability to support directional movement through established pseudopodia. As stiffness increases, greater support is offered for cytoskeleton tractional force but consequently remodelling becomes harder. 50-mM showed the most versatile level of support for cell traction whilst simultaneously offering more ease in remodelling to adapt its environment for greater cell migration.

The ECM degree of compliance has been shown to play an important role in influencing the contractility of the cell and Rho family GTPases activity (Wozniak et al. 2003) and cytoskeletal tension the assembly of focal adhesions (Burridge and Wennerberg 2004). Low centroid shift (**Figure 4.4.C**), high collagen displacement (**Figure 4.9.E**) and the selective upregulation of lamellipodia into more defined pseudopodia were seen after 24h post-embedding, suggesting cells establish structural support and upregulate tractional force on the ECM in response to a stiffer environment.

At 24-hours post-embedding, single cells in collagen-ribose matrices displayed no difference in centroid shift (**Figure 4.4.C**) or speed of cell membrane retraction and protrusion across different stiffnesses (**Figure 4.6.E**). Cells maintained a dynamic migratory phenotype and displayed a clear leading protrusion and retracting cell body at the rear. This has been shown to cause a rear-to-front hydrostatic pressure compartmentalisation that further enhances front protrusion and movement (Petrie, Koo, and Yamada 2014). However, cells in 200-mM collagen-ribose matrices showed an equal percentage of membrane protrusion and retraction (**Figure 4.6.D)** and a reduced displacement on the surrounding collagen (**Figure 4.9.E**) indicating this stiffness may better support single-cell invasion. For the same degree of mobilisation, single cells in 0- and 50-mM ribose matrices require a significantly higher level of membrane retraction and remodelling of collagen fibres. Imposing equal tractional force on softer matrices will cause a greater displacement of the more malleable fibres until taught enough to fully support the force imposed by the cell.

Early time points show the rate at which cells can upregulate their cytoskeleton directly relies on the structural support. Softer matrices are more highly remodelled over time due to their more malleable nature and are unable to withstand the traction forces being applied by the cell. Only once reaching a certain degree of stability or structural integrity is the matrix able to offer enough support for the cell to migrate along. Other studies have effectively shown how mechano-sensing, directionalities in cell alignment, cell migration, protrusion dynamics and matrix remodelling are highly integrated, the orientation of remodelled matrix being highly aligned to the direction of the mechanical force (Pang et al. 2011). Adhesion sites and actin nucleation have been shown to preferentially grow along highly organised and aligned substrate edges (Doyle et al. 2015; Ray et al. 2017; Sun et al. 2015), as we see across all ribose conditions at 24-hours.The orientation of the ECM mediates tension dependent cell migration in developmental processes such as gastrulation (Keller, Davidson, and Shook 2003) and rigidity guiding cell growth and motility (Engler et al. 2004; C. M. Lo et al. 2000). Tumour rigidity reflects increases in stromal stiffness and tumour cell tension. Small increases in the rigidity to the matrix enhance growth by inducing Rho-generated cytoskeletal tension to promote FA assembly and increase GF-dependent ERK activation (Paszek et al. 2005). These interactions by invading tumour cells applying force to the ECM thereby aligning the collagen fibres to provide a highway passage for accelerated cell migration (Gaggioli et al. 2007; Goetz et al. 2011). The dynamics of protrusion with the surrounding matrices offer insight into the mechanisms by which the cell explores, adapts, and utilises its surrounding ECM to mobilise. Further exploring the dynamics of leading protrusions in single cells will shed light on the sequence of events made by the cell to navigate and remodel the surrounding ECM at different stiffnesses.

5 Mesoscale impact of single cell protrusions dynamics on the local ECM at varying stiffnesses

5.1 Introduction

From the previous chapter, analysis of entire single HeLa cells embedded in collagen-ribose matrices showed that cells in lower stiffness matrices required a significantly higher level of membrane retraction to remodel collagen fibres. Cells exerted greater remodelling effects on the ECM in softer matrices likely due to the more malleable nature and reduced traction forces (Spill, Bakal, and Mak 2018). Moreover, a threshold of ECM stability or structural integrity was required to provide sufficient support for the cell to migrate along. The cells impose tractional force on the ECM and are able to subsequently migrate due to dynamic protrusions. Therefore, the dynamics of these single cell protrusions are essential to understand the relaying of mechanical information from the matrix to the cell. This requires imaging of protrusion dynamics in 3D over time to provide greater insight into the complex relationship ECM stiffness has on single-cell behaviour.

In order to detect the surrounding structures and properties of the ECM, cells dynamically remodel the F-actin cytoskeleton. When adhesion and traction forces are higher, migrating cells adopt a ‘mesenchymal’ morphology with integrin-based adhesions generating higher levels of traction (Doyle et al. 2015a). Actin based protrusions play a vital role in increasing the surface area explored through branched F-actin networks, such as the formation of lamellipodia, and fine parallel bundles of F-actin, such as filopodia. Filopodia extend off protrusions to explore the local structures, acting as a mechanosensory probes of the ECM (Arjonen, Kaukonen, and Ivaska 2011; Mattila and Lappalainen 2008). Actin polymerization at the leading edge of protrusions also facilitates the rapid movement of integrins to the cell front. These actin-rich, highly dynamic structures are used to expose higher numbers of integrin complexes to the surrounding matrix ligands in order to relay mechanosensory information through integrin signalling pathways (Palecek et al. 1997). Additionally, trafficking of integrins regulates their cell-surface availability through endocytosis and recycling to the plasma membrane (Ezratty et al. 2009) enabling further regulation of integrin availability (Paul, Jacquemet, and Caswell 2015).

Initially, small focal adhesions called focal complexes are formed at the leading edge of the cell protrusion, consisting of integrins and adapter proteins, such as talin, paxillin and tensin (Zaidel-Bar et al. 2004). Many of these focal complexes fail to mature and are disassembled as the lamellipodia retracts. Signalling through integrins is vital for the formation of mature focal adhesion complexes, enabling mechanical links between the cell and ECM to impose tractional forces. In motile cells, focal adhesions are being constantly assembled and disassembled as the cell establishes new contacts at the leading pseudopodia end and breaks old contacts at the trailing edge of the cell (Zaidel-Bar et al. 2004). Focal adhesions anchor the ends of actin filaments to the substrate and through actomyosin contractility, enable the cell to migrate (Mierke et al. 2017).

The intricate relationship between integrin clustering, focal adhesions and the actin cytoskeleton is essential in cell survival, migration, and metastasis of tumours in 3D tissue. Exploring the finer dynamics of leading protrusions in single cells will help shed light on the steps made by the cell to navigate and remodel the surrounding ECM at different stiffnesses in a 3D environment. The parameters used in the previous chapter with the LLSM for live-cell imaging in 3D, showed no cytotoxic effect or photobleaching on HeLa lifeact-mScarlet cells or Alexa647-SE labelled collagen-ribose matrices. Using this same live-cell imaging method, HeLa lifeact-mScarlet cell protrusion and matrix dynamics were captured on the LLSM at 24-hours in 3D. In this chapter protrusions were imaged regardless of cell volume size to better dissect the dynamics, incorporating trends of a non-migratory phenotype initially captured in chapter 3 on the iSIM at 1-hour. This offers the potential to further dissect the dynamics of protrusion activity on the remodelling around protrusions when unable to migrate into new matrix at 24-hours. This will offer greater understanding in dissecting the dynamics from protrusion activity and their role in remodelling of the local matrix structures at different stiffnesses.

5.2 Results

5.2.1 Single cell protrusion at 24-hours adopts similar morphologies despite increased stiffness of matrices.

To further explore the impact imposed by single cells on the surrounding collagen matrix and the specific role protrusions play in ECM remodelling, HeLa lifeact-mScarlet cells and Alexa647-SE labelled collagen were imaged using 3D time-lapse microscopy. Imaging was performed on single cell protrusions 24-hours post embedding in 0-, 50- and 200-mM collagen-ribose matrices at a TR of 30-seconds over 30 minutes. The live-cell imaging parameters from the previous chapter showed no detrimental impact on protrusion activity and allowed the capturing of the finer dynamic features of single cell protrusions and surrounding matrix once initial adaptation to the surrounding matrix passed.

Protrusions and the corresponding cell body were imaged in 0-, 50- and 200-mM collagen-ribose matrices, were F-actin structures ranging from filopodia to bundled stress-fibres were consistent with the results from the previous chapter, across all 3 collagen-ribose concentrations. Filopodia were observed rapidly extending and retracting from the main protrusion end, probing the surrounding collagen structures. F-actin structures showed high alignment or contact with collagen fibres at the protrusion ends, mobilising and inducing local collagen fibre displacement. Representative 5-minute MIP images of both the protrusion and corresponding cell body in Z of HeLa lifeact-mScarlet cells and Alexa647-SE labelled collagen, in green and magenta respectively, across all 3 ribose conditions, are shown in **Figure 5.1.A/B/C**. Temporally coloured edges for entire imaging period are shown at 5-minute intervals over 30 minutes (far right panels). Full 30-second TR over 30 minutes available in **Supplementary Video 5.1.A/B/C**.

These representative images demonstrate that a variety of protrusion dynamics were seen across all 3 ribose conditions.

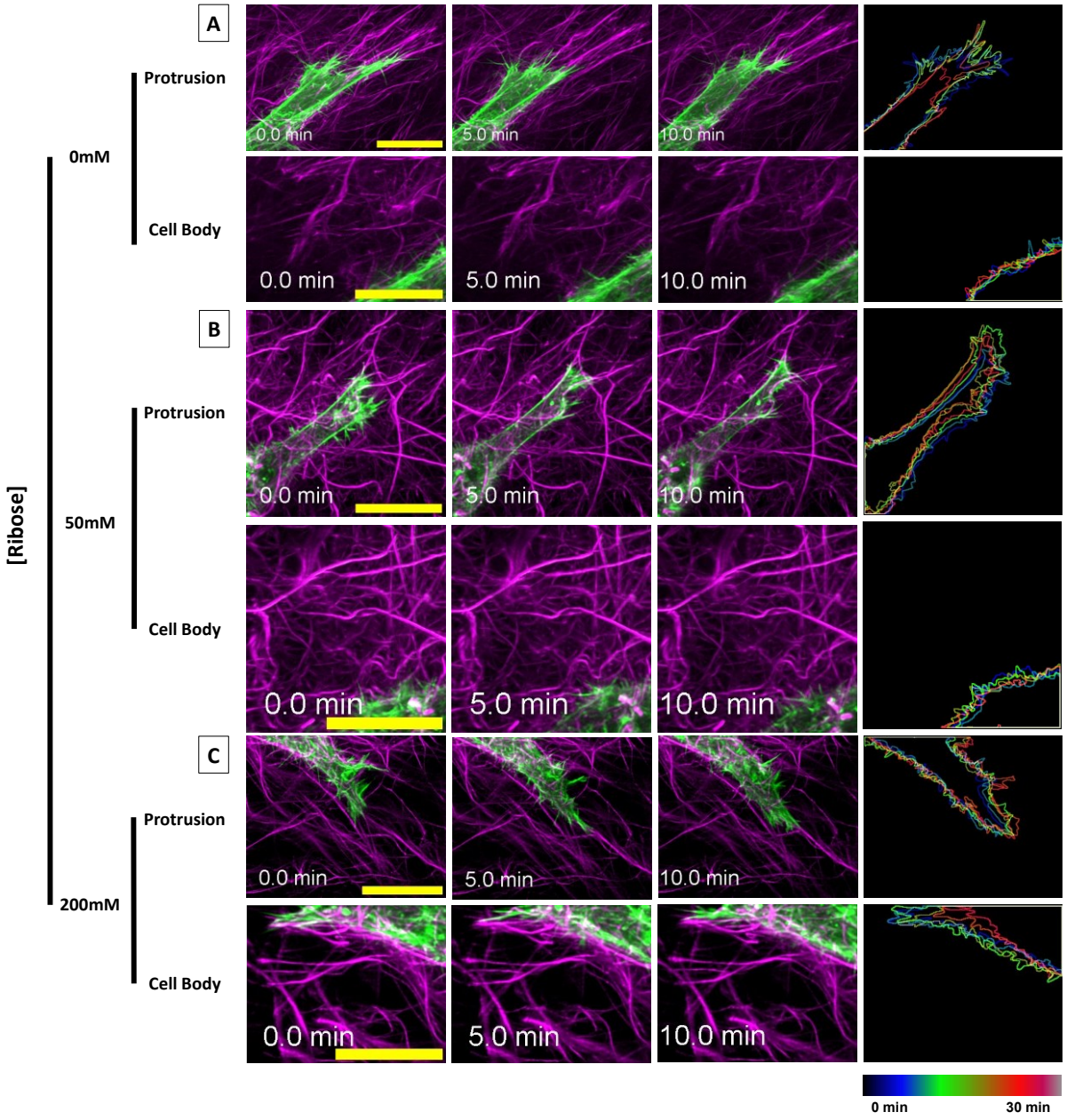

Figure 5.1 – Single cell protrusion at 24-hours adapt similar morphologies despite increased stiffness of matrices.
Representative MIP images of protrusions and corresponding cell body in Z acquired on LLSM of Single HeLa lifeact-mScarlet cells (Green) embedded in collagen (Magenta) at TR of 30-seconds. **A)** 0-mM, **B)** 50-mM and **C)** 200-mM collagen-ribose matrix with corresponding cell edges temporally colour coded at 5-minute intervals.

5.2.2 Protrusions show a consistent speed but increased percentage of membrane retraction in matrices of 0-mM collagen-ribose.

Changes in cell morphology are required to influence ECM remodelling through the extension and retraction of the cell membrane. These are important sites of mechanotransduction to direct and inform on the cells response to surrounding structures through integrin-ECM binding. To quantify this phenomenon, cell membrane extension and retraction were analysed using the ADAPT plugin (Barry et al. 2015), from MIP images from time-lapse series.

The areas of membrane speed extension (green) and retraction (magenta) in matrices of 0-, 50- and 200-mM are displayed as membrane edge velocity maps in **Figure 5.2.A/C/E.** Localised areas of extension along the protrusion are highlighted by green arrows, and retraction highlighted by red arrows, in structures such as filopodia (**Figure 5.2.A)**, protrusion body (**Figure 5.2.C)** and protrusion ends (**Figure 5.2.E**). Analysis showed a high velocity of membrane extension and retraction along the protrusion body through to the protrusion tip, allowing for the dynamic shift of the total protrusion and finer F-actin structures. The corresponding dynamics of the displayed protrusion membrane speed can be seen in **Figure 5.2.B/D/F** with displayed images marked between green highlighted lines. Full 30-second TR over 30 minutes of ADAPT edge velocity maps available in **Supplementary Video 5.2.A/C/E**.

A significantly higher percentage of membrane retraction was seen in 0-mM collagen-ribose matrices compared to higher stiffness matrices as shown in **Figure 5.2G**. 50- and 200-mM collagen-ribose protrusions showed an equal rate of cell membrane extension and retraction. No difference in membrane extension or retraction speeds were seen in matrices of 0-, 50- or 200-mM ribose, as shown in **Figure 5.2H**.

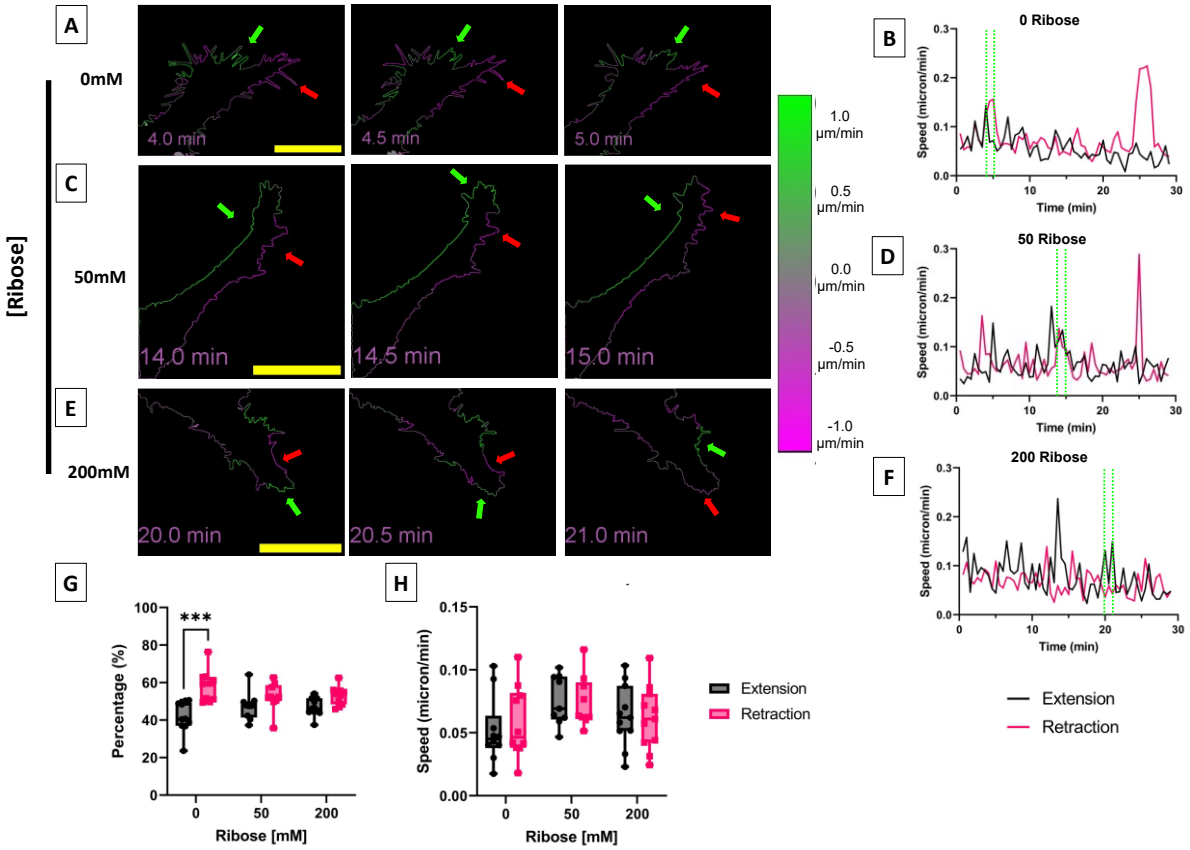

Figure 5.2 – Protrusions show a consistent speed but increased percentage of membrane retraction in matrices of 0-mM collagen-ribose.
Representative MIP images of single HeLa lifeact-mScarlet cell protrusion edges coloured for extension (green) and retraction (magenta) speed acquired on LLSM across **A)** 0-mM, **C)** 50-mM and **E)** 200-mM collagen-ribose matrices at a TR of 30-seconds over 30 minutes. Dynamics of cell membrane extension and retraction speed at **B)** 0-mM, **D)** 50-mM and **F)** 200-mM with displayed images marked between green dotted lines. **G)** Quantification of cell membrane extension and retraction as a percentage and **H)** velocity. Graph representing 10 measurements across 3 experimental repeats. Green arrows point to cell membrane extension and red retraction. All scale bars represent 20 μm. Error bars represent min to max, box-and-whiskers containing 25th/75th percentile and the median line with asterisks indicating statistical significance by Šídák multiple comparisons post-hoc test between ribose concentrations within conditions following two-way ANOVA (***=p<0.001).

5.2.3 Cells show a uniform degree of extension and retraction, operating at twice the speed in protrusions, across all ribose concentrations.

The previous figure demonstrated a higher percentage of the membrane retraction occurring in cells in 0-mM collagen-ribose matrices, and no difference in the speed of protrusion extension and retraction. To determine whether this behaviour related only to distal protrusions, the membrane dynamics of the cell body were also analysed. The corresponding dynamics of the displayed cell body membrane speed can be seen in **Figure 5.3.A/B/C**. Full 30-second TR over 30 minutes of ADAPT edge velocity maps available in **Supplementary Video 5.2.A/C/E**. Cell body dynamics showed an increased amount of membrane retraction occurring in 200-mM collagen-ribose matrices, as displayed in **Figure 5.3.D,** but no difference in extension or retraction speed of the cell body membrane quantified, as displayed in **Figure 5.3.E**.

Protrusion to cell body dynamics showed no difference in the amount of membrane extension or retraction occurring between 0-, 50- and 200-mM collagen-ribose matrices, as displayed in **Figure 5.3.F**, indicating a uniform membrane degree of extension and retraction across the whole cell body. However, the velocity of membrane protrusion was two-fold higher compared to that of the cell body, in 0-, 50- and 200-mM ribose concentration, as is displayed in **Figure 5.3.G**. This increase in protrusion dynamics over cell body membrane dynamics was equal across all matrix stiffnesses.

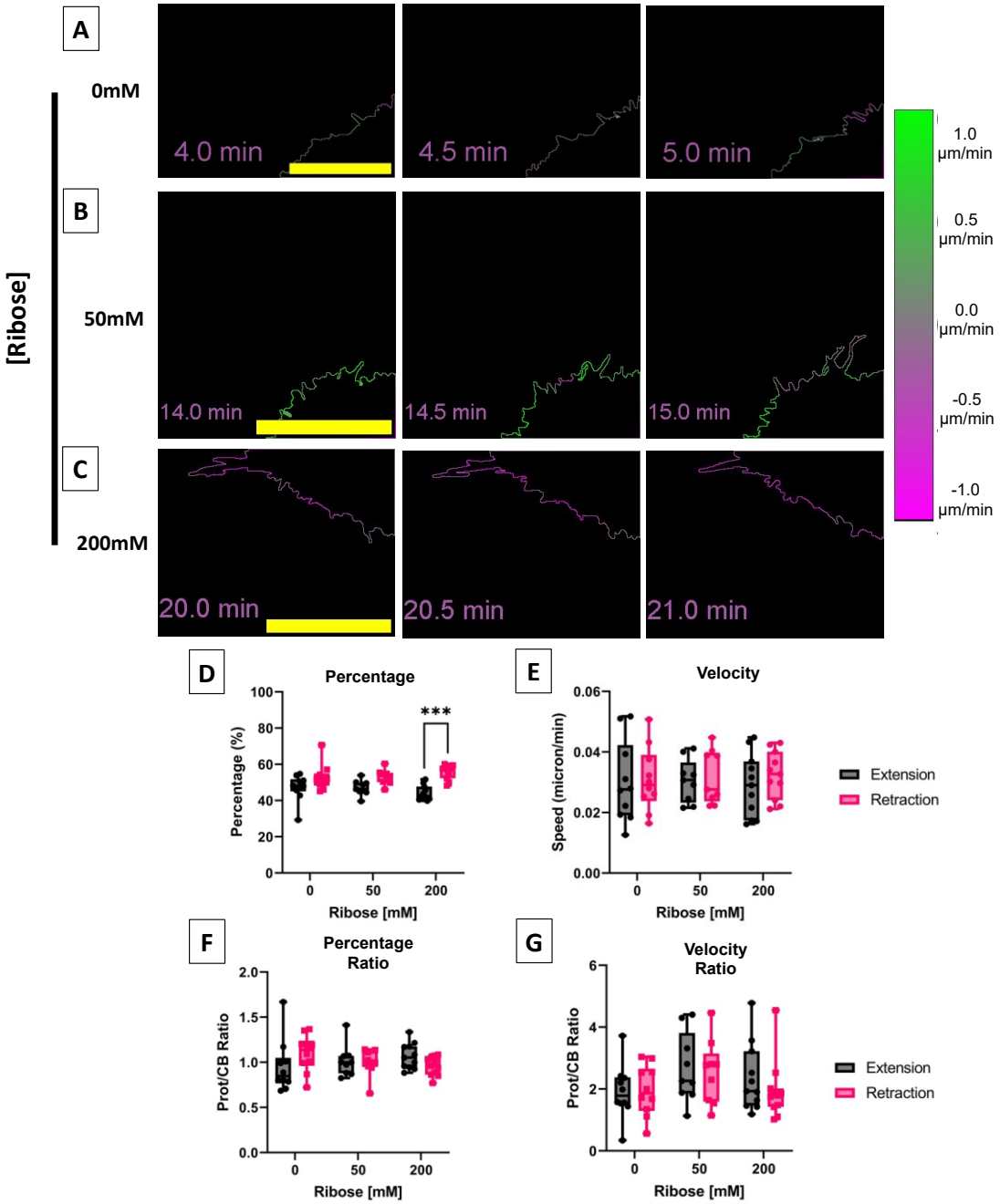

Figure 5.3 - Dynamics of protrusion to cell body ratio shows no difference in measure of extension and retraction dynamics.
Representative MIP images of single HeLa lifeact-mScarlet cell protrusion edges coloured for extension (green) and retraction (magenta) speed acquired on LLSM across **A)** 0-mM, **B)** 50-mM and **C)** 200-mM collagen-ribose matrices at a TR of 30-seconds over 30 minutes. **D)** Quantification of cell body membrane extension and retraction as a percentage and **E)** velocity. **F)** Quantification of protrusion to cell body ratio of percentage and **G)** velocity of cell membrane extension and retraction from LLSM data at 30-second TR. Both graphs represent 10 cells across 3 experimental repeats. All scale bars represent 20 μm. Error bars represent min to max, box-and-whiskers containing 25th/75th percentile and the median line with asterisks indicating statistical significance by Tukey's multiple comparisons post-hoc test between ribose concentrations within conditions following two-way ANOVA (***=p<0.001).

5.2.4 Flow speed quantification of protrusion actin dynamics shows no increase in velocity across collagen-ribose matrices.

Analysing F-actin dynamics is important to understand the potential correlation between cell cytoskeleton and ECM remodelling. The degree of remodelling is directly influenced by the cell, as shown by AFT analysis in chapter 3 (**Figure 3.5**) and dynamic volume flow analysis in chapter 4 (**Figure 4.9**). 2D cross-correlation of time points at 30-second TR was therefore used to determine the spatial directional flow of actin in cells within matrices of different stiffnesses.

Analysis of lifeact-mScarlet in protrusions in cells 24-hours post-embedding in 0-, 50- and 200-mM collagen ribose on the LLSM showed dynamic F-actin localisation and directional flow along both the protrusion body and tip. The velocity and directional MIP images of protrusion and corresponding cell body in Z for 0-, 50- and 200-mM collagen-ribose samples are displayed in **Figure 5.4.A/C/E**, respectively, and protrusion F-actin dynamics over 30 minutes in **Figure 5.4.B/D/F,** with images shown denoted between the green dotted lines**.** Cells in 0- and 50-mM collagen-ribose gels show tractional forces propagating from the protrusion tip towards the cell body. Cells in 200-mM collagen-ribose gels showed localised retraction occurring at the tip of protrusions with lower velocities visible along the protrusion body. The increased speed of displacement and directionality of lifeact-mScarlet was coupled to both the extension of the cell membrane further into the collagen and in protrusion tips moving towards the cell body.

Quantification of these behaviours revealed no significantly higher velocity between collagen-ribose gels, as quantified in **Figure 5.4.G**. There were no differences in F-actin flow in protrusions relative to the cell body across all ribose conditions, as displayed in **Figure 5.4.H**. Full 30-second TR over 30 minutes of flow speed velocity and directional maps available in **Supplementary Video 5.4.A/C/E**.

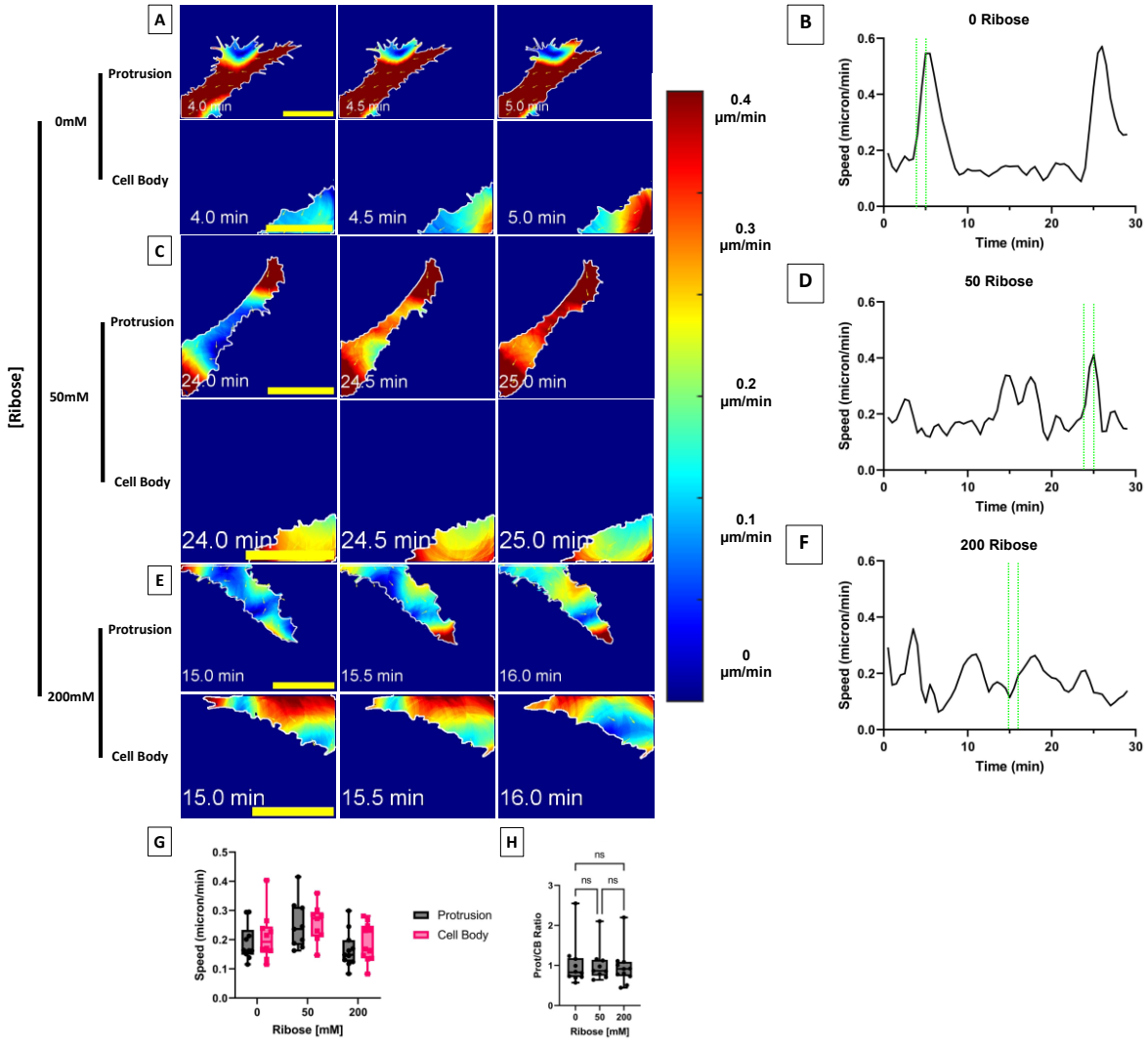

Figure 5.4 – Actin flow speed in protrusions remains consistent across all collagen-ribose matrices.
A) Representative images of 2D flow speed heatmap, vectors and cell edge of lifeact-mscarlet displacement, imaged at 30-second TR for 30 min of the cell body and protrusions embedded across 0-mM, **C)** 50-mM and **E)** 200-mM collagen-ribose matrices. Dynamics of lifeact-mscarlet speed at **B)** 0-mM, **D)** 50-mM and **F)** 200-mM with displayed images marked between green dotted lines. **G)** Quantification of actin flow speed in protrusions and **H)** protrusion to cell body ratio. All scale bars represent 20 μm. Graph representing 10 measurements across 3 experimental repeats. Error bars represent min to max, box-and-whiskers containing 25th/75th percentile and the median line with asterisks indicating statistical significance by Tukey's HSD post-hoc test between ribose concentrations within conditions following two-way ANOVA (ns = not statistically significant).

5.2.5 Flow speed quantification of collagen dynamics around protrusion shows a slight increase in displacement at 50-mM collagen-ribose matrices.

ECM remodelling is influenced by cell protrusion, either through adhesion and tractional force, de-adhesion of integrins and the amount of permanent deformation imposed by the cell. To understand the relationship between these parameters, displacement of Alexa647-SE labelled collagen structures was analysed over time on MIP images from 3D Z-stacks acquired on the LLSM.

The velocity and directional movement of collagen surrounding cell body and protrusion in 0-, 50- and 200-mM collagen-ribose samples are displayed in **Figure 5.5.A/C/E**, respectively, and corresponding protrusion dynamics over 30 minutes in **Figure 5.5.B/D/F** with images shown indicated by green dotted lines**.** Several phenotypes were observed. Higher displacement indicates higher adhesion and tractional force being applied on the matrix by the protrusion, and the directionality indicates collagen displacement relative to protrusion traction. In cases where these two measurements occurred in opposite directions, indicating loss of adhesion, the collagen was seen to undergo recoil as displayed in **Figure 5.5.A**. This recoil did not always result in restoration of collagen organisation, as the tractional forces from cells can lead to permanent deformation, due to the viscoelastic properties of the ECM. If the measurements occurred in the same direction, this indicated adhesion of the cell to the collagen and contraction on the matrix, as displayed in **Figure 5.5.C**. Greater displacement would indicate higher adhesion to the surrounding ECM. However, different areas of the same protrusion were also seen to display a combination of these phenotypes such as that shown in **Figure 5.5.E,** where collagen recoil occurs within the protrusion length but simultaneous movement of the collagen towards the cell body at the protrusion tip.

Collagen structure displacement was also seen to occur from the cell body while applying higher contractile forces at the protrusion end, as seen in **Figure 5.5.A/C**. Contraction at the protrusion tip increased tractional force applied on anchored structures near the cell body to impose deformation to the ECM, which is expected to

be more malleable in lower stiffness matrices. This suggests plasticity of the cell in modifying its contractility, adhesion, and remodelling properties through high dynamic turnover of F-actin and adhesive structures to manipulate the ECM.

Further quantification demonstrated no significant differences in the degree of actin displacement between ribose conditions as shown in **Figure 5.5.G**. Collagen around the protrusion in cells within 50-mM gels showed significantly higher displacement relative to the cell body compared to 0-mM gels as shown in **Figure 5.5.H**. However, more data sets are required to verify these trends. Full 30-second TR over 30 minutes of flow speed velocity and directional maps available in **Supplementary Video 5.5.A/C/E**.

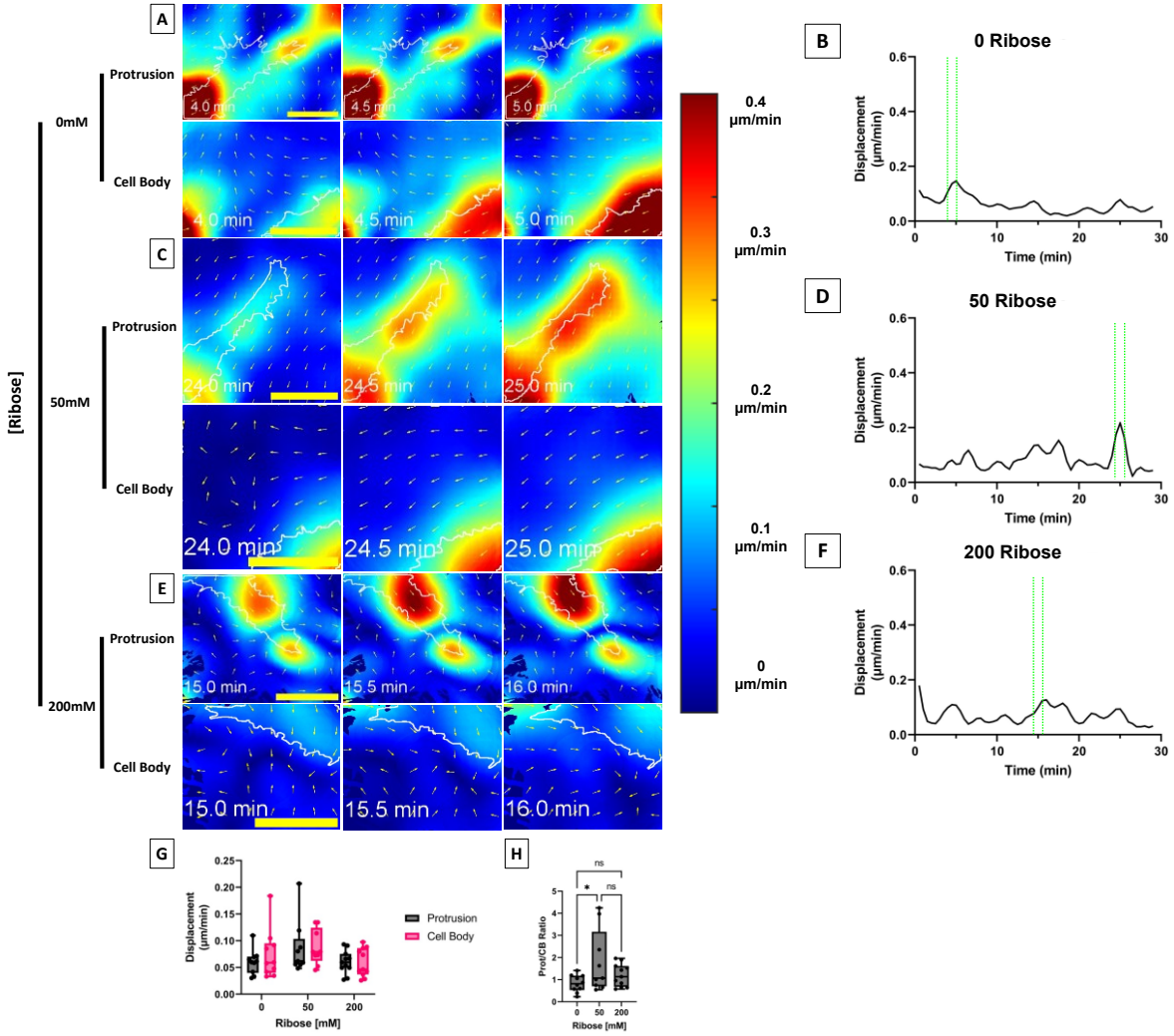

Figure 5.5 – Flow speed quantification of collagen dynamics around protrusion shows a slight increase in displacement at 50-mM collagen-ribose matrices. Representative images of 2D flow speed heatmap, vectors and cell edge of collagen displacement by protrusions imaged at 30-second TR for 30 min across **A)** 0-mM, **C)** 50-mM and **E)** 200-mM collagen-ribose matrices. Dynamics of collagen displacement at **B)** 0-mM, **D)** 50-mM and **F)** 200-mM with displayed images marked between green dotted lines. **G)** Quantification of collagen displacement flow speed in area around protrusions and **H)** protrusion to cell body ratio. Graph representing 10 measurements across 3 experimental repeats. All scale bars represent 20 µm. Error bars represent min to max, box-and-whiskers containing 25th/75th percentile and the median line with asterisks indicating statistical significance by Tukey's HSD post-hoc test between ribose concentrations within conditions following two-way ANOVA (*=p<0.05).

5.2.6 F-actin and adjacent collagen fibre alignment are heterogeneous and uncoupled.

To determine whether the degree of structure alignment in both the cytoskeleton and collagen matrices were correlated, AFT analysis was performed on fibrillar features using Fourier transformation (Marcotti et al. 2021). The order parameter of structures was measured whereby a score of 1 indicates a perfect alignment, 0 a randomly oriented and -1 indicates orthogonal alignment of neighbouring structures. Heatmap outputs with vector angle of neighbouring structures of representative images of the cell body, protrusion F-actin and surrounding collagen to both at 0-, 50- and 200-mM ribose concentration are shown in **Figure 5.6.A/C/E.** The corresponding protrusion dynamics over 30 minutes in **Figure 5.6.B/D/F** with displayed images indicated by the green dotted lines**.**

Analysis demonstrated no significant difference in the co-alignment of adjacent F-actin and collagen fibres across ribose conditions of the cell body and protrusion, as shown in **Figure 5.6.G and H** respectively, or in the order parameter of the protrusion relative to the cell body as displayed in **Figure 5.6.I**.

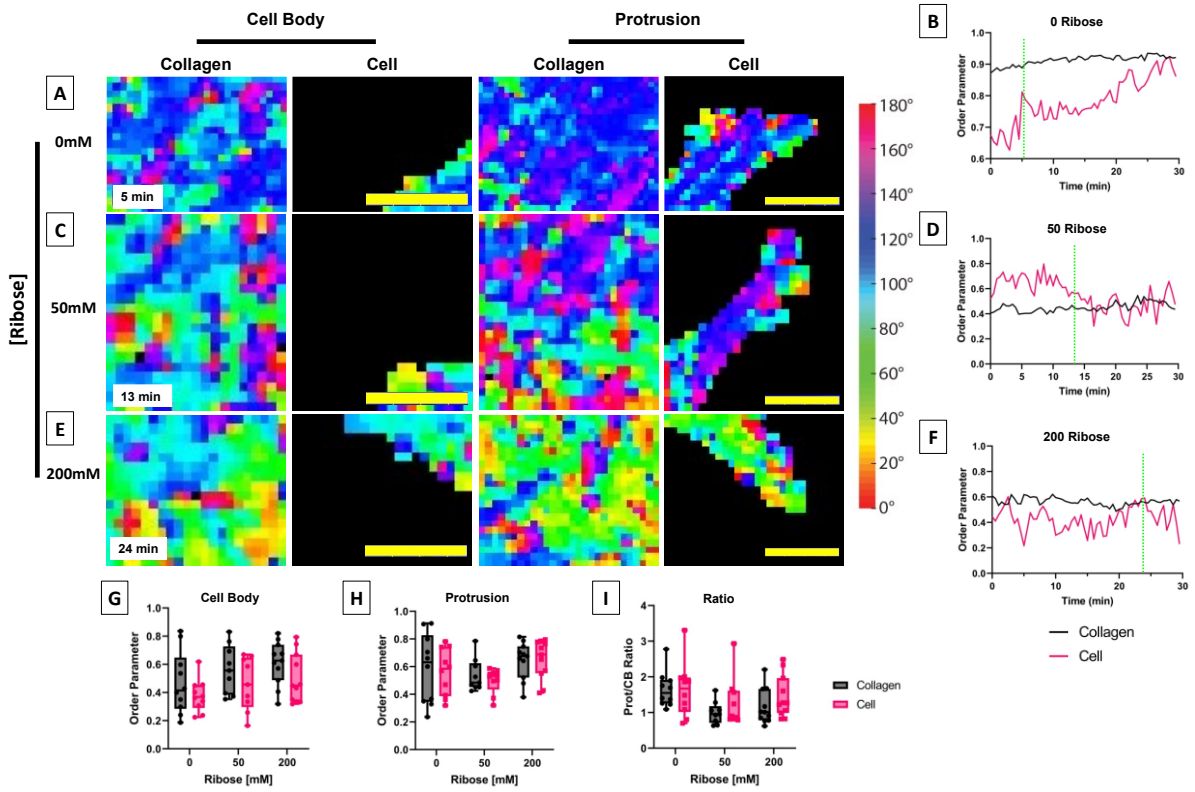

Figure 5.6 – Alignment of F-actin and adjacent collagen fibres show high heterogeneity over time

A) Representative images of MIP through Z, 2D AFT angle heatmap of collagen and corresponding cell filamentous structures imaged at 30-second TR for 30 min across 0-mM, **C)** 50-mM and **E)** 200-mM collagen-ribose matrices. Dynamics of collagen and cell order parameter at **B)** 0-mM, **D)** 50-mM and **F)** 200-mM with displayed images marked at green dotted line. **G)** Quantification of filamentous order parameter in collagen and protrusion and **H)** protrusion to cell body ratio across 0-, 50- and 200-mM collagen ribose matrices. Graph representing 10 measurements across 3 experimental repeats. All scale bars represent 20 μm. Error bars represent min to max, box-and-whiskers containing 25th/75th percentile and the median line. Asterisks indicate statistical significance via two-way ANOVA test.

5.3 Discussion

5.3.1 Protrusion adhesion and retraction dynamics are the main driving force for collagen remodelling and single cell migration

The importance of bidirectional interplay between cells and the surrounding matrix is now well accepted across many different biological settings (van Helvert, Storm, and Friedl 2017). Cells are both directly influenced by, and exert influence upon, the ECM through actomyosin based contractility, with stiffer substrates enabling increases in integrin, focal adhesion, and myosin II contractility (Doss et al. 2020; Doyle et al. 2021; Peng et al. 2022). Leading edges of some solid tumours exhibit aligned collagen fibres that provide highways for collective and single-cell migration of cells away from the tumour core. Leading invasive cells can also remodel the ECM to create paths for following cells to more easily migrate and disseminate. For example, breast cancers increase alignment of collagen fibres adjacent to the tumour and this correlated with poor patient prognosis (Conklin et al. 2011), however the underlying spatiotemporal mechanisms and contributions from different cell types within the tumour microenvironment to this phenomenon remain poorly understood (Pakshir et al. 2019; Su et al. 2021). Recent studies of cells in 3D scaffolds support the notion that sensing of ECM network topography and tension play a key role in directional cell migration (Han et al. 2018). Using enhanced resolution and reduced phototoxicity afforded by instruments such as the LLSM enables detailed analysis of protrusion dynamics in 4D and provides additional insight into how changes in F-actin dynamics can influence matrix remodelling.

Data in this chapter demonstrated that the stiffness of the matrices did not affect protrusion morphology, consistent with findings of the previous chapter (**Figure 5.2.1**). However, lower stiffness matrices induce higher rates of protrusion retraction (**Figure 5.2.2G**) and equal speeds of actin protrusion dynamics (**Figure 5.2.4G**) to induce the same degree of collagen displacement (**Figure 5.2.5G**). We hypothesised the same tractional force imposed by the protrusion is disseminated over a larger area of softer collagen networks. It is likely that the higher flexibility of the softer 3D collagen gels requires a higher degree of cell membrane retraction to achieve similar levels of stiffness required to induce migration. This could also alter the density of

collagen surrounding the cell, providing more binding sites for cell-ECM interactions, leading to a feedback mechanism and the increased retraction observed under these conditions. The reduced malleability of high stiffness matrices (200-mM) may conversely offer more structural integrity for protrusions to adhere to and impose tractional forces on. This indicates that the same degree of tractional force imposed by protrusions on the surrounding matrix in these stiffer environments instead results in more localised collagen displacement immediately adjacent to the cell. Reducing the level of collagen contraction toward the cell may also diminish the number of available integrin binding sites, consequently reducing the degree to which the protrusion retracts (**Figure 5.2.2G**).

Intriguingly, cells in 50-mM collagen-ribose matrices showed the same degree of membrane extension and retraction as higher stiffness matrices but significantly higher speeds of collagen displacement relative to the cell body (**Figure 5.2.H**). Coupled with higher centroid shifts measured from whole cell movements at 1-hour (**Figure 4.2.4**), this would confirm that matrices of middling stiffness offer a greater ability to mobilise F-actin within protrusions compared to those in 200-mM matrices but require a reduced degree of remodelling than those in 0-mM gels to achieve the stability necessary for single cell migration.

Protrusions play a crucial role in single cell migration as they simultaneously explore, remodel, and pull the cell through the matrix. Operating at twice the membrane speed, whilst maintaining the same degree of extension and retraction as the cell body (**Figure 5.2.3**) it is an optimised process for efficient collagen remodelling and single cell migration. The heterogeneity of collagen alignment surrounding protrusions seen in cells 24-hours post-embedding in 0-, 50- and 200-mM collagen-ribose gels (**Figure 5.2.6**) making it difficult to draw conclusions around short or longer-term co-ordination of F-actin and collagen alignment. More detailed analysis of single cells between 1- and 24-hours post-embedding would be interesting to perform in future to measure the initial stages of remodelling in matrices of differing stiffnesses. In order to capture the full scope of single cell activity, ranges in TR and scale are required to ascertain the finer dynamics of F-actin structures such as

filopodia and the degree of influence imposed by the cell on the surrounding matrix. This would enable the quantification of evolution of directional migration and speed of ECM remodelling over time. The techniques established here to capture cell and matrix dynamics in 3D at high resolution will enable more refined dissecting of the sequence of events in cell-ECM mechanotransduction in future.

5.3.2 Increased availability, efficiency and speed of 3D analysis programs required for the future of localisation dynamics.

The data from this chapter demonstrated successful imaging of single F-actin protrusions in HeLa cells simultaneous with adjacent Alexa647-SE labelled collagen. A maximum TR of 30-seconds was achievable for these images when capturing the full volume of the protrusions. As shown in **Figure 4.7** from the previous chapter, the higher the TR achieved, the closer to capturing and quantifying the dynamics of single cell protrusion activity in 3D collagen-ribose matrices are in real time (Henderson, Rutt, and Lee 1998). Reducing the volume imaged in future experiments would allow to further increase the TR and capture dynamics of finer structures seen in protrusions, such as filopodia.

As in the previous chapter, captured 3D image series were too memory intense to analyse using the developed program for 3D cross-correlation as performed by the analysis workstation with a Intel(R) Core(TM) i9-9960X CPU @ 3.10GHz, 3096 Mhz, 16 Core(s), 32 Logical Processor(s) and Installed Physical Memory (RAM) of 64.0 GB. The data in this chapter was therefore analysed using MIP images of 3D time-lapses of protrusions and the surrounding matrix in order to be comparable. These results may offer indications of protrusion activity, displayed in the comparative results of 2D vs 3D cross-correlation analysis, in **Figure 4.9D** and **E,** but may not reflect the true 3D dynamics of the structures analysed. Better methods of 3D analysis are required to be able to visualise, understand and quantify the localisation of the cell and surrounding matrix dynamics in a 3D space and minimise the loss of data ever-expanding image sets following the evolution of live cell microscopy techniques (Comes et al. 2019; Gibbs et al. 2021).

6 Discussion

6.1 Advances in live cell microscopy enable greater scale, spatial and temporal resolution of dynamics in single cells

In this thesis, two fluorescence microscopy techniques, iSIM and LLSM, were used to imaged HeLa lifeact-mScarlet cells in Alexa647-SE labelled collagen-ribose matrixes. The high illumination powers required to penetrate samples, image at depth, and repeatedly scan across living samples, mean most fluorescent live cell imaging in 3D can be highly phototoxic. Compared to the most standard fluorescence microscopy techniques, such as CLSM, both the iSIM and LLSM accelerate acquisition times and reduce phototoxicity. These techniques both had significant advantages and disadvantages.

The iSIM captured a significantly larger volume than LLSM (Figure 3.2.6) and offered the same resolution in X-Y, however, the Z-distance between planes was larger to reduce phototoxicity, thus limiting the Z resolution. Using LLSM, the Z-resolution was twice that of the iSIM but imaging was only possible within a smaller volume (**Figure 3.7**). Some techniques offer improved resolution at the expense of much slower imaging speeds and much higher photon doses, which can result in increased photobleaching and phototoxicity (Tinevez et al. 2012).

iSIM constantly illuminates the entire sample during acquisition, leading to elevated levels of photobleaching, increasing with every time point imaged in 3D (**Figure 4.3**). By illuminating only the plane of focus, the LLSM minimises the degree of bleaching to the sample, while other technical improvements enable acceleration of the acquisition of colour channels across three-dimensional stacks. However, higher TR leads to reduced recovery time despite the LLSM causing less photobleaching per Z-stack than the iSIM (**Figure 4.3**). All of these microscopy parameters must be carefully balanced in order to acquire 3D live cells in collagen matrices at the desired scale, structure, and dynamics, as they impact on ROS production which results in changes to cell viability (Stephens and Allan 2003; X. Wang et al. 2013) and also on the analysis of 3D structures (Comes et al. 2019).

As a result of advances in 3D live-cell microscopy, other issues such as computing hardware, image software, and analysis methods, have become the limiting factor, rather than the data acquisition. The large data files associated with live cell imaging are not yet universally accessible, easy to use, or efficient to manage. The 3D cross-correlation analysis used in this PhD resulted in significantly higher changes to the magnitudes of biological processes measured and differences between stiffnesses, compared to analysis performed on 2D MIP images (**Figure 4.9**). Although a more detailed analysis of 3D structures was achieved, the amount of computational time required to analyse 13 3D timepoints from the iSIM, took days-weeks, as opposed to minutes for 2D MIP images. This analysis was run on a Microsoft Windows 10 Enterprise, Precision 5820 Tower X-Series x-64 based PC with a Intel(R) Core(TM) i9-9960X CPU @ 3.10GHz, 3096 Mhz 16 Core(s), 32 Logical Processor(s) and installed physical memory (RAM) of 64.0 GB. The size (200 Z-slices) and number of 3D timepoints (61) in the LLSM data sets made it impossible to analyse them within the timeframe of this thesis. Future developments allowing for the rapid, efficient, and detailed visualisation and analysis of the dynamics imaged, would offer a much more comprehensive reflection of the true events occurring in 3D.

As a result of increased memory capacity and RAM requirements to store, transfer and process raw microscopy data before analysis, 3D live-cell imaging data sets are much more challenging to manage compared to 2D data. The speed of dynamic protrusions measured here was significantly different when subsampled at 30-second vs. 10-minutes TR (**Figure 4.7**) and dynamic details are lost at lower TRs. For better interpretation of 3D microscopy data, acquisition parameters should be as consistent as possible, and the trade-off between all these different parameters carefully considered, as 3D data sets have increased variable parameters, including Z- and TR, to appropriately compare data sets.

6.2 A Reproducible method of single-cell migration fluorescence imaging for stiffness-dependent dynamics of the bidirectional relationship of the cell-ECM

Cell migration in 3D microenvironments is known to vary depending on the cell type and composition of the ECM. There are numerous and complex biochemical and biomechanical properties *in vivo* that govern cell-ECM interactions. Molecular composition, concentrations, topography, topology, degree of crosslinking, porosity, density, stiffness, elasticity, and degree of remodelling in the ECM all have an impact on cell behaviour, and vice versa. *In vitro* control of these factors and parameters allows for the isolation of their individual roles contributing to cell behaviour. In this PhD, *in vitro* 3D methods offered an advantage in changing the matrix stiffness independently of matrix density, while simultaneously capturing ECM dynamics with fluorescence microscopy.

The combination of AFM and iSIM enabled the successful characterization of stiffness and topography of 0-, 50-, and 200-mM ribose collagen matrices. The protocol established from Mason et al. 2013 was primarily validated using the AFM and showed the stiffness of matrices to increase with that of increasing ribose concentrations. Unlabelled polymerised matrices visualised using CNA35-EGFP post-polymerisation labelling, maintained consistent density, porosity, and topography across all ribose conditions. Matrices with the corresponding ribose-to-stiffness measurement from the AFM were quantified through volume fill analysis (**Figure 3.1**). Volume fill analysis enabled the rapid visual validation of ribose-to-stiffness matrices, removing the impracticality of performing corresponding AFM experiments with every sample. This became particularly important when incorporating cells into matrices. The inability of the AFM to clearly visualise the touchdown surface of thick collagen-ribose samples meant it would not be possible to guarantee measurements solely of the collagen and not the cell.

Methods used in fluorescent labelling of collagen before polymerisation showed either negative interference with polymerization of the matrix using CNA35-EGFP (**Figure 3.2**), or aberrations and inconsistencies in matrix organization using Cy3

mono-reactive dye (**Figure 3.3**) likely due to the long timescale of its preparation. Alexa647-SE provided the most compatible, consistent, reproducible, and cost-effective way to fluorescently label the matrix (**Figure 3.4**). The use of Alexa647-SE and lifeact-mScarlet significantly reduced levels of phototoxicity as a result of their wavelengths and quantum yield (Bindels et al. 2016). This proved to be important in minimising the impact of imaging in 3D, across both wavelengths and over time on live samples. Volume fill analysis was also performed on collagen matrix regions and validated the accuracy of the polymerisation and stiffness of the Alexa647-SE labelled collagen.

Collagen-ribose matrices labelled with Alexa647-SE showed equal degrees of alignment between neighbouring structures as those of unlabelled collagen matrices across all ribose conditions (**Figure 3.5**). Having successfully validated this method, we subsequently applied it to the analysis of the effects of increasing matrix stiffness on single HeLa lifeact-mScarlet cells. This methodology allows for the simultaneously capturing of fluorescently tagged single cells and surrounding fluorescently labelled matrix, reducing the need for other approaches such as SHG and enabling greater resolution and visualisation of the mechanisms in mechanotransduction at different stages of ECM remodelling.

6.3 Higher stiffness matrices induce greater initial cytoskeletal structures in single cells

In agreement with the literature, increased stiffness enabled more defined cytoskeletal F-actin structures to form (**Figure 3.7**). Previous studies have shown that increased stiffness increases integrin expression in 2D and on 3D substrates (Yeung et al. 2005). Through repetitive probing of its environment with integrins and focal adhesions, the cell tests the mechanoproperties of the ECM (Plotnikov et al. 2012). According to 3D models (Han et al. 2018), tension sensing is likely to play a critical role in cancer cell migration. Cell spreading and the degree of definition of F-actin structures are also considered as predictors of cell traction (Califano and Reinhart-King 2010). F-actin structures such as filopodia, lamellipodia, and pseudopodia were evident, and upregulated to varying degrees according to stiffness, in HeLa lifeact-mScarlet cells 1-hour after embedding in collagen gels.

Low stiffness collagen-ribose matrices (0-mM) reflected previous findings, showing less developed structures of the cytoskeleton (**Figure 3.7**), and displaying higher turnover of these structures when imaged over time (**Figure 4.1** and **Figure 4.4**). With higher stiffness matrices (50- and 200-mM) actin structures extended further into the surrounding matrix with more defined stress-fibres, potential adhesion points (**Figure 3.7**) and reduced overall change to cell morphology (**Figure 4.4**). Compared to cells embedded in 0-mM, cells in high stiffness collagen-ribose matrices, correlating with increased defined F-actin structures, imposed significantly greater tractional forces and displacements on the matrix (**Figure 4.8**).

The velocity of cell membranes did not change across ribose conditions, but single cells exhibited a higher rate of membrane retraction vs protrusion across all ribose conditions (**Figure 4.5**). The higher rate of membrane retraction, combined with the degree of matrix remodelling (**Figure 4.8**), indicates opposite effects to membrane dynamics. The malleable nature of 0-mM ribose matrices causes retraction due to the lack of support for the cytoskeleton to stabilise leading to increased turnover. The actin assemblies in cells in 200-mM ribose collagen gels (**Figure 4.1**) and greater displacement of collagen (**Figure 4.8**) indicate tractional force for matrix remodelling,

but this is coupled with reduced migration (**Figure 4.4**). The strong adhesion and contraction of the cell in an undirected fashion are likely to be the reason for this reduced cell movement. Interestingly, cells in 50-mM ribose collagen gels showed reduced retraction (**Figure 4.5**), but a larger centroid shift (**Figure 4.4**) and substantial displacement of the collagen matrix (**Figure 4.8**). This suggests that matrices of medium stiffness offer the greatest potential for remodelling and simultaneous structural support for single cell migration. Cells did not show any clear directional polarity one hour after embedding, whereas by 24 hours all cells formed highly directional pseudopodium (**Figure 3.8**). Using combined iSIM and LLSM datasets, a more detailed timeline across 24-hours at different scales and TRs should be used to establish the mechanisms and feedback systems used by single cells in nascent ECM to adapt and manipulate new matrix to achieve the directional migration phenotype seen at 24-hours independent of stiffness.

6.4 Single cells adapt their cytoskeletal dynamics across stiffnesses to maintain consistent degrees of mobility and remodelling at 24-hours

Cells exhibit differences in migration depending on the elasticity and viscoelastic properties of the matrix (Chaudhuri et al. 2020), regulating genome architecture (Shivashankar 2019) and malignancy with increased matrix stiffness (Stowers et al. 2019). Matrices are viscoelastic, displaying combinations of the viscosity of a thick fluid and elasticity that attempts to return the material to its original form or organization after a deforming force is released. This combination of properties results in plastic deformation of the ECM in response to cell tractional forces, often without returning to its original form (Adebowale et al. 2021; Hui et al. 2021). The studies performed in this thesis should ideally be complemented with further analysis of the impact on the viscoelastic properties of the matrix during ECM remodelling and cell migration.

Observations of single cells imaged at 24-hours, showed an adapted more directional migratory morphology better suited for navigating the matrix, regardless of matrix stiffness, compared to cells immediately after seeding (**Figure 3.8**). These features are distinct from those seen in 2D, reflecting more the properties of mesenchymal cell migration in 3D (Doyle et al. 2021). A further indication of this is the decreased surface area to volume ratio after 24-hours, regardless of stiffness (**Figure 3.9**). Since there were limitations to the volume capacity of the LLSM, the capturing of smaller cells (**Figure 3.9**) offered greater compatibility in navigating the porosity and density of matrices at 2mg/ml of collagen, with studies of varying substrate confinement impacting cytoskeletal organisation, cell-substrate adhesion, intracellular signalling, gene expression and nuclear shape (van Helvert, Storm, and Friedl 2017). Future studies should include the acquisition of single cells of a larger volume, as was performed here with the iSIM, to establish the role cell size and matrix porosity plays on cell dynamics, ECM remodelling and migration.

The dynamics of single cells at 24-hours through matrices of different stiffnesses are highly complementary to previous studies showing the orientation of matrix remodelling being highly aligned to the direction of mechanical forces imposed by

cells (Pang et al. 2011). AFT analysis performed on collagen-ribose matrices at 24-hours showed a significantly higher alignment between neighbouring structures imposed by the cell over time compared to 1h post-embedding (**Figure 3.10**). This increased re-organisation of the matrix and consistent speed of centroid shift across ribose concentrations (**Figure 4.4**) after 24-hours shows the cell increases the ability to remodel the matrix in order to maintain migration speed. For the same degree of mobilisation, single cells in 0- and 50-mM collagen ribose matrices required a significantly higher level of membrane retraction (**Figure 4.6**) and significantly higher displacement of the matrix (**Figure 4.9**). Softer matrices therefore are better mobilised by tractional forces of the cell to enable the tautness of remodelling to be significant enough to support single cell migration. For future studies, capturing a more detailed timeline of the temporal rate, distance, and degree in which single cells remodel nascent ECM, would significantly help establish the mechano-reciprocity of the cell and ECM on one another.

6.5 Leading protrusions dynamics account for the upregulated remodelling of the ECM

The bidirectional interplay between cells and the components of 3D matrices is important in governing cell behaviour. Single cell protrusions imaged at high TR offered an important development in the dissection of mechanisms in used for matrix remodelling. Membrane protrusions are known to play an essential role in single cell migration, simultaneously exploring, applying tractional force, and optimising its mobilisation through the surrounding features of the matrix in 3D. 3D ECM alignment promotes the persistence, elongation, and adhesion of protrusions along the alignment axis through FAK and Rac1 signalling (Carey et al. 2016; Doyle et al. 2015). Delineating the dynamics of protrusion and their functional significance in greater resolution and TR relative to ECM topography will help further establish their physiological role in mechanotransduction.

The high 3D spatial and TR of the LLSM allowed quantification of protrusion dynamics at 24-hours (**Figure 5.1**) which was not possible with the lower TR iSIM data. Protrusion dynamics were twice the speed of those measured from the cell body (**Figure 5.3**) through a heterogeneously organised ECM (**Figure 5.6**). The high dynamics measured in leading protrusions to maintain consistent motility through the matrix (**Figure 4.4**), despite difference in stiffness, indicates these as key feedback mechanisms in migration.

F-actin within protrusions mobilising through or along collagen fibres can expose integrins to ECM ligands. Higher ECM density in 2D leads to increased cell retraction by increasing actin flow rate, adhesion turnover and adhesion lifetime (Gupton and Waterman-Storer 2006). Higher rates of membrane retraction (**Figure 5.2**) in lower stiffness matrices, with equal intracellular actin dynamics (**Figure 5.4**) and collagen displacement (**Figure 5.5**), suggests a positive feedback loop of increased adhesion and retraction due to the increased quantity of mobilised matrix near the cell exposing greater numbers of binding sites. Matrices of higher stiffness showed more local displacement of collagen fibres likely due to its higher structural support (**Figure 5.5**). This may reduce the number of ECM binding sites presented to the

protrusion and therefore its degree of membrane retraction (**Figure 5.3 & 5.4**). A more accurate analysis in 3D of the protrusion and matrix localisation of dynamics captured, would offer even greater insight into the adhesive, contractile and migratory sequence of events seen in matrices of varying stiffness.

Altogether, these experiments highlight the importance of the chronology of events in single cell migration relative to the topography of the surrounding matrix. Depending on the stage of the single cell, the changes in the mechanical properties of its microenvironment can differentially influence its dynamics. Using this model of chronology of single cells remodelling and migration through the ECM, of further mechanisms, pathways and possible therapeutics could be visualised and tested at different resolutions, TR, and timescales.

6.6 Future directions

Most studies to date have been performed on 2D surfaces of non-physiological high stiffnesses to identify the specific temporal and spatial steps involved with cell motility. The progression seen in cell culture methods on 3D surfaces of varying composition, density, and elasticity, have been shown to impact integrin expression and cell contractility. Cells respond to stiffer matrices through altered actomyosin contractility by matching their microenvironment to migrate up stiffness gradients (DuChez et al. 2019; Lo et al. 2000). Increased density of substrate leads to the increase of cell retraction through adhesion turnover lifetime and actin flow rates (Gupton and Waterman-Storer 2006) highlighting the external factors importance in influencing cell migration.

The increased number of parameters altering intracellular mechanisms in cell migration when expanded into the 3D microenvironment has more accurately reflected physiological conditions. 3D methods have shown increased matrix concentrations to decrease matrix pore size to a point of inhibiting cell migration due to the limiting size of the nucleus (Lämmermann et al. 2008; Renkawitz et al. 2019; Wolf et al. 2013). To better study the effect porosity plays in single cell migration, it would be important to repeat these analyses to quantify the impact of pore size and cell volume on the dynamics of migration, nuclear chromatin compaction coupled with protrusion long term invasion or changes in matrix concentration.

Non-linear elastic matrices showed the potential to undergo strain stiffening through a two-fold increase in contractile strain from the leading protrusion end, altering cell rates of migration (Doyle et al. 2021a) whereas increased alignment enhanced migration rates of cells (Riching et al. 2014; Taufalele et al. 2019). Alignment of the ECM was shown to be strongly induced after 24-hours by single cells, greater imaging of the matrix topography between 1- and 24-hours would offer a greater information on the remodelling mechanism used by cells in matrices of different stiffnesses.

Key to 3D migration is the cellular characteristics, such as the adhesiveness mediated through integrins, (Kechagia, Ivaska, and Roca-Cusachs 2019; Paul, Jacquemet, and Caswell 2015), leading edge protrusion type (Petrie et al. 2012) and actomyosin contractility (Kubow, Conrad, and Horwitz 2013) all impacting the architecture of the ECM. Further expanding of this 3D single cell model to capture the dynamics of other proteins involved in adhesion, such as FAK, vinculin, talin and tensin, cytoskeletal contractility, such as myosin II and other mechanotransduction proteins would be useful step towards a greater comprehensive understanding of events in matrix remodelling and single cell migration of different kinds. Blocking specific integrins and analysing integrin trafficking would help further dissect the specific role they play in mechanotransduction within 3D matrices. Utilising methods of FRET-based efficiency tension sensors to measure the forces across individual molecules in cells would allow for the accurate quantification of changes in molecular tension during mechanotransduction (Cost, Khalaji, and Grashoff 2019). Flipper probes, through changes in its fluorescent lifetime, would enable the quantification of membrane tension and see of any correlation with protrusion, actin dynamics and ECM remodelling (Dal Molin et al. 2015).

Laser ablation techniques in mechanosensitive adhesion studies have emphasised the variations seen in contractility applied with cell specific types of migration (Doyle et al. 2012, 2021). The differences in the migration cycles of different cell types highlight the importance of verifying cell type specificity in 3D conditions. Many pathways and proteins associated with mechanotransduction, such as Src and FAK, have been investigated as possible therapeutic targets to reduce the invasiveness of cancers (Carter et al. 2017; Lamar et al. 2019). Filopodia-associated genes are upregulated in breast carcinomas with a poor prognosis (Baumbusch et al. 2008). ROCK inhibition has shown clinically to inhibit melanoma cancer cell growth, invasion, and metastasis with multiple trials ongoing (Lee et al. 2019). Applying techniques in matrix ablation, the inhibition of known pathways and knockout/knockdown of genes associated with migration and increased aggressiveness of cancer, would enable better correlation of the role matrix topography, tension and stiffness plays in the invasiveness of cancer associated cells at different timepoints in migration.

Some targeted mechanisms have proved to induce little to no effect on the tumour and accompanied by severe side effects, such as the use of MMP inhibitors (Winer, Adams, and Mignatti 2018). Inhibition or knockout of YAP/TAZ can attenuate fibrosis in organs such as lung, liver, and kidney (He et al. 2022). Mechanistically, YAP/TAZ activation can induce a profibrotic response in fibroblasts, thereby generating more traction, depositing more collagen, and is implicated in breast cancer metastasis (Kim, Jung, and Koo 2015). By further dissecting their dynamics and subtilties in regard to the ECM, a more specific and targeted method of treatment therapy could be found in reducing the invasiveness of tumours. The methodology used in this thesis would enable a rapid and efficient method to visualise and test the impact stiffness coupled with therapeutic targeted drug screenings have on single cells and their dynamics.

Many in vivo studies have shown the specific effects of secondary cell types, such as CAFs and tumour-associated immune cells, to be essential in cancer cell invasion through increased degrees of collagen cross-linking (Maller et al. 2021) and upregulated positive feedback loops further driving metastasis (Mantovani et al. 2017). Exploring the relationship between homogenous and heterogenous cell populations of different cell-ECM compatibility, reflecting pairings known in tumour sites, is important to study to better recapitulate the tumour microenvironment. Expanding the current methods described to include heterogenous cell populations at varying concentrations up to more complex organoid in vitro methods in matrices of different stiffnesses would offer greater understanding in the physiological relationship of tumour sites and the pathways altered for increased ECM remodelling and metastasis.

The multiple ways in which cells are found to migrate in vivo, from single to collective cell migration (Krakhmal et al. 2015) effect the pathways and mechanisms activated in cells. Variations in pressure (Sarntinoranont, Rooney, and Ferrari 2003), stiffness (Mason et al. 2012)and degree of remodelling (Ray et al. 2017) imposed on the surrounding matrix and also in cell-cell interactions. The temporal role of matrix

stiffness has been implicated in the initiation of invasion in spheroid models (Staneva et al. 2018). A more detailed analysis of ECM localised stiffening and remodelling should be explored further, in spheroid-based models of 3D invasion and single cells.

Investigations into methods of personalised cancer therapies through histopathology, cell lineage, DNA and RNA analysis and the development of cell cultures from tumour biopsies to establish higher efficiency models have become more attractive in recent years. This enables the quantification of cancer cell response to targeted therapies in mixed cell cultures (Kodack et al. 2017; Miller et al. 2005; Smirnov et al. 2005). Our method would allow for mixed cell cultures in 3D to be visualised and quantified easily in response to stiffness and topography, offering insight into the specific characteristics of biopsied samples.

An increase in the use of computational models closely integrated with experimental support, have provided some quantitative assessments, and been used as predictive tools in further dissecting the reciprocal relationship of the cell-ECM. Through these computational methods they have successfully demonstrated a variety of extra- and intracellular mechanisms reflected in experimental data such as: stochastic variability of protrusion lifetimes impact on cell migration velocity; the optimal number of simultaneous protrusions to be one or two in single cell migration but variable with ECM anisotropy; and increased actin nucleation through epidermal growth factor leads to altered intracellular stiffness and power output (Heck et al. 2020; Spill, Bakal, and Mak 2018b). Through the combine fluorescence imaging and cell culturing methods of this thesis, greater ranges of scale and resolution, of both the cell and matrix, could be used for greater modelling of the dynamics of single cells at different stiffnesses and with varying degrees of structural alignment.

The techniques used and developed in this thesis helped explore the dynamics single cells use as a response to the surroundings matrix stiffness and topography. This holds the potential to capture, in a highly detailed way and explore in greater depths, the different time points (ranging from 1-hour to days), scales (from single

cell to protrusion), components of the cytoskeleton (from actin to focal adhesion) and TR (seconds to hours) of the dynamics of single cells and surrounding ECM in 3D.

7 Reference List

Abatangelo, G. et al. 2020. “Hyaluronic Acid: Redefining Its Role.” *Cells* 9(7): 1–19. https://pubmed.ncbi.nlm.nih.gov/32708202/ (November 21, 2022).

Adebowale, Kolade et al. 2021. “Enhanced Substrate Stress Relaxation Promotes Filopodia-Mediated Cell Migration.” *Nature Materials 2021 20:9* 20(9): 1290–99. https://www.nature.com/articles/s41563-021-00981-w (December 20, 2022).

Aper, Stijn J.A. et al. 2014. “Colorful Protein-Based Fluorescent Probes for Collagen Imaging.” *PLoS ONE* 9(12). /pmc/articles/PMC4260915/ (August 22, 2022).

Aper, Stijn J.A. A. et al. 2014. “Colorful Protein-Based Fluorescent Probes for Collagen Imaging” ed. Ahmad Waseem. *PLoS ONE* 9(12): 1–21. http://www.ncbi.nlm.nih.gov/pubmed/25490719 (February 20, 2019).

Arjonen, Antti, Riina Kaukonen, and Johanna Ivaska. 2011. “Filopodia and Adhesion in Cancer Cell Motility.” *Cell Adhesion & Migration* 5(5): 421. /pmc/articles/PMC3218609/ (December 14, 2022).

Aumailley, Monique. 2013. “The Laminin Family.” *Cell Adhesion & Migration* 7(1): 48–55. https://www.tandfonline.com/action/journalInformation?journalCode=kcam20 (December 4, 2022).

Bachmann, Michael, Sampo Kukkurainen, Vesa P. Hytönen, and Bernhard Wehrle-Haller. 2019. “Cell Adhesion by Integrins.” *Physiological reviews* 99(4): 1655–99. https://pubmed.ncbi.nlm.nih.gov/31313981/ (December 4, 2022).

Barry, David J., Charlotte H. Durkin, Jasmine v. Abella, and Michael Way. 2015. “Open Source Software for Quantification of Cell Migration, Protrusions, and Fluorescence Intensities.” *Journal of Cell Biology* 209(1): 163–80. www.jcb.org/cgi/doi/10.1083/jcb.201501081JCB163 (October 24, 2022).

Baumbusch, Lars O. et al. 2008. “Comparison of the Agilent, ROMA/NimbleGen and Illumina Platforms for Classification of Copy Number Alterations in Human Breast Tumors.” *BMC genomics* 9. https://pubmed.ncbi.nlm.nih.gov/18691401/ (December 21, 2022).

Berrier, Allison L., and Kenneth M. Yamada. 2007. “Cell-Matrix Adhesion.” *Journal of Cellular Physiology* 213(3): 565–73.

Bindels, Daphne S et al. 2016. “MScarlet: A Bright Monomeric Red Fluorescent Protein for Cellular Imaging.” *Nature Publishing Group* 14. http://www.microscopist.co.uk/wp-content/uploads/2018/05/mScarlet.pdf (January 8, 2019).

Bonnans, Caroline, Jonathan Chou, and Zena Werb. 2014. “Remodelling the Extracellular Matrix in Development and Disease.” *Nature reviews. Molecular cell biology* 15(12): 786–801. https://pubmed.ncbi.nlm.nih.gov/25415508/ (November 19, 2022).

Breitsprecher, Dennis et al. 2011. “Molecular Mechanism of Ena/VASP-Mediated Actin-Filament Elongation.” *The EMBO Journal* 30(3): 456. /pmc/articles/PMC3034019/ (December 29, 2022).

Brodsky, Barbara, and Anton v. Persikov. 2005. “Molecular Structure of the Collagen Triple Helix.” *Advances in Protein Chemistry* 70: 301–39.

Burdick, Jason A., and Kristi S. Anseth. 2002. “Photoencapsulation of Osteoblasts in Injectable RGD-Modified PEG Hydrogels for Bone Tissue Engineering.” *Biomaterials* 23(22): 4315–23. https://pubmed.ncbi.nlm.nih.gov/12219821/ (November 27, 2022).

Burridge, Keith, and Krister Wennerberg. 2004. “Rho and Rac Take Center Stage.” *Cell* 116(2): 167–79. https://pubmed.ncbi.nlm.nih.gov/14744429/ (December 17, 2022).

Calderwood, David A. 2004. “Integrin Activation.” *Journal of cell science* 117(Pt 5): 657–66. https://pubmed.ncbi.nlm.nih.gov/14754902/ (December 29, 2022).

Califano, Joseph P., and Cynthia A. Reinhart-King. 2010a. “Substrate Stiffness and Cell Area Predict Cellular Traction Stresses in Single Cells and Cells in Contact.” *Cellular and molecular bioengineering* 3(1): 68–75. https://pubmed.ncbi.nlm.nih.gov/21116436/ (September 5, 2022).

———. 2010b. “Substrate Stiffness and Cell Area Predict Cellular Traction Stresses in Single Cells and Cells in Contact.” *Cellular and Molecular Bioengineering* 3(1): 68–75. https://link.springer.com/article/10.1007/s12195-010-0102-6 (December 29, 2022).

Camenisch, Todd D. et al. 2000. “Disruption of Hyaluronan Synthase-2 Abrogates Normal Cardiac Morphogenesis and Hyaluronan-Mediated Transformation of Epithelium to Mesenchyme.” *The Journal of clinical investigation* 106(3): 349–60. https://pubmed.ncbi.nlm.nih.gov/10930438/ (November 21, 2022).

Campagnola, Paul J. et al. 2002. “Three-Dimensional High-Resolution Second-Harmonic Generation Imaging of Endogenous Structural Proteins in Biological Tissues.” *Biophysical journal* 82(1 Pt 1): 493–508. https://pubmed.ncbi.nlm.nih.gov/11751336/ (August 22, 2022).

Carey, Shawn P. et al. 2016. “Local Extracellular Matrix Alignment Directs Cellular Protrusion Dynamics and Migration through Rac1 and FAK.” *Integrative Biology* 8(8): 821–35. https://academic.oup.com/ib/article/8/8/821/5163761 (December 22, 2022).

Carter, Bing Z. et al. 2017. “Focal Adhesion Kinase as a Potential Target in AML and MDS.” *Molecular cancer therapeutics* 16(6): 1133–44. https://pubmed.ncbi.nlm.nih.gov/28270436/ (December 21, 2022).

Chaudhuri, Ovijit et al. 2020. “Effects of Extracellular Matrix Viscoelasticity on Cellular Behaviour.” *Nature 2020 584:7822* 584(7822): 535–46. https://www.nature.com/articles/s41586-020-2612-2 (December 20, 2022).

Chauhan, Vikash P. et al. 2014. “Compression of Pancreatic Tumor Blood Vessels by Hyaluronan Is Caused by Solid Stress and Not Interstitial Fluid Pressure.” *Cancer cell* 26(1): 14–15. https://pubmed.ncbi.nlm.nih.gov/25026209/ (November 26, 2022).

Chen, Bi Chang et al. 2014a. “Lattice Light Sheet Microscopy: Imaging Molecules to Embryos at High Spatiotemporal Resolution.” *Science (New York, N.Y.)* 346(6208): 1257998. /pmc/articles/PMC4336192/ (August 22, 2022).

———. 2014b. “Lattice Light-Sheet Microscopy: Imaging Molecules to Embryos at High Spatiotemporal Resolution.” *Science* 346(6208). https://www.science.org/doi/10.1126/science.1257998 (August 23, 2022).

———. 2014c. “Lattice Light-Sheet Microscopy: Imaging Molecules to Embryos at High Spatiotemporal Resolution.” *Science (New York, N.Y.)* 346(6208). https://pubmed.ncbi.nlm.nih.gov/25342811/ (August 2, 2022).

Cheng, Gang, Janet Tse, Rakesh K. Jain, and Lance L. Munn. 2009. “Micro-Environmental Mechanical Stress Controls Tumor Spheroid Size and Morphology by Suppressing Proliferation and Inducing Apoptosis in Cancer Cells.” *PloS one* 4(2). https://pubmed.ncbi.nlm.nih.gov/19247489/ (November 26, 2022).

Colombelli, Julien et al. 2009. “Mechanosensing in Actin Stress Fibers Revealed by a Close Correlation between Force and Protein Localization.” *Journal of cell science* 122(Pt 10): 1665–79. https://pubmed.ncbi.nlm.nih.gov/19401336/ (December 5, 2022).

Comes, M. C. et al. 2019. “The Influence of Spatial and Temporal Resolutions on the Analysis of Cell-Cell Interaction: A Systematic Study for Time-Lapse Microscopy Applications.” *Scientific Reports 2019 9:1* 9(1): 1–11. https://www.nature.com/articles/s41598-019-42475-5 (November 2, 2022).

Conchello, José Angel, and Jeff W. Lichtman. 2005. “Optical Sectioning Microscopy.” *Nature Methods 2005 2:12* 2(12): 920–31. https://www.nature.com/articles/nmeth815 (October 18, 2022).

Conklin, Matthew W. et al. 2011a. “Aligned Collagen Is a Prognostic Signature for Survival in Human Breast Carcinoma.” *The American journal of pathology* 178(3): 1221–32. https://pubmed.ncbi.nlm.nih.gov/21356373/ (November 25, 2022).

———. 2011b. “Aligned Collagen Is a Prognostic Signature for Survival in Human Breast Carcinoma.” *The American Journal of Pathology* 178(3): 1221–32.

Cost, Anna Lena, Samira Khalaji, and Carsten Grashoff. 2019. “Genetically Encoded FRET-Based Tension Sensors.” *Current protocols in cell biology* 83(1). https://pubmed.ncbi.nlm.nih.gov/30865383/ (December 29, 2022).

Cox, Thomas R., and Janine T. Erler. 2011. “Remodeling and Homeostasis of the Extracellular Matrix: Implications for Fibrotic Diseases and Cancer.” *Disease models & mechanisms* 4(2): 165–78. https://pubmed.ncbi.nlm.nih.gov/21324931/ (November 19, 2022).

Critchley, David R., and Alexandre R. Gingras. 2008. “Talin at a Glance.” *Journal of cell science* 121(Pt 9): 1345–47. https://pubmed.ncbi.nlm.nih.gov/18434644/ (December 5, 2022).

Culbert, A. A. et al. 1995. “Substitutions of Aspartic Acid for Glycine-220 and of Arginine for Glycine-664 in the Triple Helix of the pro A1(I) Chain of Type I Procollagen Produce Lethal Osteogenesis Imperfecta and Disrupt the Ability of Collagen Fibrils to Incorporate Crystalline Hydroxyapatite.” *Biochemical Journal* 311(3): 815–20. /biochemj/article/311/3/815/32438/Substitutions-of-aspartic-acid-for-glycine-220-and (December 4, 2022).

Curd, Alistair et al. 2015a. “Construction of an Instant Structured Illumination Microscope.” *Methods (San Diego, Calif.)* 88: 37–47. https://pubmed.ncbi.nlm.nih.gov/26210400/ (November 18, 2022).

———. 2015b. “Construction of an Instant Structured Illumination Microscope.” *Methods (San Diego, Calif.)* 88: 37–47. https://pubmed.ncbi.nlm.nih.gov/26210400/ (August 23, 2022).

Dal Molin, Marta et al. 2015. “Fluorescent Flippers for Mechanosensitive Membrane Probes.” *Journal of the American Chemical Society* 137(2): 568–71. https://pubs.acs.org/doi/full/10.1021/ja5107018 (December 29, 2022).

Deryugina, Elena I., and James P. Quigley. 2006. “Matrix Metalloproteinases and Tumor Metastasis.” *Cancer metastasis reviews* 25(1): 9–34. https://pubmed.ncbi.nlm.nih.gov/16680569/ (November 26, 2022).

Dobner, Stephan, Ovid C. Amadi, and Richard T. Lee. 2012. “Cardiovascular Mechanotransduction.” *Muscle: Fundamental Biology and Mechanisms of Disease* 1–2: 173–86.

Domogatskaya, Anna, Sergey Rodin, and Karl Tryggvason. 2012. “Functional Diversity of Laminins.” *Annual review of cell and developmental biology* 28: 523–53. https://pubmed.ncbi.nlm.nih.gov/23057746/ (November 20, 2022).

Doss, Bryant L. et al. 2020. “Cell Response to Substrate Rigidity Is Regulated by Active and Passive Cytoskeletal Stress.” *Proceedings of the National Academy of Sciences of the United States of America* 117(23): 12817–25. https://www.pnas.org/doi/abs/10.1073/pnas.1917555117 (December 18, 2022).

Doyle, Andrew D. et al. 2012. “Micro-Environmental Control of Cell Migration - Myosin IIA Is Required for Efficient Migration in Fibrillar Environments through Control of Cell Adhesion Dynamics.” *Journal of Cell Science* 125(9): 2244–56. /pmc/articles/PMC3367941/ (December 21, 2022).

———. 2015a. “Local 3D Matrix Microenvironment Regulates Cell Migration through Spatiotemporal Dynamics of Contractility-Dependent Adhesions.” *Nature Communications 2015 6:1* 6(1): 1–15. https://www.nature.com/articles/ncomms9720 (December 18, 2022).

———. 2015b. “Local 3D Matrix Microenvironment Regulates Cell Migration through Spatiotemporal Dynamics of Contractility-Dependent Adhesions.” *Nature Communications* 6: 1–15. http://dx.doi.org/10.1038/ncomms9720.

———. 2018. “Fluorescent Labeling of Rat-Tail Collagen for 3D Fluorescence Imaging.” *Bio-protocol* 8(13). /pmc/articles/PMC6089535/ (August 23, 2022).

———. 2021a. “3D Mesenchymal Cell Migration Is Driven by Anterior Cellular Contraction That Generates an Extracellular Matrix Prestrain.” *Developmental Cell* 56(6): 826-841.e4.

———. 2021b. “3D Mesenchymal Cell Migration Is Driven by Anterior Cellular Contraction That Generates an Extracellular Matrix Prestrain.” *Developmental Cell* 56(6): 826-841.e4.

Doyle, Andrew D., Francis W. Wang, Kazue Matsumoto, and Kenneth M. Yamada. 2009. “One-Dimensional Topography Underlies Three-Dimensional Fibrillar Cell Migration.” *The Journal of cell biology* 184(4): 481–90. https://pubmed.ncbi.nlm.nih.gov/19221195/ (November 27, 2022).

Doyle, Andrew D., and Kenneth M. Yamada. 2016. “Mechanosensing via Cell-Matrix Adhesions in 3D Microenvironments.” *Experimental Cell Research* 343(1): 60–66. https://www.researchgate.net/publication/283455730_Mechanosensing_via_cell-matrix_adhesions_in_3D_microenvironments (November 23, 2022).

DuChez, Brian J., Andrew D. Doyle, Emilios K. Dimitriadis, and Kenneth M. Yamada. 2019. “Durotaxis by Human Cancer Cells.” *Biophysical Journal* 116(4): 670–83.

Dupont, Sirio. 2016. “Role of YAP/TAZ in Cell-Matrix Adhesion-Mediated Signalling and Mechanotransduction.” *Experimental cell research* 343(1): 42–53. https://pubmed.ncbi.nlm.nih.gov/26524510/ (November 22, 2022).

Egeblad, Mikala, Morten G. Rasch, and Valerie M. Weaver. 2010. “Dynamic Interplay between the Collagen Scaffold and Tumor Evolution.” *Current opinion in cell biology* 22(5): 697–706. https://pubmed.ncbi.nlm.nih.gov/20822891/ (November 21, 2022).

Egner, Alexander, Martin Schrader, and Stefan W. Hell. 1998. “Refractive Index Mismatch Induced Intensity and Phase Variations in Fluorescence Confocal, Multiphoton and 4Pi-Microscopy.” *Optics Communications* 153(4–6): 211–17.

Elfenbein, Arye, and Michael Simons. 2013. “Syndecan-4 Signaling at a Glance.” *Journal of cell science* 126(Pt 17): 3799–3804. https://pubmed.ncbi.nlm.nih.gov/23970415/ (November 23, 2022).

Elliott, Amicia D. 2020. “Confocal Microscopy: Principles and Modern Practices.” *Current Protocols in Cytometry* 92(1): e68. https://onlinelibrary.wiley.com/doi/full/10.1002/cpcy.68 (December 2, 2022).

Elosegui-Artola, Alberto et al. 2022. “Matrix Viscoelasticity Controls Spatio-Temporal Tissue Organization.” *bioRxiv*: 2022.01.19.476771. https://www.biorxiv.org/content/10.1101/2022.01.19.476771v1 (September 2, 2022).

Engler, Adam J. et al. 2004. “Myotubes Differentiate Optimally on Substrates with Tissue-like Stiffness: Pathological Implications for Soft or Stiff Microenvironments.” *The Journal of cell biology* 166(6): 877–87. https://pubmed.ncbi.nlm.nih.gov/15364962/ (December 17, 2022).

Etienne-Manneville, Sandrine. 2004. “Actin and Microtubules in Cell Motility: Which One Is in Control?” *Traffic (Copenhagen, Denmark)* 5(7): 470–77. https://pubmed.ncbi.nlm.nih.gov/15180824/ (November 23, 2022).

Ezratty, Ellen J., Claire Bertaux, Eugene E. Marcantonio, and Gregg G. Gundersen. 2009a. “Clathrin Mediates Integrin Endocytosis for Focal Adhesion Disassembly in Migrating Cells.” *The Journal of cell biology* 187(5): 733–47. https://pubmed.ncbi.nlm.nih.gov/19951918/ (December 5, 2022).

———. 2009b. “Clathrin Mediates Integrin Endocytosis for Focal Adhesion Disassembly in Migrating Cells.” *The Journal of cell biology* 187(5): 733–47. https://pubmed.ncbi.nlm.nih.gov/19951918/ (December 29, 2022).

Fang, Min, Jingping Yuan, Chunwei Peng, and Yan Li. 2014. “Collagen as a Double-Edged Sword in Tumor Progression.” *Tumour biology : the journal of the International Society for Oncodevelopmental Biology and Medicine* 35(4): 2871–82. https://pubmed.ncbi.nlm.nih.gov/24338768/ (November 26, 2022).

Fiolka, Reto et al. 2012. “Time-Lapse Two-Color 3D Imaging of Live Cells with Doubled Resolution Using Structured Illumination.” *Proceedings of the National Academy of Sciences of the United States of America* 109(14): 5311–15. https://www.pnas.org/doi/abs/10.1073/pnas.1119262109 (October 18, 2022).

Fletcher, Daniel A., and R. Dyche Mullins. 2010. “Cell Mechanics and the Cytoskeleton.” *Nature 2010 463:7280* 463(7280): 485–92. https://www.nature.com/articles/nature08908 (December 29, 2022).

Francis-Sedlak, Megan E. et al. 2009. “Characterization of Type I Collagen Gels Modified by Glycation.” *Biomaterials* 30(9): 1851–56. https://pubmed.ncbi.nlm.nih.gov/19111897/ (November 30, 2022).

Frantz, Christian, Kathleen M. Stewart, and Valerie M. Weaver. 2010. “The Extracellular Matrix at a Glance.” *Journal of Cell Science* 123(24): 4195. /pmc/articles/PMC2995612/ (April 14, 2023).

Gaggioli, Cedric et al. 2007. “Fibroblast-Led Collective Invasion of Carcinoma Cells with Differing Roles for RhoGTPases in Leading and Following Cells.” *Nature cell biology* 9(12): 1392–1400. https://pubmed.ncbi.nlm.nih.gov/18037882/ (December 17, 2022).

Gardel, Margaret L., Ian C. Schneider, Yvonne Aratyn-Schaus, and Clare M. Waterman. 2010. “Mechanical Integration of Actin and Adhesion Dynamics in Cell Migration.” *Annual review of cell and developmental biology* 26: 315. /pmc/articles/PMC4437624/ (November 21, 2022).

Geiger, Benjamin, Joachim P. Spatz, and Alexander D. Bershadsky. 2009. “Environmental Sensing through Focal Adhesions.” *Nature reviews. Molecular*

cell biology 10(1): 21–33. https://pubmed.ncbi.nlm.nih.gov/19197329/ (November 21, 2022).

Genes, Nicholas G., Jonathan A. Rowley, David J. Mooney, and Lawrence J. Bonassar. 2004. “Effect of Substrate Mechanics on Chondrocyte Adhesion to Modified Alginate Surfaces.” *Archives of Biochemistry and Biophysics* 422(2): 161–67. https://pubmed.ncbi.nlm.nih.gov/14759603/ (November 29, 2022).

Gibbs, Holly C. et al. 2021. “Navigating the Light-Sheet Image Analysis Software Landscape: Concepts for Driving Cohesion From Data Acquisition to Analysis.” *Frontiers in Cell and Developmental Biology* 9. /pmc/articles/PMC8631767/ (November 4, 2022).

Gilkes, Daniele M., Gregg L. Semenza, and Denis Wirtz. 2014. “Hypoxia and the Extracellular Matrix: Drivers of Tumour Metastasis.” *Nature reviews. Cancer* 14(6): 430–39. https://pubmed.ncbi.nlm.nih.gov/24827502/ (November 26, 2022).

Glassman, Wenling, Mary Bryam-Smith, and Robert E. Garfield. 1995. “Changes in Rat Cervical Collagen during Gestation and after Antiprogesterone Treatment as Measured in Vivo with Light-Induced Autofluorescence.” *American journal of obstetrics and gynecology* 173(5): 1550–56. https://pubmed.ncbi.nlm.nih.gov/7503200/ (August 22, 2022).

Goetz, Jacky G. et al. 2011. “Biomechanical Remodeling of the Microenvironment by Stromal Caveolin-1 Favors Tumor Invasion and Metastasis.” *Cell* 146(1): 148–63. http://www.cell.com/article/S0092867411006453/fulltext (December 17, 2022).

Gostynska, Natalia et al. 2017. “3D Porous Collagen Scaffolds Reinforced by Glycation with Ribose for Tissue Engineering Application.” *Biomedical Materials (Bristol)* 12(5).

Grinnell, Frederick. 2003. “Fibroblast Biology in Three-Dimensional Collagen Matrices.” *Trends in Cell Biology* 13(5): 264–69. https://pubmed.ncbi.nlm.nih.gov/12742170/ (November 27, 2022).

Gupton, Stephanie L., and Clare M. Waterman-Storer. 2006. “Spatiotemporal Feedback between Actomyosin and Focal-Adhesion Systems Optimizes Rapid Cell Migration.” *Cell* 125(7): 1361–74.

Gustafsson, M. G.L. 2000. “Surpassing the Lateral Resolution Limit by a Factor of Two Using Structured Illumination Microscopy.” *Journal of Microscopy* 198(2): 82–87. https://onlinelibrary.wiley.com/doi/full/10.1046/j.1365-2818.2000.00710.x (December 2, 2022).

Hagedorn, Elliott J. et al. 2013. “The Netrin Receptor DCC Focuses Invadopodia-Driven Basement Membrane Transmigration in Vivo.” *The Journal of cell biology* 201(6): 903–13. https://pubmed.ncbi.nlm.nih.gov/23751497/ (November 26, 2022).

Hall, Matthew S. et al. 2016. “Fibrous Nonlinear Elasticity Enables Positive Mechanical Feedback between Cells and ECMs.” *Proceedings of the National Academy of Sciences of the United States of America* 113(49): 14043–48. https://pubmed.ncbi.nlm.nih.gov/27872289/ (December 18, 2022).

Han, Yu Long et al. 2018a. “Cell Contraction Induces Long-Ranged Stress Stiffening in the Extracellular Matrix.” *Proceedings of the National Academy of Sciences of the United States of America* 115(16): 4075–80. https://www.pnas.org/doi/abs/10.1073/pnas.1722619115 (December 18, 2022).

———. 2018b. “Cell Contraction Induces Long-Ranged Stress Stiffening in the Extracellular Matrix.” *PNAS* 115.

Harburger, David S., and David A. Calderwood. 2009. “Erratum: Integrin Signalling at a Glance (Journal of Cell Science Vol. 122 (159-163)).” *Journal of Cell Science* 122(9): 1472.

Hartman, Christopher D., Brett C. Isenberg, Samantha G. Chua, and Joyce Y. Wong. 2017. “Extracellular Matrix Type Modulates Cell Migration on Mechanical Gradients.” *Experimental cell research* 359(2): 361–66. https://pubmed.ncbi.nlm.nih.gov/28821395/ (November 21, 2022).

He, Xiaolin et al. 2022. “Myofibroblast YAP/TAZ Activation Is a Key Step in Organ Fibrogenesis.” *JCI Insight* 7(4). /pmc/articles/PMC8876427/ (December 21, 2022).

Heck, Tommy et al. 2020. “The Role of Actin Protrusion Dynamics in Cell Migration through a Degradable Viscoelastic Extracellular Matrix: Insights from a Computational Model.” *PLOS Computational Biology* 16(1): e1007250. https://journals.plos.org/ploscompbiol/article?id=10.1371/journal.pcbi.1007250 (December 22, 2022).

HELL, S., G. REINER, C. CREMER, and E. H.K. STELZER. 1993. “Aberrations in Confocal Fluorescence Microscopy Induced by Mismatches in Refractive Index.” *Journal of Microscopy* 169(3): 391–405. https://onlinelibrary.wiley.com/doi/full/10.1111/j.1365-2818.1993.tb03315.x (October 18, 2022).

van Helvert, Sjoerd, Cornelis Storm, and Peter Friedl. 2017a. “Mechanoreciprocity in Cell Migration.” *Nature Cell Biology 2017 20:1* 20(1): 8–20. https://www.nature.com/articles/s41556-017-0012-0 (September 5, 2022).

———. 2017b. “Mechanoreciprocity in Cell Migration.” *Nature Cell Biology 2017 20:1* 20(1): 8–20. https://www.nature.com/articles/s41556-017-0012-0 (December 18, 2022).

———. 2017c. “Mechanoreciprocity in Cell Migration.” *Nature Cell Biology*. https://doi.org/10.1038/s41556-017-0012-0 (January 20, 2020).

Hemmler, Daniel et al. 2018. “Insights into the Chemistry of Non-Enzymatic Browning Reactions in Different Ribose-Amino Acid Model Systems.” *Scientific Reports 2018 8:1* 8(1): 1–10. https://www.nature.com/articles/s41598-018-34335-5 (November 29, 2022).

Henderson, Elizabeth, Brian K. Rutt, and Ting Yim Lee. 1998. “Temporal Sampling Requirements for the Tracer Kinetics Modeling of Breast Disease.” *Magnetic resonance imaging* 16(9): 1057–73. https://pubmed.ncbi.nlm.nih.gov/9839990/ (December 18, 2022).

Hiramatsu, Ryuji et al. 2013. “External Mechanical Cues Trigger the Establishment of the Anterior-Posterior Axis in Early Mouse Embryos.” *Developmental cell* 27(2): 131–44. https://pubmed.ncbi.nlm.nih.gov/24176640/ (November 26, 2022).

Hirvonen, L M, R J Marsh, G E Jones, and S Cox. 2020. “Combined AFM and Super-Resolution Localisation Microscopy: Investigating the Structure and Dynamics of Podosomes.” *European Journal of Cell Biology* 99(7): 151106.

Hochmuth, Robert M. 2000. “Micropipette Aspiration of Living Cells.” *Journal of biomechanics* 33(1): 15–22. https://pubmed.ncbi.nlm.nih.gov/10609514/ (August 23, 2022).

Hodge, John E. 1955. “The Amadori Rearrangement.” *Advances in carbohydrate chemistry* 10(C): 169–205. https://pubmed.ncbi.nlm.nih.gov/13292324/ (November 29, 2022).

Hoffman, Brenton D., Gladys Massiera, Kathleen M. van Citters, and John C. Crocker. 2006. “The Consensus Mechanics of Cultured Mammalian Cells.” *Proceedings of the National Academy of Sciences of the United States of America* 103(27): 10259–64. https://www.pnas.org/doi/abs/10.1073/pnas.0510348103 (August 23, 2022).

Hoshino, Ayuko et al. 2015. “Tumour Exosome Integrins Determine Organotropic Metastasis.” *Nature* 527(7578): 329–35. https://pubmed.ncbi.nlm.nih.gov/26524530/ (December 6, 2022).

Hui, Erica, Leandro Moretti, Thomas H. Barker, and Steven R. Caliari. 2021. “The Combined Influence of Viscoelastic and Adhesive Cues on Fibroblast Spreading and Focal Adhesion Organization.” *Cellular and Molecular Bioengineering 2021 14:5* 14(5): 427–40. https://link.springer.com/article/10.1007/s12195-021-00672-1 (December 20, 2022).

Hynes, Richard O. 2002. “Integrins: Bidirectional, Allosteric Signaling Machines.” *Cell* 110(6): 673–87. https://pubmed.ncbi.nlm.nih.gov/12297042/ (December 29, 2022).

Iozzo, Renato v., and Nikos Karamanos. 2010. “Proteoglycans in Health and Disease: Emerging Concepts and Future Directions.” *The FEBS journal* 277(19): 3863. https://pubmed.ncbi.nlm.nih.gov/20812984/ (November 20, 2022).

Iozzo, Renato v., and Liliana Schaefer. 2015. “Proteoglycan Form and Function: A Comprehensive Nomenclature of Proteoglycans.” *Matrix biology : journal of the*

International Society for Matrix Biology 42: 11–55. https://pubmed.ncbi.nlm.nih.gov/25701227/ (November 20, 2022).

Jacquemet, Guillaume, Hellyeh Hamidi, and Johanna Ivaska. 2015. “Filopodia in Cell Adhesion, 3D Migration and Cancer Cell Invasion.” *Current Opinion in Cell Biology* 36: 23–31.

Järveläinen, Hannu et al. 2009. “Extracellular Matrix Molecules: Potential Targets in Pharmacotherapy.” *Pharmacological Reviews* 61(2): 198. /pmc/articles/PMC2830117/ (November 19, 2022).

De Jong, Sanne et al. 2014. “Ex Vivo and in Vivo Administration of Fluorescent CNA35 Specifically Marks Cardiac Fibrosis.” *Molecular Imaging* 13(10). https://journals.sagepub.com/doi/full/10.2310/7290.2014.00036 (April 20, 2023).

Junqueira, L. C.U., G. Bignolas, and R. R. Brentani. 1979. “Picrosirius Staining plus Polarization Microscopy, a Specific Method for Collagen Detection in Tissue Sections.” *The Histochemical journal* 11(4): 447–55. https://pubmed.ncbi.nlm.nih.gov/91593/ (August 22, 2022).

Kai, Fui Boon, Hanane Laklai, and Valerie M. Weaver. 2016. “Force Matters: Biomechanical Regulation of Cell Invasion and Migration in Disease.” *Trends in cell biology* 26(7): 486–97. https://pubmed.ncbi.nlm.nih.gov/27056543/ (November 19, 2022).

Kardos, Roland et al. 2009. “The Effects of ADF/Cofilin and Profilin on the Conformation of the ATP-Binding Cleft of Monomeric Actin.” *Biophysical Journal* 96(6): 2335–43.

Kechagia, Jenny Z., Johanna Ivaska, and Pere Roca-Cusachs. 2019a. “Integrins as Biomechanical Sensors of the Microenvironment.” *Nature Reviews Molecular Cell Biology 2019 20:8* 20(8): 457–73. https://www.nature.com/articles/s41580-019-0134-2 (December 4, 2022).

———. 2019b. “Integrins as Biomechanical Sensors of the Microenvironment.” *Nature Reviews Molecular Cell Biology 2019 20:8* 20(8): 457–73. https://www.nature.com/articles/s41580-019-0134-2 (December 21, 2022).

Keller, Ray, Lance A. Davidson, and David R. Shook. 2003. “How We Are Shaped: The Biomechanics of Gastrulation.” *Differentiation* 71(3): 171–205.

Kelley, Laura C., Lauren L. Lohmer, Elliott J. Hagedorn, and David R. Sherwood. 2014. “Traversing the Basement Membrane in Vivo: A Diversity of Strategies.” *The Journal of cell biology* 204(3): 291–302. https://pubmed.ncbi.nlm.nih.gov/24493586/ (November 26, 2022).

Kendall, Ryan T., and Carol A. Feghali-Bostwick. 2014. “Fibroblasts in Fibrosis: Novel Roles and Mediators.” *Frontiers in Pharmacology* 5. /pmc/articles/PMC4034148/ (December 4, 2022).

Kerber, Michael L., and Richard E. Cheney. 2011. “Myosin-X: A MyTH-FERM Myosin at the Tips of Filopodia.” *Journal of Cell Science* 124(22): 3733–41. https://journals.biologists.com/jcs/article/124/22/3733/64641/Myosin-X-a-MyTH-FERM-myosin-at-the-tips-of (December 29, 2022).

Kessenbrock, Kai, Chih Yang Wang, and Zena Werb. 2015. “Matrix Metalloproteinases in Stem Cell Regulation and Cancer.” *Matrix biology : journal of the International Society for Matrix Biology* 44–46: 184–90. https://pubmed.ncbi.nlm.nih.gov/25661772/ (November 26, 2022).

Kim, Hye Min, Woo Hee Jung, and Ja Seung Koo. 2015. “Expression of Yes-Associated Protein (YAP) in Metastatic Breast Cancer.” *International Journal of Clinical and Experimental Pathology* 8(9): 11248. /pmc/articles/PMC4637664/ (December 21, 2022).

Kim, Soo Hyun, Jeremy Turnbull, and Scott Guimond. 2011. “Extracellular Matrix and Cell Signalling: The Dynamic Cooperation of Integrin, Proteoglycan and Growth Factor Receptor.” *The Journal of endocrinology* 209(2): 139–51. https://pubmed.ncbi.nlm.nih.gov/21307119/ (November 19, 2022).

Kleinman, Hynda K., and George R. Martin. 2005. “Matrigel: Basement Membrane Matrix with Biological Activity.” *Seminars in cancer biology* 15(5): 378–86. https://pubmed.ncbi.nlm.nih.gov/15975825/ (November 27, 2022).

Kniazeva, Ekaterina, and Andrew J. Putnam. 2009. “Endothelial Cell Traction and ECM Density Influence Both Capillary Morphogenesis and Maintenance in 3-D.” *American journal of physiology. Cell physiology* 297(1). https://pubmed.ncbi.nlm.nih.gov/19439531/ (November 29, 2022).

Kodack, David P. et al. 2017. “Primary Patient-Derived Cancer Cells and Their Potential for Personalized Cancer Patient Care.” *Cell Reports* 21(11): 3298. /pmc/articles/PMC5745232/ (December 22, 2022).

Krakhmal, N. v. et al. 2015. “Cancer Invasion: Patterns and Mechanisms.” *Acta Naturae* 7(2): 17. /pmc/articles/PMC4463409/ (December 21, 2022).

Krause, Matthias, and Alexis Gautreau. 2014. “Steering Cell Migration: Lamellipodium Dynamics and the Regulation of Directional Persistence.” *Nature Reviews Molecular Cell Biology 2014 15:9* 15(9): 577–90. https://www.nature.com/articles/nrm3861 (August 24, 2022).

Kubow, Kristopher E., Sarah K. Conrad, and A. Rick Horwitz. 2013. “Matrix Microarchitecture and Myosin II Determine Adhesion in 3D Matrices.” *Current Biology* 23(17): 1607–19.

Kulsum, Safeena et al. 2019. “Cancer Stem Cells and Fibroblast Niche Cross Talk in an In-Vitro Oral Dysplasia Model.” *Molecular Carcinogenesis* 58(5): 820–31. https://onlinelibrary.wiley.com/doi/full/10.1002/mc.22974 (December 6, 2022).

Lamar, John M. et al. 2019. “SRC Tyrosine Kinase Activates the YAP/TAZ Axis and Thereby Drives Tumor Growth and Metastasis.” *The Journal of biological chemistry* 294(7): 2302–17. https://pubmed.ncbi.nlm.nih.gov/30559289/ (December 21, 2022).

Lämmermann, Tim et al. 2008. “Rapid Leukocyte Migration by Integrin-Independent Flowing and Squeezing.” *Nature 2008 453:7191* 453(7191): 51–55. https://www.nature.com/articles/nature06887 (December 21, 2022).

Lanza, Alessandro, Serena Morigi, Fiorella Sgallari, and You Wei Wen. 2014. “Image Restoration with Poisson–Gaussian Mixed Noise.” *https://doi.org/10.1080/21681163.2013.811039* 2(1): 12–24. https://www.tandfonline.com/doi/abs/10.1080/21681163.2013.811039 (October 18, 2022).

Laurent, Michel, Georges Johannin, Hervé Guyader, and Anne Fleury. 1992. “Confocal Scanning Optical Microscopy and Three-Dimensional Imaging.” *Biology of the Cell* 76(1): 113–24. http://doi.wiley.com/10.1016/0248-4900%2892%2990203-D (April 20, 2023).

Lee, Jun Ho et al. 2016. “Comparison of Reflectance Confocal Microscopy and Two-Photon Second Harmonic Generation Microscopy in Fungal Keratitis Rabbit Model Ex Vivo.” *Biomedical Optics Express* 7(2): 677. /pmc/articles/PMC4771480/ (September 2, 2022).

Lee, Mee Hyun, Joydeb Kumar Kundu, Jung il Chae, and Jung Hyun Shim. 2019. “Targeting ROCK/LIMK/Cofilin Signaling Pathway in Cancer.” *Archives of Pharmacal Research* 42(6): 481–91. https://link.springer.com/article/10.1007/s12272-019-01153-w (December 21, 2022).

Lee, Soo Hong, James J. Moon, and Jennifer L. West. 2008. “Three-Dimensional Micropatterning of Bioactive Hydrogels via Two-Photon Laser Scanning Photolithography for Guided 3D Cell Migration.” *Biomaterials* 29(20): 2962–68. https://pubmed.ncbi.nlm.nih.gov/18433863/ (November 27, 2022).

Lehnert, Dirk et al. 2004. “Cell Behaviour on Micropatterned Substrata: Limits of Extracellular Matrix Geometry for Spreading and Adhesion.” *Journal of cell science* 117(Pt 1): 41–52. https://pubmed.ncbi.nlm.nih.gov/14657272/ (November 27, 2022).

Levental, I. et al. 2010. “A Simple Indentation Device for Measuring Micrometer-Scale Tissue Stiffness.” *Journal of Physics: Condensed Matter* 22(19): 194120. https://iopscience.iop.org/article/10.1088/0953-8984/22/19/194120 (August 23, 2022).

Levental, Kandice R. et al. 2009. “Matrix Crosslinking Forces Tumor Progression by Enhancing Integrin Signaling.” *Cell* 139(5): 891–906. https://pubmed.ncbi.nlm.nih.gov/19931152/ (November 26, 2022).

Lichtman, Jeff W., and José Angel Conchello. 2005. “Fluorescence Microscopy.” *Nature Methods 2005 2:12* 2(12): 910–19. https://www.nature.com/articles/nmeth817 (December 2, 2022).

Liu, J. et al. 2006. “Microrheology Probes Length Scale Dependent Rheology.” *Physical Review Letters* 96(11): 118104. https://journals.aps.org/prl/abstract/10.1103/PhysRevLett.96.118104 (August 23, 2022).

Liu, S., D. A. Calderwood, and M. H. Ginsberg. 2000. “Integrin Cytoplasmic Domain-Binding Proteins.” *Journal of cell science* 113 (Pt 20)(20): 3563–71. https://pubmed.ncbi.nlm.nih.gov/11017872/ (November 21, 2022).

Lo, Chun Min, Hong Bei Wang, Micah Dembo, and Yu Li Wang. 2000a. “Cell Movement Is Guided by the Rigidity of the Substrate.” *Biophysical Journal* 79(1): 144. /pmc/articles/PMC1300921/?report=abstract (December 17, 2022).

———. 2000b. “Cell Movement Is Guided by the Rigidity of the Substrate.” *Biophysical Journal* 79(1): 144–52.

Lo, Su Hao. 2006. “Focal Adhesions: What’s New Inside.” *Developmental Biology* 294(2): 280–91.

Lu, Pengfei, Ken Takai, Valerie M. Weaver, and Zena Werb. 2011. “Extracellular Matrix Degradation and Remodeling in Development and Disease.” *Cold Spring Harbor perspectives in biology* 3(12). https://pubmed.ncbi.nlm.nih.gov/21917992/ (November 19, 2022).

Lucero, H. A., and H. M. Kagan. 2006. “Lysyl Oxidase: An Oxidative Enzyme and Effector of Cell Function.” *Cellular and molecular life sciences : CMLS* 63(19–20): 2304–16. https://pubmed.ncbi.nlm.nih.gov/16909208/ (November 21, 2022).

Luisier, Florian, Cédric Vonesch, Thierry Blu, and Michael Unser. 2010. “Fast Interscale Wavelet Denoising of Poisson-Corrupted Images.” *Signal Processing* 90(2): 415–27. https://www.researchgate.net/publication/221998101_Fast_Interscale_Wavelet_Denoising_of_Poisson-Corrupted_Images (October 18, 2022).

Lutolf, M. P., and J. A. Hubbell. 2005. “Synthetic Biomaterials as Instructive Extracellular Microenvironments for Morphogenesis in Tissue Engineering.” *Nature Biotechnology 2005 23:1* 23(1): 47–55. https://www.nature.com/articles/nbt1055 (November 27, 2022).

Mahaffy, R. E. et al. 2004. “Quantitative Analysis of the Viscoelastic Properties of Thin Regions of Fibroblasts Using Atomic Force Microscopy.” *Biophysical Journal* 86(3): 1777. /pmc/articles/PMC1304012/ (August 23, 2022).

Maller, Ori et al. 2021. “Tumour-Associated Macrophages Drive Stromal Cell-Dependent Collagen Crosslinking and Stiffening to Promote Breast Cancer

Aggression.” *Nature materials* 20(4): 548–59. https://pubmed.ncbi.nlm.nih.gov/33257795/ (December 21, 2022).

Mana, Giulia, Donatella Valdembri, and Guido Serini. 2020. “Conformationally Active Integrin Endocytosis and Traffic: Why, Where, When and How?” *Biochemical Society Transactions* 48(1): 83. /pmc/articles/PMC7054750/ (December 4, 2022).

Mantovani, Alberto et al. 2017. “Tumour-Associated Macrophages as Treatment Targets in Oncology.” *Nature reviews. Clinical oncology* 14(7): 399–416. https://pubmed.ncbi.nlm.nih.gov/28117416/ (December 22, 2022).

Marcotti, Stefania et al. 2021. “A Workflow for Rapid Unbiased Quantification of Fibrillar Feature Alignment in Biological Images.” *bioRxiv*: 2021.07.22.453401. https://www.biorxiv.org/content/10.1101/2021.07.22.453401v1 (September 1, 2022).

Martino, Fabiana et al. 2018. “Cellular Mechanotransduction: From Tension to Function.” *Frontiers in physiology* 9(JUL). https://pubmed.ncbi.nlm.nih.gov/30026699/ (November 23, 2022).

Mascharak, Shamik et al. 2021. “Preventing Engrailed-1 Activation in Fibroblasts Yields Wound Regeneration without Scarring.” *Science* 372(6540). https://www.science.org/doi/10.1126/science.aba2374 (September 2, 2022).

Mason, Brooke N et al. 2012. “Tuning 3D Collagen Matrix Stiffness Independently of Collagen Concentration Modulates Endothelial Cell Behavior.”

Mason, Brooke N. et al. 2013a. “Tuning 3D Collagen Matrix Stiffness Independently of Collagen Concentration Modulates Endothelial Cell Behavior.” *Acta biomaterialia* 9(1): 4635. /pmc/articles/PMC3508162/ (September 5, 2022).

———. 2013b. “Tuning Three-Dimensional Collagen Matrix Stiffness Independently of Collagen Concentration Modulates Endothelial Cell Behavior.” *Acta Biomaterialia* 9(1): 4635–44.

Mason, Brooke N., and Cynthia A. Reinhart-King. 2013. “Controlling the Mechanical Properties of Three-Dimensional Matrices via Non-Enzymatic Collagen Glycation.” *http://dx.doi.org/10.4161/org.24942* 9(2): 70–75. https://www.tandfonline.com/doi/abs/10.4161/org.24942 (August 24, 2022).

Mata, Alvaro et al. 2009. “Micropatterning of Bioactive Self-Assembling Gels.” *Soft Matter* 5(6): 1228–36. https://pubs.rsc.org/en/content/articlehtml/2009/sm/b819002j (November 27, 2022).

Mattila, Pieta K., and Pekka Lappalainen. 2008. “Filopodia: Molecular Architecture and Cellular Functions.” *Nature reviews. Molecular cell biology* 9(6): 446–54. https://pubmed.ncbi.nlm.nih.gov/18464790/ (October 18, 2022).

Mierke, Claudia T. et al. 2017a. “Focal Adhesion Kinase Activity Is Required for Actomyosin Contractility-Based Invasion of Cells into Dense 3D Matrices.” *Scientific Reports 2017 7:1* 7(1): 1–18. https://www.nature.com/articles/srep42780 (December 5, 2022).

———. 2017b. “Focal Adhesion Kinase Activity Is Required for Actomyosin Contractility-Based Invasion of Cells into Dense 3D Matrices.” *Scientific Reports 2017 7:1* 7(1): 1–18. https://www.nature.com/articles/srep42780 (December 29, 2022).

Miller, Jordan S. et al. 2010. “Bioactive Hydrogels Made from Step-Growth Derived PEG-Peptide Macromers.” *Biomaterials* 31(13): 3736–43. https://pubmed.ncbi.nlm.nih.gov/20138664/ (November 27, 2022).

Miller, Lance D. et al. 2005. “An Expression Signature for P53 Status in Human Breast Cancer Predicts Mutation Status, Transcriptional Effects, and Patient Survival.” *Proceedings of the National Academy of Sciences of the United States of America* 102(38): 13550–55. https://www.pnas.org/doi/abs/10.1073/pnas.0506230102 (December 21, 2022).

Miranti, Cindy K., and Joan S. Brugge. 2002. “Sensing the Environment: A Historical Perspective on Integrin Signal Transduction.” *Nature cell biology* 4(4). https://pubmed.ncbi.nlm.nih.gov/11944041/ (December 29, 2022).

Nair, Neha et al. 2017. “A Cancer Stem Cell Model as the Point of Origin of Cancer-Associated Fibroblasts in Tumor Microenvironment.” *Scientific Reports 2017 7:1* 7(1): 1–13. https://www.nature.com/articles/s41598-017-07144-5 (December 6, 2022).

Naomi, Ruth, Pauzi Muhd Ridzuan, and Hasnah Bahari. 2021. “Current Insights into Collagen Type I.” *Polymers* 13(16). /pmc/articles/PMC8399689/ (December 4, 2022).

Nikitovic, Dragana et al. 2018. “Proteoglycans-Biomarkers and Targets in Cancer Therapy.” *Frontiers in Endocrinology* 9(MAR): 69.

Oh, Myung Jin, Frank Kuhr, Fitzroy Byfield, and Irena Levitan. 2012. “Micropipette Aspiration of Substrate-Attached Cells to Estimate Cell Stiffness.” *Journal of Visualized Experiments* (67).

Ouellette, Jonathan N. et al. 2021. “Navigating the Collagen Jungle: The Biomedical Potential of Fiber Organization in Cancer.” *Bioengineering* 8(2): 1–19. /pmc/articles/PMC7909776/ (September 2, 2022).

Ozaki, Toshinori, and Akira Nakagawara. 2011. “Role of P53 in Cell Death and Human Cancers.” *Cancers* 3(1): 994. /pmc/articles/PMC3756401/ (December 6, 2022).

Özdemir, Berna C. et al. 2014. “Depletion of Carcinoma-Associated Fibroblasts and Fibrosis Induces Immunosuppression and Accelerates Pancreas Cancer with Reduced Survival.” *Cancer cell* 25(6): 719–34. https://pubmed.ncbi.nlm.nih.gov/24856586/ (November 26, 2022).

Pakshir, Pardis et al. 2019. “Dynamic Fibroblast Contractions Attract Remote Macrophages in Fibrillar Collagen Matrix.” *Nature Communications 2019 10:1* 10(1): 1–17. https://www.nature.com/articles/s41467-019-09709-6 (December 18, 2022).

Palecek, Sean P. et al. 1997. “Integrin-Ligand Binding Properties Govern Cell Migration Speed through Cell-Substratum Adhesiveness.” *Nature* 385(6616): 537–40. https://pubmed.ncbi.nlm.nih.gov/9020360/ (November 21, 2022).

Pampaloni, Francesco, Emmanuel G. Reynaud, and Ernst H.K. Stelzer. 2007. “The Third Dimension Bridges the Gap between Cell Culture and Live Tissue.” *Nature Reviews Molecular Cell Biology 2007 8:10* 8(10): 839–45. https://www.nature.com/articles/nrm2236 (November 27, 2022).

Pandya, Pahini, Jose L. Orgaz, and Victoria Sanz-Moreno. 2017. “Actomyosin Contractility and Collective Migration: May the Force Be with You.” *Current Opinion in Cell Biology* 48: 87–96.

Pang, Yonggang, Xiaoli Wang, Dongkeun Lee, and Howard P. Greisler. 2011. “Dynamic Quantitative Visualization of Single Cell Alignment and Migration and Matrix Remodeling in 3-D Collagen Hydrogels under Mechanical Force.” *Biomaterials* 32(15): 3776–83.

Pankov, Roumen, and Kenneth M Yamada. 2002a. “Fibronectin at a Glance.” *Journal of Cell Science* 115: 3861–63.

Pankov, Roumen, and Kenneth M. Yamada. 2002b. “Fibronectin at a Glance.” *Journal of cell science* 115(Pt 20): 3861–63. https://pubmed.ncbi.nlm.nih.gov/12244123/ (November 21, 2022).

Parisi, Ludovica et al. 2020. “A Glance on the Role of Fibronectin in Controlling Cell Response at Biomaterial Interface.” *The Japanese Dental Science Review* 56(1): 50. /pmc/articles/PMC6928270/ (December 3, 2022).

Park, Danielle et al. 2020. “Extracellular Matrix Anisotropy Is Determined by TFAP2C-Dependent Regulation of Cell Collisions.” *Nature materials* 19(2): 227–38. https://pubmed.ncbi.nlm.nih.gov/31659294/ (September 2, 2022).

Paszek, Matthew J. et al. 2005a. “Tensional Homeostasis and the Malignant Phenotype.” *Cancer cell* 8(3): 241–54. https://pubmed.ncbi.nlm.nih.gov/16169468/ (November 25, 2022).

———. 2005b. “Tensional Homeostasis and the Malignant Phenotype.” *Cancer Cell* 8(3): 241–54.

———. 2005c. “Tensional Homeostasis and the Malignant Phenotype.” *Cancer Cell* 8(3): 241–54.

Paszek, Matthew J., David Boettiger, Valerie M. Weaver, and Daniel A. Hammer. 2009. “Integrin Clustering Is Driven by Mechanical Resistance from the Glycocalyx and the Substrate.” *PLOS Computational Biology* 5(12): e1000604. https://journals.plos.org/ploscompbiol/article?id=10.1371/journal.pcbi.1000604 (December 4, 2022).

Paul, Nikki R., Guillaume Jacquemet, and Patrick T. Caswell. 2015a. “Endocytic Trafficking of Integrins in Cell Migration.” *Current biology : CB* 25(22): R1092–1105. https://pubmed.ncbi.nlm.nih.gov/26583903/ (December 5, 2022).

———. 2015b. “Endocytic Trafficking of Integrins in Cell Migration.” *Current Biology* 25(22): R1092–1105.

———. 2015c. “Endocytic Trafficking of Integrins in Cell Migration.” *Current Biology* 25(22): R1092–1105.

Pedersen, John A., and Melody A. Swartz. 2005. “Mechanobiology in the Third Dimension.” *Annals of Biomedical Engineering* 33(11): 1469–90.

Peng, Yueting et al. 2022. “Non-Muscle Myosin II Isoforms Orchestrate Substrate Stiffness Sensing to Promote Cancer Cell Contractility and Migration.” *Cancer Letters* 524: 245–58.

Petrie, Ryan J., Núria Gavara, Richard S. Chadwick, and Kenneth M. Yamada. 2012. “Nonpolarized Signaling Reveals Two Distinct Modes of 3D Cell Migration.” *The Journal of cell biology* 197(3): 439–55. https://pubmed.ncbi.nlm.nih.gov/22547408/ (December 21, 2022).

Petrie, Ryan J., Hyun Koo, and Kenneth M. Yamada. 2014. “Generation of Compartmentalized Pressure by a Nuclear Piston Governs Cell Motility in a 3D Matrix.” *Science (New York, N.Y.)* 345(6200): 1062–65. https://pubmed.ncbi.nlm.nih.gov/25170155/ (December 18, 2022).

Plotnikov, Sergey v., Ana M. Pasapera, Benedikt Sabass, and Clare M. Waterman. 2012. “Force Fluctuations within Focal Adhesions Mediate ECM-Rigidity Sensing to Guide Directed Cell Migration.” *Cell* 151(7): 1513–27. http://dx.doi.org/10.1016/j.cell.2012.11.034.

Pompili, Simona et al. 2021. “The Charming World of the Extracellular Matrix: A Dynamic and Protective Network of the Intestinal Wall.” *Frontiers in Medicine* 8: 477.

Provenzano, Paolo P. et al. 2006. “Collagen Reorganization at the Tumor-Stromal Interface Facilitates Local Invasion.” *BMC medicine* 4(1). https://pubmed.ncbi.nlm.nih.gov/17190588/ (November 25, 2022).

———. 2008. “Collagen Density Promotes Mammary Tumor Initiation and Progression.” *BMC medicine* 6. https://pubmed.ncbi.nlm.nih.gov/18442412/ (November 26, 2022).

Raab-Westphal, Sabine, John F. Marshall, and Simon L. Goodman. 2017. “Integrins as Therapeutic Targets: Successes and Cancers.” *Cancers* 9(9). https://pubmed.ncbi.nlm.nih.gov/28832494/ (November 19, 2022).

Raeber, G. P., M. P. Lutolf, and J. A. Hubbell. 2005. “Molecularly Engineered PEG Hydrogels: A Novel Model System for Proteolytically Mediated Cell Migration.” *Biophysical Journal* 89(2): 1374. /pmc/articles/PMC1366622/ (November 27, 2022).

Ray, Arja, Oscar Lee, et al. 2017. “Anisotropic Forces from Spatially Constrained Focal Adhesions Mediate Contact Guidance Directed Cell Migration.” *Nature communications* 8. https://pubmed.ncbi.nlm.nih.gov/28401884/ (December 18, 2022).

Ray, Arja, Zachary M. Slama, et al. 2017. “Enhanced Directional Migration of Cancer Stem Cells in 3D Aligned Collagen Matrices.” *Biophysical Journal* 112(5).

Reichheld, Sean E. et al. 2019. “Sequence Variants of Human Tropoelastin Affecting Assembly, Structural Characteristics and Functional Properties of Polymeric Elastin in Health and Disease.” *Matrix biology : journal of the International Society for Matrix Biology* 84: 68–80. https://pubmed.ncbi.nlm.nih.gov/31254613/ (November 19, 2022).

Reigle, Kristin L. et al. 2008. “Non-Enzymatic Glycation of Type I Collagen Diminishes Collagen-Proteoglycan Binding and Weakens Cell Adhesion.” *Journal of cellular biochemistry* 104(5): 1684. /pmc/articles/PMC2746388/ (November 29, 2022).

Renkawitz, Jörg et al. 2019. “Nuclear Positioning Facilitates Amoeboid Migration along the Path of Least Resistance.” *Nature 2019 568:7753* 568(7753): 546–50. https://www.nature.com/articles/s41586-019-1087-5 (December 21, 2022).

Ricard-Blum, Sylvie, and Florence Ruggiero. 2005. “The Collagen Superfamily: From the Extracellular Matrix to the Cell Membrane.” *Pathologie-biologie* 53(7): 430–42. https://pubmed.ncbi.nlm.nih.gov/16085121/ (November 19, 2022).

Riching, Kristin M. et al. 2014. “3D Collagen Alignment Limits Protrusions to Enhance Breast Cancer Cell Persistence.” *Biophysical Journal* 107(11): 2546–58.

Rizzelli, Francesca, Maria Grazia Malabarba, Sara Sigismund, and Marina Mapelli. 2020. “The Crosstalk between Microtubules, Actin and Membranes Shapes Cell Division.” *Open biology* 10(3). https://pubmed.ncbi.nlm.nih.gov/32183618/ (December 29, 2022).

Röper, Katja. 2013. “Supracellular Actomyosin Assemblies during Development.” *Ceased* 3(2): 45–49. https://www.tandfonline.com/doi/abs/10.4161/bioa.25339 (December 29, 2022).

Rosso, Francesco, Antonio Giordano, Manlio Barbarisi, and Alfonso Barbarisi. 2004. “From Cell–ECM Interactions to Tissue Engineering.” *Journal of Cellular Physiology* 199(2): 174–80. https://onlinelibrary.wiley.com/doi/full/10.1002/jcp.10471 (December 4, 2022).

Rozario, Tania, and Douglas W. DeSimone. 2010a. “The Extracellular Matrix in Development and Morphogenesis: A Dynamic View.” *Developmental biology* 341(1): 126–40. https://pubmed.ncbi.nlm.nih.gov/19854168/ (November 19, 2022).

———. 2010b. “The Extracellular Matrix in Development and Morphogenesis: A Dynamic View.” *Developmental biology* 341(1): 126–40. https://pubmed.ncbi.nlm.nih.gov/19854168/ (November 21, 2022).

Sagot, Isabelle et al. 2002. “An Actin Nucleation Mechanism Mediated by Bni1 and Profilin.” *Nature Cell Biology 2002 4:8* 4(8): 626–31. https://www.nature.com/articles/ncb834 (August 24, 2022).

Sahai, Erik, and Christopher J. Marshall. 2003. “Differing Modes of Tumour Cell Invasion Have Distinct Requirements for Rho/ROCK Signalling and Extracellular Proteolysis.” *Nature cell biology* 5(8): 711–19. https://pubmed.ncbi.nlm.nih.gov/12844144/ (October 24, 2022).

Sarntinoranont, Malisa, Frank Rooney, and Mauro Ferrari. 2003a. “Interstitial Stress and Fluid Pressure within a Growing Tumor.” *Annals of biomedical engineering*

31(3): 327–35. https://pubmed.ncbi.nlm.nih.gov/12680730/ (November 26, 2022).

———. 2003b. “Interstitial Stress and Fluid Pressure within a Growing Tumor.” *Annals of biomedical engineering* 31(3): 327–35. https://pubmed.ncbi.nlm.nih.gov/12680730/ (December 22, 2022).

Schéele, Susanne et al. 2007. “Laminin Isoforms in Development and Disease.” *Journal of molecular medicine (Berlin, Germany)* 85(8): 825–36. https://pubmed.ncbi.nlm.nih.gov/17426950/ (November 21, 2022).

Shamloo, Amir, and Sarah C. Heilshorn. 2010. “Matrix Density Mediates Polarization and Lumen Formation of Endothelial Sprouts in VEGF Gradients.” *Lab on a Chip* 10(22): 3061–68. https://pubs.rsc.org/en/content/articlehtml/2010/lc/c005069e (November 29, 2022).

Shellard, Adam, and Roberto Mayor. 2019. “Supracellular Migration - Beyond Collective Cell Migration.” *Journal of Cell Science* 132(8). https://journals.biologists.com/jcs/article/132/8/jcs226142/57322/Supracellular-migration-beyond-collective-cell (December 29, 2022).

Sheppard, Colin J.R. 2021. “The Development of Microscopy for Super-Resolution: Confocal Microscopy, and Image Scanning Microscopy.” *Applied Sciences 2021, Vol. 11, Page 8981* 11(19): 8981. https://www.mdpi.com/2076-3417/11/19/8981/htm (December 2, 2022).

Shivashankar, G. v. 2019. “Mechanical Regulation of Genome Architecture and Cell-Fate Decisions.” *Current opinion in cell biology* 56: 115–21. https://pubmed.ncbi.nlm.nih.gov/30554028/ (December 20, 2022).

Small, J. Victor, K. Rottner, I. Kaverina, and K. I. Anderson. 1998a. “Assembling an Actin Cytoskeleton for Cell Attachment and Movement.” *Biochimica et Biophysica Acta - Molecular Cell Research* 1404(3): 271–81.

———. 1998b. “Assembling an Actin Cytoskeleton for Cell Attachment and Movement.” *Biochimica et biophysica acta* 1404(3): 271–81. https://pubmed.ncbi.nlm.nih.gov/9739149/ (November 23, 2022).

Smalley, Keiran S.M., Mercedes Lioni, and Meenhard Herlyn. 2006. “Life Isn’t Flat: Taking Cancer Biology to the next Dimension.” *In vitro cellular & developmental biology. Animal* 42(8–9): 242–47. https://pubmed.ncbi.nlm.nih.gov/17163781/ (November 27, 2022).

Smirnov, Denis A. et al. 2005. “Global Gene Expression Profiling of Circulating Tumor Cells.” *Cancer research* 65(12): 4993–97. https://pubmed.ncbi.nlm.nih.gov/15958538/ (December 22, 2022).

Smith, Michael L. et al. 2007. “Force-Induced Unfolding of Fibronectin in the Extracellular Matrix of Living Cells.” *PLOS Biology* 5(10): e268. https://journals.plos.org/plosbiology/article?id=10.1371/journal.pbio.0050268 (November 21, 2022).

Sodunke, Temitope R. et al. 2007. “Micropatterns of Matrigel for Three-Dimensional Epithelial Cultures.” *Biomaterials* 28(27): 4006–16. https://pubmed.ncbi.nlm.nih.gov/17574663/ (November 27, 2022).

Solon, Jérôme et al. 2007. “Fibroblast Adaptation and Stiffness Matching to Soft Elastic Substrates.” *Biophysical journal* 93(12): 4453–61. https://pubmed.ncbi.nlm.nih.gov/18045965/ (December 18, 2022).

Spill, Fabian, Chris Bakal, and Michael Mak. 2018a. “Mechanical and Systems Biology of Cancer.” *Computational and structural biotechnology journal* 16: 237–45. https://pubmed.ncbi.nlm.nih.gov/30105089/ (December 29, 2022).

———. 2018b. “Mechanical and Systems Biology of Cancer.” *Computational and Structural Biotechnology Journal* 16: 237–45.

Staneva, Ralitza et al. 2018. “A New Biomimetic Assay Reveals the Temporal Role of Matrix Stiffening in Cancer Cell Invasion.” *Molecular Biology of the Cell* 29(25): 2979. /pmc/articles/PMC6333180/ (December 21, 2022).

Stephens, David J., and Victoria J. Allan. 2003a. “Light Microscopy Techniques for Live Cell Imaging.” *Science* 300(5616): 82–86.

———. 2003b. “Light Microscopy Techniques for Live Cell Imaging.” *Science (New York, N.Y.)* 300(5616): 82–86. https://pubmed.ncbi.nlm.nih.gov/12677057/ (December 29, 2022).

Stowers, Ryan S. et al. 2019. “Matrix Stiffness Induces a Tumorigenic Phenotype in Mammary Epithelium through Changes in Chromatin Accessibility.” *Nature biomedical engineering* 3(12): 1009–19. https://pubmed.ncbi.nlm.nih.gov/31285581/ (December 20, 2022).

Streets, Aaron M., Ang Li, Tao Chen, and Yanyi Huang. 2014. “Imaging without Fluorescence: Nonlinear Optical Microscopy for Quantitative Cellular Imaging.” *Analytical Chemistry* 86(17): 8506–13.

Stylianou, Andreas, Stylianos Vasileios Kontomaris, Colin Grant, and Eleni Alexandratou. 2019. “Atomic Force Microscopy on Biological Materials Related to Pathological Conditions.” *Scanning* 2019. /pmc/articles/PMC6535871/ (September 2, 2022).

Su, Chia Yi et al. 2021. “Engineering a 3D Collective Cancer Invasion Model with Control over Collagen Fiber Alignment.” *Biomaterials* 275: 120922.

Sulli, Gabriele, Raffaella di Micco, and Fabrizio D.Adda di Fagagna. 2012. “Crosstalk between Chromatin State and DNA Damage Response in Cellular Senescence and Cancer.” *Nature reviews. Cancer* 12(10): 709–20. https://pubmed.ncbi.nlm.nih.gov/22952011/ (December 6, 2022).

Sun, Xiaoyu et al. 2015. “Asymmetric Nanotopography Biases Cytoskeletal Dynamics and Promotes Unidirectional Cell Guidance.” *Proceedings of the National Academy of Sciences of the United States of America* 112(41): 12557–62. https://pubmed.ncbi.nlm.nih.gov/26417076/ (December 18, 2022).

Svensmark, Julius H., and Cord Brakebusch. 2019a. “Rho GTPases in Cancer: Friend or Foe?” *Oncogene* 38(50): 7447–56. https://pubmed.ncbi.nlm.nih.gov/31427738/ (December 5, 2022).

———. 2019b. “Rho GTPases in Cancer: Friend or Foe?” *Oncogene* 38(50): 7447–56. https://pubmed.ncbi.nlm.nih.gov/31427738/ (December 29, 2022).

Swee, Mei H., William C. Parks, and Richard A. Pierce. 1995. “Developmental Regulation of Elastin Production. Expression of Tropoelastin Pre-MRNA Persists after down-Regulation of Steady-State MRNA Levels.” *The Journal of biological chemistry* 270(25): 14899–906. https://pubmed.ncbi.nlm.nih.gov/7797468/ (November 19, 2022).

Taufalele, Paul v. et al. 2019. “Fiber Alignment Drives Changes in Architectural and Mechanical Features in Collagen Matrices.” *PloS one* 14(5). https://pubmed.ncbi.nlm.nih.gov/31091287/ (December 21, 2022).

Thé, Manuel et al. 2006. “Anisotropy of Cell Adhesive Microenvironment Governs Cell Internal Organization and Orientation of Polarity.” *Proceedings of the National Academy of Sciences of the United States of America* 103(52): 19771–76. https://www.pnas.org/doi/abs/10.1073/pnas.0609267103 (November 27, 2022).

Tinevez, Jean Yves et al. 2012a. “A Quantitative Method for Measuring Phototoxicity of a Live Cell Imaging Microscope.” *Methods in Enzymology* 506: 291–309.

———. 2012b. “A Quantitative Method for Measuring Phototoxicity of a Live Cell Imaging Microscope.” *Methods in Enzymology* 506: 291–309.

Tojkander, Sari, Gergana Gateva, and Pekka Lappalainen. 2012. “Actin Stress Fibers--Assembly, Dynamics and Biological Roles.” *Journal of cell science* 125(Pt 8): 1855–64. https://pubmed.ncbi.nlm.nih.gov/22544950/ (November 23, 2022).

Ulrich, Peter, and Anthony Cerami. 2001. “Protein Glycation, Diabetes, and Aging.” *Recent progress in hormone research* 56: 1–21. https://pubmed.ncbi.nlm.nih.gov/11237208/ (November 30, 2022).

Wang, E., C. M. Babbey, and Kenneth W. Dunn. 2005. “Performance Comparison between the High-Speed Yokogawa Spinning Disc Confocal System and Single-Point Scanning Confocal Systems.” *Journal of Microscopy* 218(2): 148–59. https://onlinelibrary.wiley.com/doi/full/10.1111/j.1365-2818.2005.01473.x (October 18, 2022).

Wang, Xianhua et al. 2013. “Imaging ROS Signaling in Cells and Animals.” *Journal of Molecular Medicine (Berlin, Germany)* 91(8): 917. /pmc/articles/PMC3730091/ (December 29, 2022).

Warner, Harry, Beverley J. Wilson, and Patrick T. Caswell. 2019. “Control of Adhesion and Protrusion in Cell Migration by Rho GTPases.” *Current opinion in cell biology* 56: 64–70. https://pubmed.ncbi.nlm.nih.gov/30292078/ (December 5, 2022).

Wilson, Brian C., and Steven L. Jacques. 1990. “Optical Reflectance and Transmittance of Tissues: Principles and Applications.” *IEEE Journal of Quantum Electronics* 26(12): 2186–99.

Winer, Arthur, Sylvia Adams, and Paolo Mignatti. 2018. “Matrix Metalloproteinase Inhibitors in Cancer Therapy: Turning Past Failures Into Future Successes.” *Molecular cancer therapeutics* 17(6): 1147–55. https://pubmed.ncbi.nlm.nih.gov/29735645/ (December 21, 2022).

Winter, Peter W et al. 2014. “Two-Photon Instant Structured Illumination Microscopy Improves the Depth Penetration of Super-Resolution Imaging in Thick Scattering Samples.” *Optica* 1(3): 181–91. http://www.ncbi.nlm.nih.gov/pubmed/25485291 (August 23, 2022).

Wolf, Katarina et al. 2013. “Physical Limits of Cell Migration: Control by ECM Space and Nuclear Deformation and Tuning by Proteolysis and Traction Force.” *Journal of Cell Biology* 201(7): 1069–84. www.jcb.org/cgi/doi/10.1083/jcb.201210152JCB1069 (December 21, 2022).

Wozniak, Michele A. et al. 2003. “ROCK-Generated Contractility Regulates Breast Epithelial Cell Differentiation in Response to the Physical Properties of a Three-Dimensional Collagen Matrix.” *The Journal of cell biology* 163(3): 583–95. https://pubmed.ncbi.nlm.nih.gov/14610060/ (December 17, 2022).

Yan, Shi Fang, Ravichandran Ramasamy, Yoshifumi Naka, and Ann Marie Schmidt. 2003. “Glycation, Inflammation, and RAGE: A Scaffold for the Macrovascular Complications of Diabetes and Beyond.” *Circulation research* 93(12): 1159–69. https://pubmed.ncbi.nlm.nih.gov/14670831/ (November 29, 2022).

Yang, Ya Li, and Laura J. Kaufman. 2009. “Rheology and Confocal Reflectance Microscopy as Probes of Mechanical Properties and Structure during Collagen and Collagen/Hyaluronan Self-Assembly.” *Biophysical Journal* 96(4): 1566. /pmc/articles/PMC2717242/ (September 2, 2022).

Yeung, Tony et al. 2005a. “Effects of Substrate Stiffness on Cell Morphology, Cytoskeletal Structure, and Adhesion.” *Cell motility and the cytoskeleton* 60(1): 24–34. https://pubmed.ncbi.nlm.nih.gov/15573414/ (December 17, 2022).

———. 2005b. “Effects of Substrate Stiffness on Cell Morphology, Cytoskeletal Structure, and Adhesion.” *Cell Motility and the Cytoskeleton* 60(1): 24–34. https://onlinelibrary.wiley.com/doi/full/10.1002/cm.20041 (December 29, 2022).

Yolland, Lawrence et al. 2019. “Persistent and Polarized Global Actin Flow Is Essential for Directionality during Cell Migration.” *Nature Cell Biology 2019 21:11* 21(11): 1370–81. https://www.nature.com/articles/s41556-019-0411-5 (August 22, 2022).

York, Andrew G. et al. 2013. “Instant Super-Resolution Imaging in Live Cells and Embryos via Analog Image Processing.” *Nature Methods 2013 10:11* 10(11): 1122–26. https://www.nature.com/articles/nmeth.2687 (December 2, 2022).

Zaidel-Bar, R., M. Cohen, L. Addadi, and B. Geiger. 2004a. “Hierarchical Assembly of Cell-Matrix Adhesion Complexes.” *Biochemical Society transactions* 32(Pt3): 416–20. https://pubmed.ncbi.nlm.nih.gov/15157150/ (December 14, 2022).

———. 2004b. “Hierarchical Assembly of Cell-Matrix Adhesion Complexes.” *Biochemical Society transactions* 32(Pt3): 416–20. https://pubmed.ncbi.nlm.nih.gov/15157150/ (December 29, 2022).

Zhang, Jun Ming, and Jianxiong An. 2007. “Cytokines, Inflammation and Pain.” *International anesthesiology clinics* 45(2): 27. /pmc/articles/PMC2785020/ (December 4, 2022).

Zhang, Shuguang. 2003. “Fabrication of Novel Biomaterials through Molecular Self-Assembly.” *Nature Biotechnology 2003 21:10* 21(10): 1171–78. https://www.nature.com/articles/nbt874 (November 27, 2022).

Zhovmer, Alexander, and Christian A. Combs. 2021. “A Step-by-Step Guide to Instant Structured Illumination Microscopy (ISIM).” *Methods in Molecular Biology* 2304: 347–59.